Antarctic Division

Department of Science and Technology

AUSTRALIAN NATIONAL ANTARCTIC RESEARCH EXPEDITIONS

ANARE REPORTS

132

R. C. Lile

The flow law for isotropic and anisotropic ice at low strain rates

Anstralian Government Publishing Service
Canberra 1984

ISBN 0 644 00560 2

Typeset by Advocate Press Pty. Ltd., Melbourne.
Printed by Graphic Services Pty Ltd, Northfield, S.A.

Contents

Figures

The flow law for isotropic and anisotropic ice at low strain rates

R. C. Lile
Meteorology Department
University of Melbourne
Parkville, Victoria, Australia

ABSTRACT

One of the weakest links in present ice dynamics models is the lack of an adequate empirical flow law for polycrystalline ice in its natural state. Inadequacies include a paucity of creep data relevant to cold ice masses and a general neglect of the effects of preferred crystal orientation fabrics. The present study reports the results of 150 000 hours of creep tests on isotropic aggregates replicating conditions of temperature and shear stress relevant to polar ice masses, from which an extended isotropic flow law has been constructed. It is shown how anisotropic crystal orientation fabrics can be incorporated into such a flow law. The quantitative model developed for this purpose is made possible by: (a) the definition of a normalised third deviatoric stress invariant as a configuration parameter describing the geometrical distribution of shear stress; and (b) a reinterpretation of the scalar geometric factor employed in the analysis of monocrystalline creep as a tensor coefficient of correlation between the orientation fabric and the stress configuration parameter. Laboratory experiments are presented to substantiate the validity of the model.

1 Introduction

1.1 OUTLINE OF THE PROBLEM

The large ice masses of the earth hold significant clues to the climatic history of our planet. Several stable physical and chemical characteristics of precipitated hydrometeors and trapped atmospheric gases have been related to prevailing climatic conditions at the time of their deposition (Dansgaard 1964, Johnson et al. 1972, Raynaud and Lorius 1973, Berner et al. 1977, Boutron and Martin 1980, and Morgan 1982). These tagged volume elements are preserved in the earth's larger (polar) ice masses for tens or hundreds of thousands of years before returning to the surface. With an increased understanding of the earth's past climate gained through analysis of ice cores removed from deep boreholes, especially those of the Antarctic and Greenland ice caps, man's potential ability to understand past climatic change, and thereby predict future climatic change, may someday be realised.

One of the real interpretational limitations at present rests with our inability to accurately extrapolate the trajectory of a glacier volume element backward in time to its position at the surface. To overcome this limitation, increasingly accurate glacier dynamics models are necessary.

1.1.1 The equations of motion

The dynamical behaviour of an ice mass deforming under its own weight is governed primarily by its equation of motion and its rheological properties. For natural ice masses, Reynolds numbers are typically of the order of 10^{-14}; thus accelerations are far smaller than other forces and may be neglected. The equation of motion then takes the form

$$\sigma_{ij,j} = \rho g_i \tag{1.1}$$

where σ_{ij} is the stress tensor; ρg_i is the gravitational force per unit mass acting in the ith direction; a subscript following a comma indicates partial differentiation with respect to that co-ordinate direction; summation is implied on repeated subscripts.

Boundary conditions in terms of stress are generally unknown; however boundary velocities can normally be measured or inferred. We therefore require a relationship between the stress and strain rate tensors.

1.1.2 The flow law for ice

The relationship between the stress and strain rate tensors, the flow law for ice, describes its rheological properties. Glen (1958) discussed the theoretical possibilities for such a flow law, assuming isotropic polycrystalline ice for which the strain rate

tensor $\dot{\epsilon}_{ij}$ for steady state flow depends only on the stress tensor σ_{ij}. Under these assumptions he showed that the most general form of the flow law can be written

$$\dot{\epsilon}_{ij} = A\delta_{ij} + B\sigma_{ij} + C\sigma_{ik}\sigma_{kj}, \tag{1.2}$$

where $\delta_{ij} = 1$ if $i = j$, and $\delta_{ij} = 0$ if $i \neq j$; A, B and C are scalar functions of the three invariants of stress, I_1, I_2 and I_3 (Section 2.1.2). Glen (1958) further assumed incompressibility and independence of the flow law on I_1 (Rigsby 1958), showing that equation (1.2) can then be expressed in terms of the deviatoric stress tensor $\sigma'_{ij} = \sigma_{ij} - \frac{1}{3}I_1\delta_{ij}$ and its invariants I'_2 and I'_3 (Section 2.1.2):

$$\dot{\epsilon}_{ij} = -\tfrac{2}{3}I'_2\, C(I'_2, I'_3)\delta_{ij} + B(I'_2, I'_3)\sigma'_{ij} + C(I'_2, I'_3)\sigma'_{ik}\sigma'_{kj}. \tag{1.3}$$

Nye (1953) suggested the possibility that the components of strain rate are proportional to the components of the stress deviator, and that the constant of proportionality is a function of I'_2 only. Incorporating these assumptions, equation (1.3) reduces to

$$\dot{\epsilon}_{ij} = B(I'_2)\sigma'_{ij} \tag{1.4}$$

Taking into account the effects of temperature and crystallographic structure, equation (1.4) may be written in terms of the polycrystalline fluidity λ:

$$\dot{\epsilon}_{ij} = \lambda\sigma'_{ij}, \tag{1.5}$$

where

$$\lambda = \lambda(I'_2, I'_3\, f, T) \tag{1.6}$$

is a scalar function of the second and third deviatoric stress invariants, temperature T, and crystallography f (Section 2.3.1 and Section 3).

1.1.3 Closure of the problem

The strain rate tensor is related to the velocity gradients by definition:

$$\dot{\epsilon}_{ij} = u_{j,i} \tag{1.7}$$

where the u_j are the velocity components in each coordinate direction. For incompressible flow we have, in addition, the relationship

$$\dot{\epsilon}_{ii} = 0 \tag{1.8}$$

Thus, given the mass distribution and the strain rates at the boundaries, equations (1.1) and (1.5) may be solved for the strain rates. If the boundary velocities are known, equation (1.7) may then be solved with equation (1.8) for the velocities. Knowing the velocities and the surface distribution of accumulation and ablation, the new mass distribution is determined, and so forth.

It is clear that a successful dynamics model relies on an accurate specification of the flow law (equation 1.5) for ice.

1.2 EMPIRICAL APPROACH TO THE SPECIFICATION OF THE FLOW LAW

Empirical studies of the flow law for polycrystalline ice involve the measurement of various components of the strain rate tensor, i.e. dimensional changes as a function of time, of a specified volume or mass of ice for which the state of stress has been either measured or calculated. Two approaches to such studies are through field observations of natural ice masses and through laboratory observations of natural and synthetic ice specimens. Each approach offers certain advantages while suffering from inherent limitations.

1.2.1 Historical background

The first important laboratory observations on the deformation of ice were recorded by McConnell and Kidd (1886). Their experiments on lake ice showed that their specimens would yield plastically to shearing stresses in a plane parallel to the plane of the original water surface, even at temperatures substantially below pressure melting. Hagenbach-Bishoff (1889) expressed the view that crystalline plasticity was the primary cause of glacier flow, arguing that the irregular interlocked crystalline structure would inhibit intracrystalline rotations and displacements. Chamberlin (1928) made direct measurements of the strain rate across a thrust plane on several glaciers in an effort to test the theory of rigid motion via thrust planes. Utilising a mechanical strain gauge with a waxed recording disc, he identified periods of constant creep, no creep, and rapid adjustment. He interpreted his results as an argument against purely viscous behaviour in favor of idiomolecular exchange, yielding, and rotations between grains in conjunction with bulk sliding over bedrock and slip along well-defined thrust planes (veined structure). He concluded that glacier motion was, in fact, typical rock deformation behaviour (see Chamberlin 1936).

Following the discovery by Barnes (1929) and Bragg (1922) of the arrangement of water molecules in an ice crystal utilising x-ray analysis, Hawkes (1930) concluded that ice flow was caused by intragranular flow along basal planes, intergranular (amorphous) flow at grain boundaries, and flow along fracture surfaces within grains. It became clear that an extensive field program concerned with the structural characteristics and changes, including the transition of snow into glacier ice, was required.

It was with this goal that the Jungfraujoch Research Party of 1938 was organised. The results (Perutz and Seligman 1939; Perutz 1940; Hughes and Seligman 1939) represent a great milestone in our understanding of structural glaciology: clarification of the origin of stratification bands and their relationship to glacier motion; ellucidation of the time sequence of crystallographic features in terms of the mechanisms of grain-growth, deformation, and reorientation; and the association of crystallographic-preferred orientations with the orientation of greatest shearing stress.

Assuming a decrease of ice viscosity with depth, Streif-Becker (1938) postulated the existence of a layer of fast moving ice in the interior of glaciers, while Demorest (1941, 1943) postulated a similar 'extrusion flow' theory for ice sheets. The extrusion flow theories, (indeed all theories of glacier flow) are based essentially on a par-

ticular assumption about the rheological properties of polycrystalline ice. However, it wasn't until the middle of the twentieth century that the first carefully controlled laboratory experiments aimed at establishing the flow law for ice were undertaken. Glen (1952, 1953, 1955) tested polycrystalline blocks of ice under compressive stresses in the range from one to ten bars at temperatures from $-13\,^{\circ}C$ to the melting point. His results were similar to results found for the plastic creep of polycrystalline metals near their melting point, and provided a good fit to a power law type of flow law.

Nye (1952) then examined the flow of a valley glacier using the results of plasticity theory. Nye, approximating Glen's flow law, assumed ice to be a plastic substance having a well defined yield stress.

Glen's experiments were undertaken in conjunction with a field program (Gerrard et al. 1952) designed to measure the interior velocity distribution of a glacier, as velocity distribution predictions by the various glacier theories had not been previously verified by experiment. The results of this field study are in general agreement with the power law found by Glen, and together indicate that the power law exponent is an increasing function of increased stress. A transition region is indicated at stresses near 0.05 MN m^{-2} (0.5 bar).

With the present availability of numerical computers, glacier models are no longer restricted by the necessity of yielding analytical solutions; an empirical flow law can now be incorporated into a numerical model with relative ease. A brief summary of the empirical evidence at hand to date is given in Figure 1. Excellent reviews of recent results have been provided by Weertman (1973) and Hooke et al. (1980).

1.2.2 Field observations

Field observation programs relating to the flow law of ice have been carried out on glaciers, ice sheets, ice shelves and isolated ice caps through measurements of horizontal and vertical velocity gradients on exposed surfaces, interior vertical gradients of horizontal velocity and closure rates of boreholes and tunnels.

The techniques of surface observations of strain and associated data analysis utilising strain grids have been discussed by Nye (1959), McLaren (1968) and Holdsworth (1975) among others. The deep borehole measurement of the vertical components of strain rate, the horizontal shear rate and the relationship of the vertical to horizontal components of strain rates were discussed by Bader (1964). Nye (1953) treated the contraction rates of cylindrical holes in ice masses theoretically; his results are applicable to borehole and tunnel closure rates. Butkovich and Landauer (1959) presented a technique for the measurement of ice tunnel deformation rates.

The inherent advantage of measurements on natural ice masses is the potential ability of field results to reflect steady state conditions in the ranges of independent parameters operating in natural ice masses. The accuracy of observed strain rates is potentially excellent as a result of the large dimensions employed. On the other hand, measurements made in the interior of natural ice masses seldom offer sufficient data for the specification of the complete strain rate tensor. Together with the difficulties associated with the measurement or calculation of the stress field, the analysis of field data in terms of the flow law must often proceed under severe interpretational handicaps. These difficulties become most pronounced when the dimensions of the observed volume or area is small in comparison to the dimensions

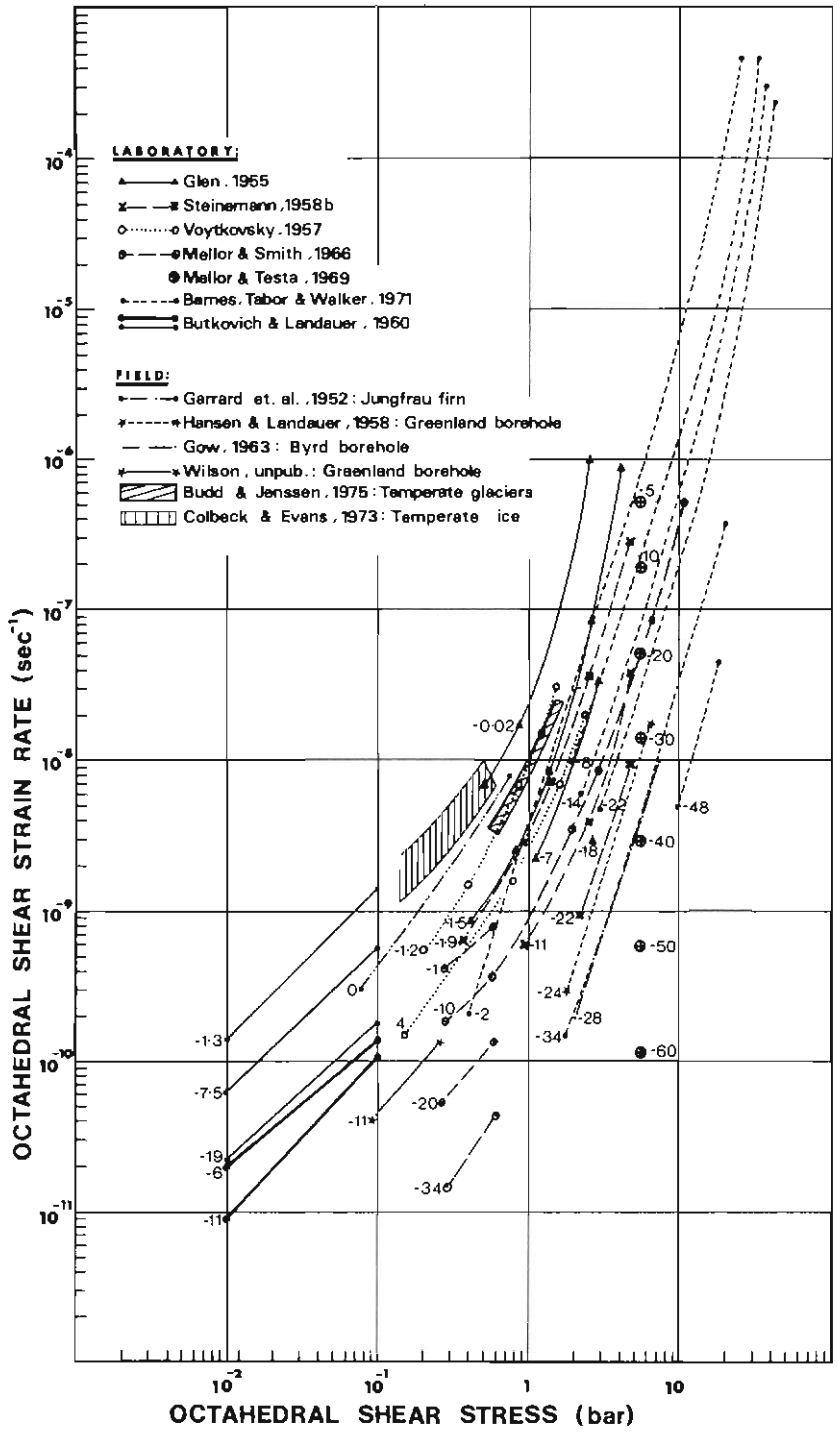

Figure 1. Flow law of ice. Laboratory and field measurements of ice strain rates versus stress. Temperatures are indicated in °C (Updated after Budd 1969).

of the region disturbed by excavation, e.g. observations of borehole and tunnel closure rates (Paterson 1977).

Interpretational difficulties may be greatly relieved with the judicious selection of observational sites. Meier (1958) argued that the common tendency to analyse field results in terms of a priori assumptions concerning the form of the flow law contributes little to progress in this field and, indeed, may lead to ambiguous conclusions. He suggested that vertical profile sites, in particular, be chosen with full consideration given to determination of the associated surface horizontal strain field.

1.2.3 Laboratory studies

In the laboratory, a high degree of control can be realised in the specification of the independent parameters of the flow law. Though specimen dimensions are necessarily limited, sensitive deformation transducers can be operated under near optimal conditions in the laboratory, thereby making possible the complete determination of the strains to a high precision.

However, the inherent steady state deformational response of natural ice to the stress field, and the apparent (Budd 1972) compatibility of ice characteristics such as texture, grain size, and preferred crystallographic orientation with the stress and deformation fields, are lost. Strain rate, texture, grain size and crystallographic anisotropy are generally observed as time dependent features of laboratory creep tests.

1.2.4 The creep test

The precise measurement of creep rates in the laboratory can be undertaken with the accurate specification of the independent creep variables. A laboratory creep test may be carried out at an accurately controlled temperature and known load on ice of specified dimensions, crystallographic characteristics, density and grain size and shape through petrographic examination and selection of natural or synthetic ice specimens. Calibrated loads are applied by means of rigid plattens, the displacement of which can be measured accurately with sensitive transducers. Specimen temperatures may be monitored continuously and controlled to the required accuracy.

The purpose of the creep test depends on the parameters being studied. Because the parameters associated with ice type are, in general, time dependent the creep test is useful in studies of the development of crystallographic orientation fabrics, syntectonic modification of grain size and shape, para- and post-kinematic recrystallisation, grain boundary migration under stress, dilatation, densification, etc. Constant strain rate tests on monocrystalline and polycrystalline specimens have proven useful in studies of microcreep mechanics. The concern here is with the use of the constant load creep test to provide 'steady state' creep results applicable to the specification of the flow law for polycrystalline ice.

The complete specification of the deformation, strain and strain rate tensors, and their octahedral values for pure shear deformation (i.e. deformation of incompressible materials) requires the measurement of two independent displacement vectors in addition to a knowledge of the relevant initial dimensions of the specimen. However, under certain conditions of symmetry, observation of a single displacement vector may be sufficient (Section 2.2.3). In order to avoid confusion, let the displacement

function be defined as the measured platten displacement with respect to time, the (octahedral) creep function as the (octahedral) strain as a function of time, and the (octahedral) creep rate function as the (octahedral) strain rate against time. Polycrystalline materials including metals, minerals and ice exhibit similar creep functions, the general form of which is illustrated in Figure 2. Three distinct periods, or stages, can be identified and are discussed below.

The instantaneous strain response of a specimen upon application of the load is elastic and recoverable (AB of Figure 2). During the earliest time dependent stage, commonly referred to as the primary stage of creep (BC of Figure 2), the rate of strain decreases with time. The primary stage is transient and is often recoverable if the total strain is insufficient to induce changes in the structure of the material. This period of deceleration has been interpreted (Gilman 1969, and Finnie and Heller 1959) as a period of work hardening during which the mobility of dislocations is decreasing due to mutual interference as dislocations move in response to the applied stress. If linearly time dependent plastic strain is removed from the curve ABCF, its similarity to the relaxation curve FGH (Figure 2) is well known. The residual strain, HI, is a result of this irrecoverable plastic strain component.

When the rate of work hardening has decreased so as to balance the rate of thermal softening, the creep function exhibits a period of unaccelerated or quasi-viscous creep known as the secondary stage of creep (straight line CD of Figure 2). This is a stage of irrecoverable, purely plastic strain. An extended period of secondary creep (CD of Figure 2) may in some cases reflect an equilibrium state characteristic of the structural parameters measured prior to deformation, i.e. before the onset of dynamic

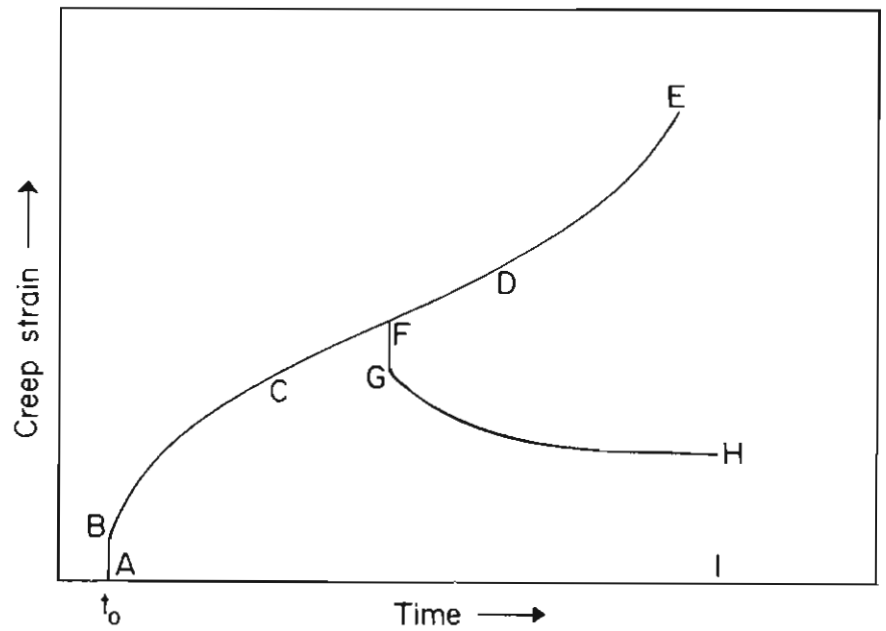

Figure 2. Typical creep curve for a polycrystalline aggregate.

recrystallisation. Whenever possible, a post-deformation structural analysis should be made to confirm the invariance of these parameters during the test.

The third, or tertiary, stage of creep is characterised by a period of accelerating strain rate (DE of Figure 2). For stresses sufficiently high to cause failure, this acceleration has been attributed to the onset of intercrystalline cracking (Rotherham 1951). However, at reduced stress levels, the increase in strain rate is apparently caused by flow-induced structural changes of the material, e.g. polygonisation, dynamic recrystallisation and grain boundary migration leading to the development of preferred crystallographic orientations (Kamb 1972, Vialov 1970, Steinemann 1958b, Shumskiy 1964, and Finnie and Heller 1959). Duval (1972) and Budd and Matsuda (1974) noted a cyclic variation in the tertiary creep rate of ice in the laboratory. Gifkins (1959) and Richardson et al. (1966) have observed a similar phenomenon in the creep behaviour of lead and nickel respectively. Gifkins attributed the tertiary periods of increased strain rate to the primary creep of large new grains formed by dynamic recrystallisation. Luton and Sellars (1969) noted a critical shearing stress separating states of periodic and continuous recrystallisation.

Kamb (1972) suggested that fabric development proceeds in a stepwise fashion, noting distinct reorganisation of crystal structure at total shear strains of 0.04, 0.1 and 0.3. An alternative possibility presented by Kamb (1972) is that fabric development proceeds continuously, but that at a given total strain large statistical fluctuations influence the extent of reorientation in localised regions of the specimen. However, in light of the inhomogenous states of stress and strain in laboratory specimens (Section 2), local regions of a specimen reach a given total strain at varying total bulk strains. The observed effect might then be similar to that observed by Kamb (1972).

Evidently, then, the structural changes characteristic of the tertiary stage of creep, once initiated, may proceed rapidly, leading to catastrophic failure; through a series of transition periods, each followed by a certain degree of recovery, thereby resulting in a periodic tertiary creep function; or continuously, exhibiting a smooth transition to an equilibrium tertiary state.

An important point to be raised here is that the secondary creep rate, while apparently characteristic of an equilibrium state, may, in fact, be that of a quasi-stable state preceeding the accumulation of sufficient strain for the onset of recrystallisation and subsequent establishment of a crystallographic structure compatible (Budd 1972) with the local stress situation and flow picture. The argument, then, is that prolonged steady secondary creep often leads to recrystallisation and, therefore, to modifications of the independent structural parameters of the flow law as exemplified by a modified rate of strain (tertiary creep phase). The stresses operating in natural ice masses are maintained for extremely long periods of time. Furthermore, there is considerable evidence (Budd 1972) that crystallographic and other structural properties of natural ice are flow induced, resulting from dynamic recrystallisation and other dynamic mechanisms. It seems reasonable, therefore, to associate a final stage of tertiary creep with a flow law for natural ice masses.

For an important range of naturally occurring temperature and stress, tertiary creep has not been attained, even after prolonged laboratory creep tests. Indeed, at low temperatures and stresses, the existence of a tertiary creep state has not been established by laboratory tests. When the tertiary stage is achieved, and settles to a subsequent period of constant rate of strain persisting sufficiently long to establish beyond reasonable doubt that all dynamic mechanisms are in equilibrium, the final

strain rate may then be regarded as characteristic of the final structure of the specimen under the test conditions of temperature and stress.

Following the above arguments, degeneration of the secondary stage to a point of inflection between the primary and tertiary stages suggests that there is no justification in associating the minimum strain rate at the inflection point with the steady or secondary rate; i.e. the independent variables related to ice structure remain time dependent.

1.2.5 Need for further investigation

From Figure 1 it is evident that two independent variables, octahedral shearing stress and temperature, account for the major proportion of the variance in observed deformation rates. Budd (1969) pointed out that the experimental data still left the strain rates in doubt by a factor of two, and probably more, due apparently to effects associated with ice structure, e.g. grain texture and crystallographic orientation fabrics. This doubt persists even now. In addition, much of the data is based on isometric, isotropic specimens, whereas the crystals of natural ice masses tend to adopt systematic orientation fabrics and textures (Rigsby 1960, and Budd 1972).

Laboratory studies yielding strain rates less than 10^{-10}sec^{-1} present special problems related to the measurement of extremely small deformations over long periods and, not unexpectedly, in the interpretation of these results. Indeed, Steinemann (1958b) cautioned laboratory researchers as to the pitfalls accompanying the measurement and interpretation of deformation rates less than 10^{-9}sec^{-1}. The relative paucity of laboratory data at deformation rates less than about 10^{-10}sec^{-1}, shown by Figure 1, attests to the inherent difficulties. It is only through the relatively recent introduction of stable, sensitive and accurate electronic displacement transducers that studies in this important region are practical. Even so, time scales of the order of months or years are required.

In light of the fact that the range of octahedral stress and temperature relevant to the flow of natural ice masses spans values from approximately 0.01 to 3 bars and 0 °C to − 60 °C it is clear that an urgent need for additional data extending into this region exists. Two areas of investigation are suggested: the extension of the flow law for isometric isotropic ice down to octahedral values near 10^{-12}sec^{-1}; and the methodical investigation of the flow law for natural anisotropic structures in terms of, for instance, an enhancement factor relative to the isotropic flow law.

1.3 PURPOSE AND SCOPE OF THE PRESENT STUDY

In the introduction it is shown that neither field nor laboratory studies can stand alone in providing an adequate specification of the flow law for ice. Indeed, both field and laboratory studies must proceed hand-in-hand with a program of numerical modelling to achieve useful results. The study described herein is but one aspect of a continuing joint project undertaken through the co-operation of the Meteorology Department of the University of Melbourne and the Antarctic Division of the Commonwealth Department of Science and Technology. The purposes of this study are as follows:

- To extend the suite of isotropic creep data into the ranges of temperature and shear stress commonly observed in natural ice masses. This aspect of the study is a continuing effort with its long-term goal being coverage of the temperature range between 0 °C and −50 °C for shear stresses between 0.05 and 2.8 bars octahedral. The immediate concern here is with polar ice masses. Data are presented for temperatures ranging from −10 °C to −50 °C at shear stresses between 0.05 and 2.8 bars octahedral. Creep studies near pressure melting require special treatment and are beyond the scope of the present study.
- To extend the applicability of the isotropic results to natural ice masses through a model of strain rate enhancement due to anisotropy effects; and to test it.

2. The rheological variables

While the flow law for polycrystalline ice is influenced by many variables, the most important of these are evidently the stress tensor, temperature and the structure of the ice itself. The emphasis of the present study is the interrelationship between the stress situation and crystallographic structure, and the combined influence on the rate of strain. Consequently, the stress tensor, strain rate tensor and crystallography are examined in some detail. The remaining variables are considered primarily to establish an appreciation for the necessary controls and limitations imposed on experiments designed to isolate the effects of the aforementioned control variables.

2.1 STRESS

2.1.1 The stress tensor

The stress tensor σ_{ij} is written in the usual manner as

$$\sigma_{ij} = \begin{vmatrix} \sigma_{xx} & \tau_{xy} & \tau_{xz} \\ \tau_{yx} & \sigma_{yy} & \tau_{yz} \\ \tau_{zx} & \tau_{zy} & \sigma_{zz} \end{vmatrix} \tag{2.1}$$

From a consideration of the equilibrium of a volume element, the couples given by $\tau_{ij} - \tau_{ji}$ must vanish; therefore $\tau_{ij} = \tau_{ji}$ so that σ_{ij} is symmetric. It can be shown generally (Jaeger 1969) that by a suitable choice of co-ordinate axes a symmetric tensor, say τ_{ij}, can be represented in the form

$$\tau_{ij} = \begin{vmatrix} \tau_1 & 0 & 0 \\ 0 & \tau_2 & 0 \\ 0 & 0 & \tau_3 \end{vmatrix} \tag{2.2}$$

where, by convention, $\tau_1 \geq \tau_2 \geq \tau_3$ are the principal tensor components parallel to the principal axes. In particular, then,

$$\sigma_{ij} = \begin{vmatrix} \sigma_1 & 0 & 0 \\ 0 & \sigma_2 & 0 \\ 0 & 0 & \sigma_3 \end{vmatrix} \tag{2.3}$$

where $\sigma_1 \geq \sigma_2 \geq \sigma_3$.

Subtracting the hydrostatic pressure from the stress tensor yields the deviatoric stress tensor

$$\sigma'_{ij} = \sigma_{ij} - p\delta_{ij} \tag{2.4a}$$

where

$$p = \tfrac{1}{3}\sigma_{kl}\,\delta_{kl} \tag{2.4b}$$

The principal stress deviators are parallel, respectively, to the principal stress axes. Thus, in the principal stress co-ordinates

$$\sigma'_{ij} = \begin{vmatrix} \sigma'_1 & 0 & 0 \\ 0 & \sigma'_2 & 0 \\ 0 & 0 & \sigma'_3 \end{vmatrix} \tag{2.5a}$$

where the principal stress deviators are related by the expression

$$\sigma'_1 + \sigma'_2 + \sigma'_3 \equiv 0 \tag{2.5b}$$

Denoting the magnitude of the resolved shear stress on a given plane by τ, Jaeger (1969) shows that there are three stationary values, τ_i, associated with the planes whose normals bisect the angles between the principal axes. The magnitudes of these principal shear stresses are

$$\left.\begin{aligned} \tau_1 &= \tfrac{1}{2}(\sigma_2 - \sigma_3) = \tfrac{1}{2}(\sigma'_2 - \sigma'_3) \\ \tau_2 &= \tfrac{1}{2}(\sigma_1 - \sigma_3) = \tfrac{1}{2}(\sigma'_1 - \sigma'_3) \\ \tau_3 &= \tfrac{1}{2}(\sigma_1 - \sigma_2) = \tfrac{1}{2}(\sigma'_1 - \sigma'_2) \end{aligned}\right\} \tag{2.6}$$

Just as the principal stress deviators are related by equation (2.5b), we have a similar relationship among the principal shear stresses

$$\tau_1 - \tau_2 + \tau_3 \equiv 0 \tag{2.7}$$

Manipulation of equation (2.6) together with equation (2.5b) yields

$$\left.\begin{aligned} \sigma'_1 &= \tfrac{2}{3}(\tau_2 - \tau_3) \\ \sigma'_2 &= \tfrac{2}{3}(\tau_1 - \tau_3) \\ \sigma'_3 &= -\tfrac{2}{3}(\tau_1 + \tau_2) \end{aligned}\right\} \tag{2.8}$$

2.1.2 Invariants

Hydrostatic pressure

The first invariant of the stress tensor (Jaeger 1969) may be written

$$I_1 = \sigma_{ij}\delta_{ij} = 3p \tag{2.9}$$

Thus I_1 is physically related to the hydrostatic pressure. It follows from equation (2.5b) that the first invariant of the deviatoric stress tensor vanishes:

$$I'_1 = \sigma'_{ij}\delta_{ij} \equiv 0 \tag{2.10}$$

The physical effect of hydrostatic pressure on the deformation rate of an incompressible material evidently vanishes in principle. Empirical confirmation of this is provided by Rigsby (1958).

Octahedral and effective shear stress

The second invariant of the deviatoric stress tensor is (Jaeger 1969)

$$I_2' \equiv \tfrac{1}{2}\sigma_{ij}'\sigma_{ij}' \tag{2.11a}$$

$$= \tfrac{1}{6}[(\sigma_2 - \sigma_3)^2 + (\sigma_3 - \sigma_1)^2 + (\sigma_1 - \sigma_2)^2]$$

Since the second deviatoric invariant can be represented in terms of the differences of the principal stresses, we have by equations (2.10) and (2.6)

$$I_2' = \tfrac{2}{3}(\tau_1^2 + \tau_2^2 + \tau_3^2) \tag{2.11b}$$

The shear stress across the octahedral plane, whose normal has direction cosines $(3)^{-\frac{1}{2}}$ referred to the principal axes, has been shown (Jaeger 1969) to be

$$\tau_o \equiv (\sigma_{ij}'\sigma_{ij}'/3)^{\frac{1}{2}}$$

$$= (2I_2'/3)^{\frac{1}{2}} \tag{2.12}$$

$$= \tfrac{2}{3}(\tau_1^2 + \tau_2^2 + \tau_3^2)^{\frac{1}{2}}$$

Hereafter a zero subscript denotes the octahedral value of the associated tensor defined as in equation (2.12).

The effective shear stress defined by Nye (1957) is related to the octahedral shear stress and second deviatoric stress invariant as

$$\tau_e = (I_2')^{\frac{1}{2}} = (2/3)^{\frac{1}{2}}\tau_o \tag{2.13}$$

Stress configuration

The third invariant of the stress deviator is defined (Jaeger 1969, and Glen 1958) as

$$I_3' \equiv \tfrac{1}{3}\,\sigma_{ij}'\sigma_{jk}'\sigma_{ki}' \tag{2.14}$$

$$= \sigma_1'\sigma_2'\sigma_3'$$

This invariant contains information related to stress configuration. When dependence on I_2' is eliminated from I_3' by scaling the components of σ_{ij}' to an octahedral value of $2^{1/2}$, the resulting normalised value (λ_I) of I_3' ranges from $+1$ for uniaxial tension ($\sigma_2' = \sigma_3' = -\tfrac{1}{2}\sigma_1'$) through zero for a two-dimensional stress situation ($\sigma_2' = 0$, so that $\sigma_3' = -\sigma_1'$) to -1 for uniaxial compression ($\sigma_1' = \sigma_2' = -\tfrac{1}{2}\sigma_3'$).

Kamb (1972) proposed two alternative configuration parameters. The first and most general is defined in terms of the principal stress differences as [$\lambda_K =]\ (\sigma_2 - \sigma_1)/(\sigma_3 - \sigma_1)$. Many of the tests described by Kamb (1972) were performed on an annulus of ice in combined torsion and compression. As the tangential force in such tests varies inversely as the radius, it is clear that the stress situation is distributed inhomogeneously through the annulus and is strongly dependent on the ratio of the difference and sum of the outer and inner radii. Evidently to overcome the difficulties associated with determining the effective value of λ_K, Kamb (1972) defined a second parameter [$\lambda_S =]\sigma/\tau$ directly in terms of the applied compressive σ and mean shear τ loads. Budd (1972), considering the relationship between the symmetry of the stress situation, flow picture and orientation fabric, used the configuration parameter [$\lambda_B =]\sigma_2'/\sigma_1'$.

The parameter λ_I offers two main advantages over those suggested by Kamb (1972) and Budd (1972): its symmetry with respect to the sign of the dominant normal stress, i.e. whether tensile or compressive, and its unity limits. However, the extended computations necessary to evaluate λ_I would seem to offset these advantages in practice. Therefore, an alternative definition of the third deviatoric stress invariant

in terms of the principal shear stresses is proposed here. The invariant

$$\Lambda = (\tau_3 - \tau_1)/\tau_2 \tag{2.15}$$

is non-dimensional and independent of I_2' while retaining the symmetry and unity limits exhibited by the normalised form of I_3'. The relationships between the various stress configuration parameters discussed above are now considered.

Expanding Λ in terms of the principal stresses using equations (2.15) and (2.6) we obtain

$$\begin{aligned}\Lambda &= \frac{\sigma_1 - 2\sigma_2 + \sigma_3}{\sigma_1 - \sigma_3} \\ &= \frac{2\sigma_2 - \sigma_1 - \sigma_3}{\sigma_3 - \sigma_1} + \frac{\sigma_3 - \sigma_1}{\sigma_3 - \sigma_1} - 1 \\ &= 2\left[\frac{\sigma_2 - \sigma_1}{\sigma_3 - \sigma_1}\right] - 1\end{aligned} \tag{2.16}$$

thus

$$\Lambda = 2\lambda_K - 1 \tag{2.17}$$

Continuing with equation (2.16) and introducing equation (2.6) then equation (2.5b) gives

$$\begin{aligned}\Lambda &= 2\left[\frac{\sigma_2 - \sigma_1}{\sigma_3 - \sigma_1}\right] - 1 \\ &= 2\left[\frac{\sigma_2' - \sigma_1'}{\sigma_3' - \sigma_1'}\right] - 1 \\ &= -2\left[\frac{\sigma_2' - \sigma_1'}{2\sigma_1' + \sigma_2'}\right] - \left[\frac{2\sigma_1' + \sigma_2'}{2\sigma_1' + \sigma_2'}\right] \\ &= \frac{-3\sigma_2'}{2\sigma_1' + \sigma_2'}\end{aligned} \tag{2.18}$$

Finally, dividing both the numerator and denominator of equation (2.18) by σ_1' yields

$$\Lambda = \frac{-3\lambda_B}{\lambda_B + 2} \tag{2.19}$$

The stress situation in a combined torsion/compression experiment approaches homogeneity as the ratio of the distance between the outer and inner radii to the mean radius diminishes. The stress situation then approaches the case of a sample between parallel plattens to which a normal stress σ and a shear stress τ are applied in combination. It is shown from equation (2.41) that the associated stress configuration parameter is

$$\Lambda = \sigma (\sigma^2 + 4\tau^2)^{-1/2}$$

$$= \frac{\sigma}{\tau}\left(\frac{\sigma^2}{\tau^2} + 4\right)^{-1/2}$$

$$= \lambda_S (\lambda_S^2 + 4)^{-1/2} \tag{2.20}$$

The relationship between these various configuration parameters is illustrated in Figure 3. As no definite relationship has yet been found between the stress configuration (i.e. third deviatoric stress invariant) and the octahedral strain rate of an isotropic aggregate (see, however, Glen 1958), a stress configuration parameter will be most useful when considering the effects of anisotropy on the strain rate (Section 3).

2.1.3 State of stress

An arbitrary deviatoric state of stress may be specified in terms of the octahedral shear stress τ_o, the stress configuration parameter Λ and the orientation of the principal axes of stress. To demonstrate that this is so, expressions for the principal stresses and the principal shear stresses are next developed in terms of τ_o and Λ.

Beginning with equation (2.15) and eliminating first τ_1 then τ_2 using equation (2.7), we may write

$$\Lambda = \frac{\tau_3 - \tau_2 + \tau_3}{\tau_2}$$

$$= \frac{2\tau_3}{\tau_2} - 1 \tag{2.21}$$

or

$$\tau_3 = \frac{(1 + \Lambda)}{2}\tau_2 \tag{2.22}$$

and then similarly

$$\tau_1 = \frac{(1 - \Lambda)}{2}\tau_2 \tag{2.23}$$

By equation (2.12)

$$\tau_o = \tfrac{2}{3}\,\tau_2\left[\frac{(1 - \Lambda)^2}{2} + 1 + \frac{(1 + \Lambda)^2}{2}\right]^{1/2} \tag{2.24}$$

so that

$$\tau_2 = \frac{3}{\sqrt{2}}\frac{\tau_o}{(3 + \Lambda^2)^{1/2}}. \tag{2.25}$$

It follows that

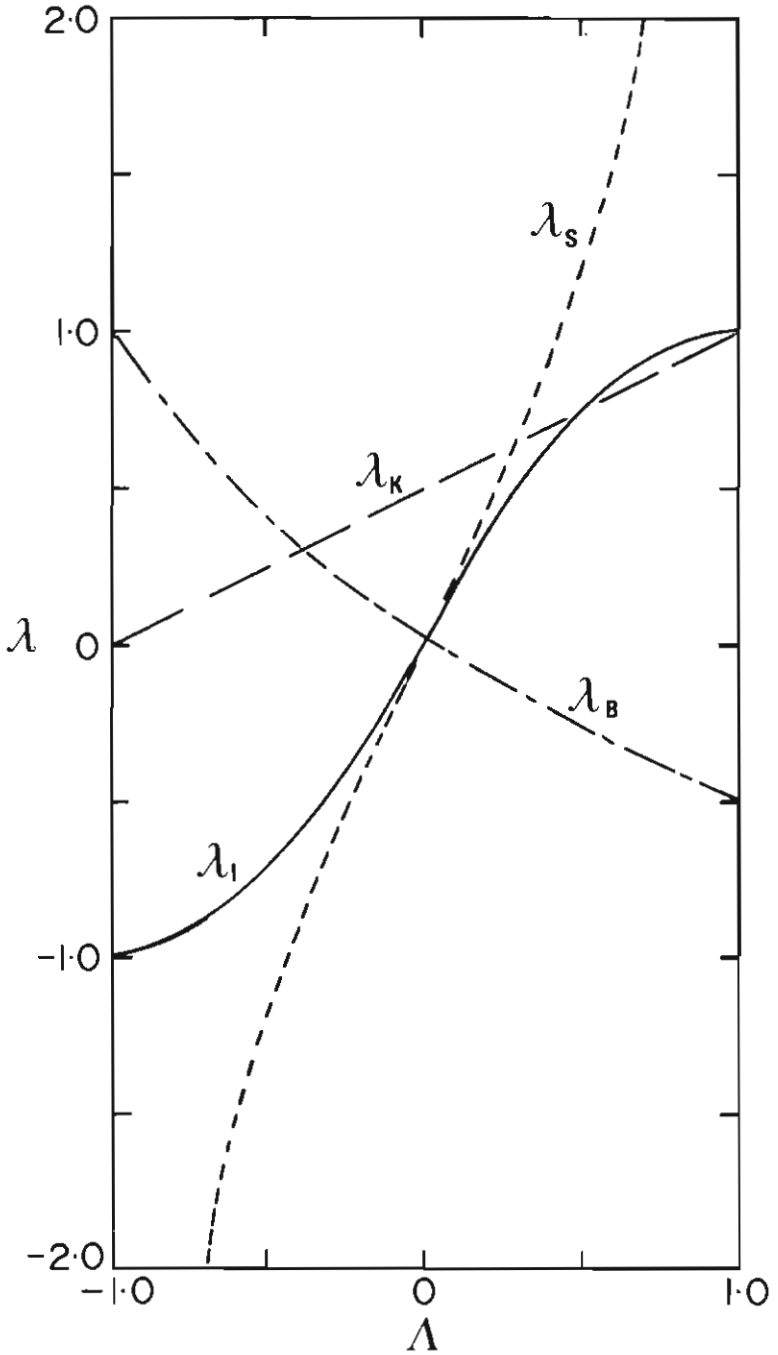

Figure 3. Relationship between the various stress configuration parameters.

$$\left.\begin{aligned}
\tau_1 &= \frac{3}{\sqrt{2}}\left(\frac{1 - \Lambda}{2}\right)\frac{\tau_o}{(3 + \Lambda^2)^{1/2}} \\
\tau_2 &= \frac{3}{\sqrt{2}}\,\frac{\tau_o}{(3 + \Lambda^2)^{1/2}} \\
\tau_3 &= \frac{3}{\sqrt{2}}\left(\frac{1 + \Lambda}{2}\right)\frac{\tau_o}{(3 + \Lambda^2)^{1/2}}
\end{aligned}\right\} \qquad (2.26)$$

Therefore, by equation (2.8)

$$\left.\begin{aligned}
\sigma_1' &= \frac{\Lambda + 3}{\sqrt{2}\,(3 + \Lambda^2)^{1/2}}\,\tau_o \\
\sigma_2' &= \frac{-2\Lambda}{\sqrt{2}\,(3 + \Lambda^2)^{1/2}}\,\tau_o \\
\sigma_3' &= \frac{\Lambda - 3}{\sqrt{2}\,(3 + \Lambda^2)^{1/2}}\,\tau_o
\end{aligned}\right\} \qquad (2.27)$$

Also

$$\begin{aligned}
I_3' &= \sigma_1'\,\sigma_2'\,\sigma_3' \\
&= \frac{(3 + \Lambda)\,(3 - \Lambda)\,\Lambda}{\sqrt{2}\,(3 + \Lambda^2)^{3/2}}\tau_o^3
\end{aligned} \qquad (2.28)$$

Finally

$$\lambda_1 = \frac{(3 + \Lambda)\,(3 - \Lambda)\,\Lambda}{(3 + \Lambda^2)^{3/2}} \qquad (2.29)$$

Even in the simplest cases, the task of determining the distributed state of stress in an isotropic laboratory specimen stressed under externally applied forces is complicated by end effects. Generally a homogeneous distribution of τ_o and Λ is required. The extent to which end effects permeate a laboratory specimen and thereby modify an otherwise homogeneous distribution of these parameters depends primarily on the geometry of the specimen and the nature of the specimen-platten interface.

As the ratio of specimen volume to the surface area under load is increased, the distribution of stress becomes increasingly homogeneous. This has been confirmed experimentally using the stress analysis techniques of photo-elasticity theory. St Venant, in 1885, was apparently the first to appreciate this phenomenon. The principle bearing his name states, in essence, that if the external forces applied to the surface of an elastic body are replaced by a different but statistically equivalent set of forces, then gross modifications to the initial stress field will occur near the region of the applied forces, but that the stress distribution at points sufficiently removed from the applied forces will remain essentially unaltered (page 22).

2.1.4 Common types of stress configuration

Assuming that end effects are negligible, the state of stress in a laboratory specimen is now examined for the most common constant load configurations.

The uniaxial configuration

Consider a specimen mounted between parallel plattens to which a constant normal load σ is applied. If the load is tensile ($\sigma > 0$), the principal stresses are (σ, 0, 0); the principal deviatoric stresses are ($2\sigma/3$, $-\sigma/3$, $-\sigma/3$); and by equations (2.6) the principal shear stresses are (0, $\sigma/2$, $\sigma/2$). Thus

$$\tau_o = \tfrac{2}{3}(\tau_1^2 + \tau_2^2 + \tau_3^2)^{1/2}$$

$$= \frac{\sqrt{2}}{3}\sigma \tag{2.30}$$

and

$$\Lambda = (\tau_3 - \tau_1)/\tau_2$$

$$= 1 \tag{2.31}$$

For a compressive load ($\sigma < 0$) the principal stresses become (0, 0, σ); the principal deviatoric stresses, ($-\sigma/3$, $-\sigma/3$, $2\sigma/3$); and the principal shear stresses, ($-\sigma/2$, $-\sigma/2$, 0). Therefore

$$\tau_o = \frac{\sqrt{2}}{3}\,|\,\sigma\,| \tag{2.32}$$

and

$$\Lambda = -1 \tag{2.33}$$

For the tensile case the first principal axis of stress is normal to the plattens, while in the compressive case the third principal axis of stress is normal to the plattens. The remaining axes may be chosen arbitrarily due to the symmetry of the stress situation.

The two-dimensional configuration

Consider a specimen loaded in a uniaxial configuration as discussed above, but with movement confined to two dimensions by a pair of parallel fixed lateral plattens. With the application of a compressive load ($\sigma < 0$), a reactive compressive load is induced normal to the fixed plattens of magnitude $\sigma/2$. The principal stresses are (0, $\sigma/2$, σ), and the principal deviatoric stresses are ($-\sigma/2$, 0, $\sigma/2$). The second and third principal axes of stress are normal to the fixed and loaded plattens, respectively. The principal shear stresses are ($-\sigma/4$, $-\sigma/2$, $-\sigma/4$) which give

$$\tau_o = \frac{\sqrt{2}\;|\,\sigma\,|}{\sqrt{3}\;2} \tag{2.34}$$

and

$$\Lambda = 0. \tag{2.35}$$

The composite configuration

When combined normal σ and shear τ loads are applied to parallel plattens, a composite stress configuration is obtained. If a set of co-ordinates is chosen so that x_3 is normal to the plattens and x_1 is tangential to the plattens and directed parallel to the applied shear load, the stress tensor is

$$\sigma_{ij} = \begin{vmatrix} 0 & 0 & \tau \\ 0 & 0 & 0 \\ \tau & 0 & \sigma \end{vmatrix} \tag{2.36}$$

Solution of the characteristic equation associated with σ_{ij} (Jaeger 1969) yields the principal stresses

$$\left.\begin{aligned} \sigma_1 &= \tfrac{1}{2}\sigma + \tfrac{1}{2}(\sigma^2 + 4\tau^2)^{\frac{1}{2}} \\ \sigma_2 &= 0 \\ \sigma_3 &= \tfrac{1}{2}\sigma - \tfrac{1}{2}(\sigma^2 + 4\tau^2)^{\frac{1}{2}} \end{aligned}\right\} \tag{2.37}$$

The principal deviatoric stresses are thus

$$\left.\begin{aligned} \sigma_1' &= \tfrac{1}{6}\sigma + \tfrac{1}{2}(\sigma^2 + 4\tau^2)^{\frac{1}{2}} \\ \sigma_2' &= -\tfrac{1}{3}\sigma \\ \sigma_3' &= \tfrac{1}{6}\sigma - \tfrac{1}{2}(\sigma^2 + 4\tau^2)^{\frac{1}{2}} \end{aligned}\right\} \tag{2.38}$$

Substitution of equations (2.38) into equations (2.6) gives the principal shear stresses

$$\left.\begin{aligned} \tau_1 &= \tfrac{1}{4}(\sigma^2 + 4\tau^2)^{\frac{1}{2}} - \tfrac{1}{4}\sigma \\ \tau_2 &= \tfrac{1}{2}(\sigma^2 + 4\tau^2)^{\frac{1}{2}} \\ \tau_3 &= \tfrac{1}{4}(\sigma^2 + 4\tau^2)^{\frac{1}{2}} + \tfrac{1}{4}\sigma \end{aligned}\right\} \tag{2.39}$$

therefore

$$\tau_o = \frac{\sqrt{2}}{3}(\sigma^2 + 4\tau^2)^{\frac{1}{2}} \tag{2.40}$$

and

$$\Lambda = \sigma(\sigma^2 + 4\tau^2)^{-\frac{1}{2}} \tag{2.41}$$

The second principal axis of stress is oriented normal to the plane containing σ and τ. The first principal axis is tilted at an angle

$$\theta = \tfrac{1}{2}\tan^{-1}\left[\frac{2\tau}{\sigma}\right] \tag{2.42}$$

toward the x_1 axis, i.e. into the direction of shear for $\sigma > 0$ and away from the direction of shear for $\sigma < 0$.

The specimen-platten interface

Nearly perfect contact can be achieved between an ice specimen and a metal platten by freezing the warmed platten onto the specimen. A platten bonded in this manner

is capable of transmitting a highly uniform normal force to the specimen. If the boundary stress required at the interface is to be purely compressive (negligible traction or shearing forces), such a 'frozen bond' may prove to be unsuitable.

In order to achieve complete radial freedom in uniaxial tests, three approaches are possible (Hawkes and Mellor 1970). The first is to match the radial strain of the platten to the radial strain of the specimen; the second is to reduce the coefficient of friction between the specimen and the platten to a value less than that which prevents slip; and the third is by hydrostatically loading the ends of the specimen.

The best guarantee of strain compatibility between the platten and sample is through the use of a polycrystalline ice platten. Dumb-bell-shaped specimens achieve this effect, but this complicates the measurement of axial strain. Lubricating fluids and thin sheets of low friction or deformable materials have been interposed between the platten and the sample to reduce friction. The third method is difficult to achieve in practice due to difficulties arising from the need to isolate the pressurised fluid from the free surfaces of the specimen.

In simple shear tests, on the other hand, a bond capable of transmitting shear forces without slip is essential. Raraty and Tabor (1958) conducted a series of tests in which they measured the adhesion properties of ice to various metals. Their results showed that significant differences in specific adhesion exist in regard to the various metals tested, the preparation of the surfaces and the temperature of the bond. The dependence on temperature was interpreted as a difference in the mode of failure: below $-7\,°C$ a brittle form of failure was attributed to the propagation of cracks; above $-7\,°C$ failure was ductile and temperature dependent.

D. S. Russell-Head (personal communication) found that aluminium plates, anodised and then baked to form many minute cracks in the anodised surface, produced a frozen bond with ice stronger than the ice itself. The platten surface had been prepared by washing with a solution of soap and water followed by several hot water rinses.

Specimen geometry

The shape, size and proportions of test specimens are important in insuring the homogeneity of the stress field. An intuitive notion is that the test specimen should at least exhibit a geometric symmetry in conformity with the symmetry of the applied stress configuration. In uniaxial tests this notion suggests a circular cylindrical shape; in simple shear a rectangular shape is implied.

The smallest dimension of a specimen loaded uniaxially is determined primarily by its grain size. Creep tests on polycrystalline ice are intended to represent the bulk properties of the material. Sample diameter should, therefore, be large in comparison to the average grain size. Brace (1960) concluded that the extent of the controlling defect mechanism in rock is of the order of the grain size. Hawkes and Mellor (1970) have assessed the ratio of cross-sectional area unaffected by the free surface in relation to the ratio of mean grain diameter to sample diameter. They concluded that it is desirable to maintain a sample to grain diameter ratio in excess of 20.

As regards specimen length in uniaxial tests, a compromise must be met when considering homogeneity of stress (a long sample is suggested by St. Venant's Principle), stability (a short sample is implied to minimise buckling) strain resolution (a long specimen is preferable) and practical implications.

Unstable creep due to buckling in compression is a direct consequence of either angular misalignment of the plattens or asymetric centering (eccentricity) of the specimen and the plattens. Because an initial misalignment or eccentricity is amplified as creep proceeds, it is particularly important that the specimen be cast and/or machined precisely and that the plattens be accurately bonded to the specimen. Hawke and Mellor (1970) have estimated the error (ratio of peak buckling stress to mean stress) due to eccentric loading to be $8\Delta/D$, where D is the diameter of the specimen, and Δ is the eccentric displacement of the load axis with respect to the specimen axis. The effect of the initial error is proportional to the length of the specimen and is amplified by increased buckling as deformation proceeds.

Angular contact alignment between the load transmitting members of a compression apparatus and the specimen plattens is often accomplished through the use of locking spherical seats. Free spherical seats also limit the net shearing stresses (torsional and lateral) at the platten-sample interface.

The distribution of stress in a uniaxially loaded cylinder with a length to diameter ratio (L/D) of 2 has been provided by Balla (1960), assuming an elastic material with a Poisson's ratio of 0.33, and complete radial restraint with perfect contact at the platten-specimen interfaces. Based on Balla's (1960) reported results, distributed values of τ_o and Λ have been calculated. These distributions are illustrated in Figures 4 and 5, respectively. The figures show only the upper right hand quarter of the cross sections, as the distributions are symmetrical about the centre of the specimen. The contours of Figure 4 have been normalised by the octahedral stress, calculated using equation (2.32). Note the penetration of boundary effects, leading to large gradients of the control parameters τ_o and Λ near the peripheries of the plattens. Based on the contours shown in Figure 4, 28 per cent on the sample volume deviates from the octahedral shear stress calculated with equation (2.32) by more than 10 per cent. Approximately 8 per cent of the sample volume exhibits a stress configuration parameter greater than -0.9; the target value for uniaxial compression is -1.

2.2 STRAIN RATE

The time rate of change of the strain tensor is regarded here as the dependent variable of the flow law. In this section the strain rate tensor is considered. We will use true or logarithmic rate of strain, $\dot{\epsilon} = \frac{1}{l}\frac{dl}{dt}$, in preference to the nominal rate of strain, $\dot{\delta} = \frac{1}{l_o}\frac{dl}{dt}$, where l_o is the initial sample dimension and l is the instantaneous dimension associated with a particular strain rate component; true and nominal strain rates are related by equation (2.43)

$$\dot{\epsilon} = \ln (1 + \dot{\delta}) \tag{2.43}$$

In practice, true and nominal strain rates are essentially equivalent for total strains less than several per cent.

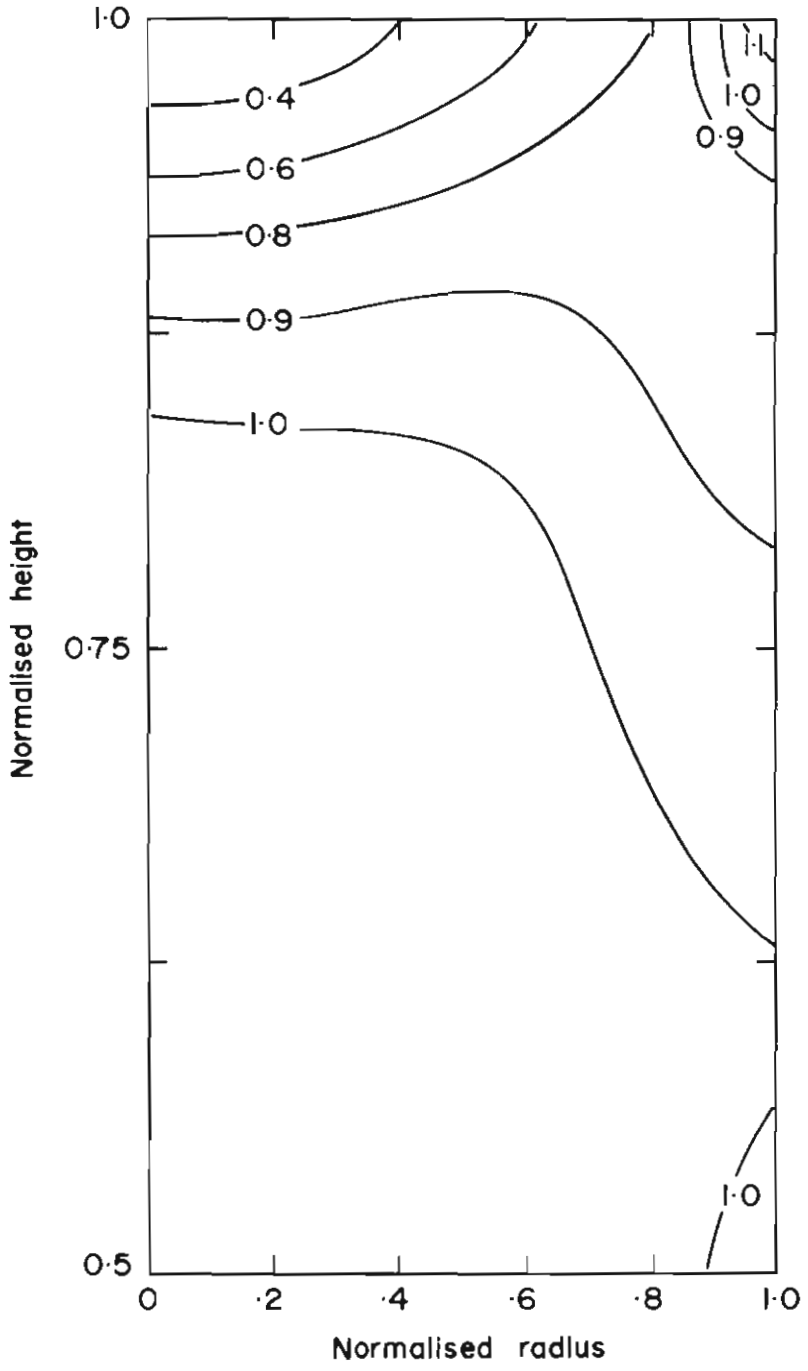

Figure 4. Distribution of normalised octahedral sheer stress for a cylinder of circular cross section in uniaxial compression.

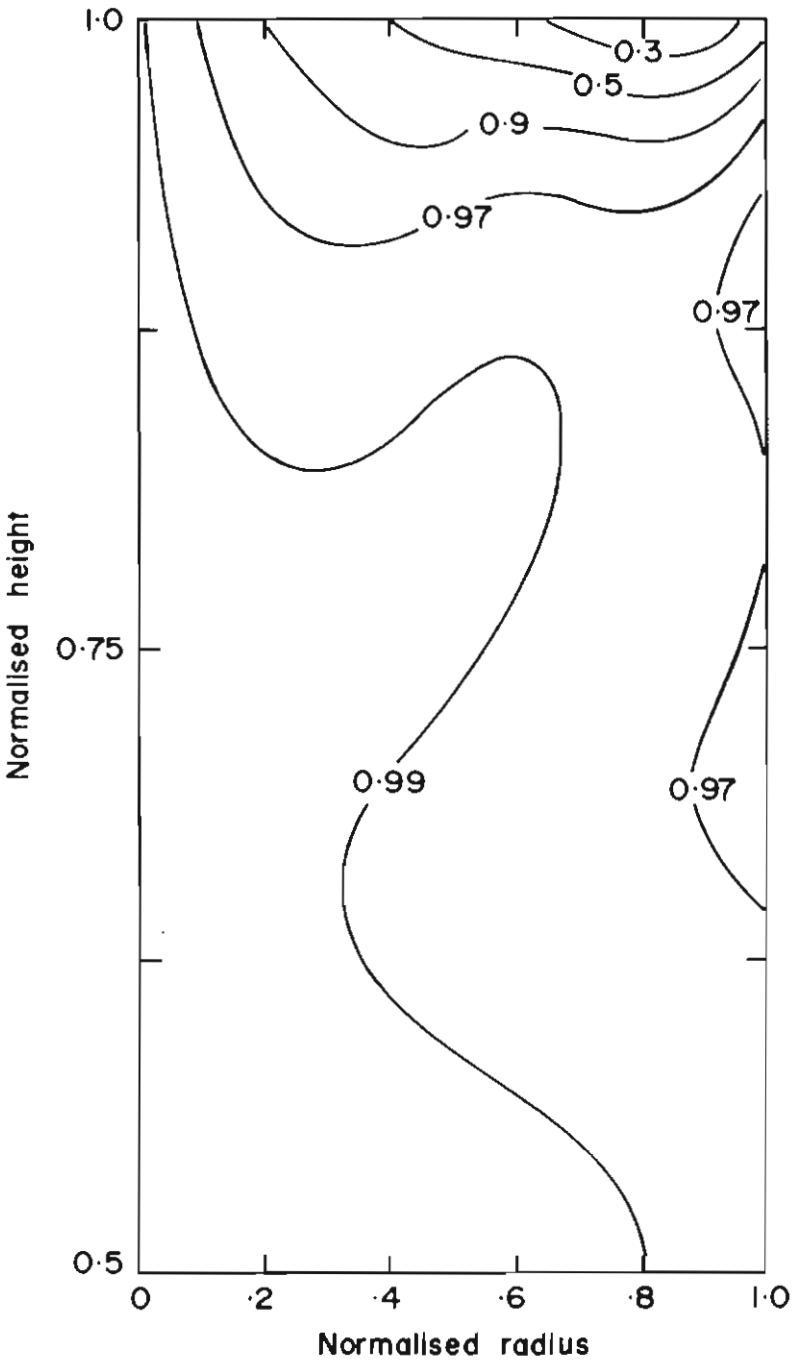

Figure 5. Distribution of stress configuration parameter for a cylinder of circular cross section in uniaxial compression.

2.2.1 The strain rate tensor

Denoting the strain rate tensor in the customary way, we write

$$\dot{\epsilon}_{ij} = \begin{vmatrix} \dot{\epsilon}_{xx} & \dot{\epsilon}_{xy} & \dot{\epsilon}_{xz} \\ \dot{\epsilon}_{yx} & \dot{\epsilon}_{yy} & \dot{\epsilon}_{yz} \\ \dot{\epsilon}_{zx} & \dot{\epsilon}_{zy} & \dot{\epsilon}_{zz} \end{vmatrix} \tag{2.44}$$

where the strain rate components $\dot{\epsilon}_{ij}$ are related to the velocity (u_i) gradients by the expression

$$\dot{\epsilon}_{ij} = u_{j,i} \tag{2.45}$$

The strain rate tensor may be expressed as the sum of symmetric and skew symmetric terms. Thus,

$$\dot{\epsilon}_{ij} = \begin{vmatrix} \dot{\epsilon}_{xx} & \dot{\gamma}_{xy} & \dot{\gamma}_{xz} \\ \dot{\gamma}_{xy} & \dot{\epsilon}_{yy} & \dot{\gamma}_{yz} \\ \dot{\gamma}_{xz} & \dot{\gamma}_{yz} & \dot{\epsilon}_{zz} \end{vmatrix} + \begin{vmatrix} 0 & \dot{\omega}_{xy} & \dot{\omega}_{xz} \\ \dot{\omega}_{xy} & 0 & \dot{\omega}_{yz} \\ \dot{\omega}_{xz} & \dot{\omega}_{yz} & 0 \end{vmatrix} \tag{2.46}$$

where

$$\begin{aligned} \dot{\gamma}_{ij} &= \tfrac{1}{2}(\dot{\epsilon}_{ij} + \dot{\epsilon}_{ji}) \\ &= \tfrac{1}{2}(u_{j,i} + u_{i,j}) \end{aligned} \tag{2.47}$$

and

$$\begin{aligned} \dot{\omega}_{ij} &= \tfrac{1}{2}(\dot{\epsilon}_{ij} - \dot{\epsilon}_{ji}) \\ &= \tfrac{1}{2}(u_{j,i} - u_{i,j}). \end{aligned} \tag{2.48}$$

The first term on the right hand side of equation (2.46) is the deformation rate tensor and represents a pure distortion, while the second term is the rotation rate tensor. The dual of $\dot{\omega}_{ij}$ is the vector rate of rotation. Although rotations play an important part in the interpretation of crystallographic orientation fabrics, they may be neglected in dealing with deformations alone.

The deformation rate tensor may be expressed further as

$$\dot{\gamma}_{ij} = \frac{\Delta}{3} \begin{vmatrix} 1 & 0 & 0 \\ 0 & 1 & 0 \\ 0 & 0 & 1 \end{vmatrix} + \begin{vmatrix} \dot{\epsilon}'_{xx} & \dot{\gamma}_{xy} & \dot{\gamma}_{xz} \\ \dot{\gamma}_{xy} & \dot{\epsilon}'_{yy} & \dot{\gamma}_{yz} \\ \dot{\gamma}_{xz} & \dot{\gamma}_{yz} & \dot{\epsilon}'_{zz} \end{vmatrix} \tag{2.49}$$

where

$$\Delta = \frac{1}{V}\frac{dV}{dt} = \dot{\gamma}_{ij}\,\delta_{ij} \tag{2.50}$$

is the dilitation rate or fractional volume rate of change arising from the deformation, and

$$\dot{\gamma}'_{ij} = \dot{\gamma}_{ij} - \tfrac{1}{3}\,\Delta\,\delta_{ij} \tag{2.51}$$

The first term on the right hand side of equation (2.49) is the spherical rate of deformation while the second term $\dot{\gamma}'_{ij}$ is referred to as the deformation rate deviator and describes the rate of deformation of an incompressible material. With the

exception of the firn layer, the density distribution in glaciers and ice sheets is relatively constant. Unless otherwise noted, incompressible flow is assumed; thus $\Delta \equiv 0$ and $\dot{\gamma}_{ij} = \dot{\gamma}'_{ij}$ in the present text.

Since $\dot{\gamma}_{ij}$ is symmetric, a set of axes called the principal axes of strain or strain rate can be found such that

$$\dot{\gamma}_{ij} = \begin{vmatrix} \dot{\epsilon}_1 & 0 & 0 \\ 0 & \dot{\epsilon}_2 & 0 \\ 0 & 0 & \dot{\epsilon}_3 \end{vmatrix} \tag{2.52}$$

where, by convention, $\dot{\epsilon}_1 \geq \dot{\epsilon}_2 \geq \dot{\epsilon}_3$ are the principal deformation rates parallel to the principal axes of strain. The principal shearing rates analogous to the principal shear stresses are

$$\left.\begin{aligned} \dot{\gamma}_1 &= \tfrac{1}{2}(\dot{\epsilon}_2 - \dot{\epsilon}_3) = \tfrac{1}{2}(\dot{\epsilon}'_2 - \dot{\epsilon}'_3) \\ \dot{\gamma}_2 &= \tfrac{1}{2}(\dot{\epsilon}_1 - \dot{\epsilon}_3) = \tfrac{1}{2}(\dot{\epsilon}'_1 - \dot{\epsilon}'_3) \\ \dot{\gamma}_3 &= \tfrac{1}{2}(\dot{\epsilon}_1 - \dot{\epsilon}_2) = \tfrac{1}{2}(\dot{\epsilon}'_1 - \dot{\epsilon}'_2) \end{aligned}\right\} \tag{2.53}$$

2.2.2 Invariants

Compressibility and pure shear

The first invariant of the deformation rate tensor may be written

$$\begin{aligned} J_1 &\equiv \dot{\gamma}_{ij}\,\delta_{ij} \\ &= \dot{\epsilon}_1 + \dot{\epsilon}_2 + \dot{\epsilon}_3 \end{aligned} \tag{2.54}$$

Thus J_1 is physically equivalent to the dilitation rate $\Delta = \dfrac{1}{V}\dfrac{dV}{dt}$.

For $\Delta = 0$, the flow is incompressible and called a pure shear deformation.

Octahedral and effective rate of deformation

The second invariant of the deviatoric deformation rate tensor is

$$\begin{aligned} J'_2 &\equiv \tfrac{1}{2}\dot{\gamma}'_{ij}\,\dot{\gamma}'_{ij} \\ &= \tfrac{1}{6}[(\dot{\epsilon}_2 - \dot{\epsilon}_3)^2 + (\dot{\epsilon}_3 - \dot{\epsilon}_1)^2 + (\dot{\epsilon}_1 - \dot{\epsilon}_2)^2] \\ &= \tfrac{2}{3}(\dot{\gamma}_1^2 + \dot{\gamma}_2^2 + \dot{\gamma}_3^2) \end{aligned} \tag{2.55}$$

Jaeger (1969) shows that the octahedral shear rate of deformation

$$\dot{\gamma}_o = (\dot{\gamma}_{ij}\,\dot{\gamma}_{ij}/3)^{1/2} = \left(\frac{2J'_2}{3}\right)^{1/2} \tag{2.56}$$

is the shear deformation rate resolved on the octahedral plane, possessing direction cosines $(3)^{-1/2}$ referred to the principal axes. Alternately, Nye (1957) defines the effective shear rate as

$$\dot{\gamma}_e = (J'_2)^{1/2} = \frac{\sqrt{3}}{2}\,\dot{\gamma}_o \tag{2.57}$$

$$\dot{\omega}_{ij} = \begin{vmatrix} 0 & 0 & -\frac{\dot{\gamma}}{2} \\ 0 & 0 & 0 \\ \frac{\dot{\gamma}}{2} & 0 & 0 \end{vmatrix} \tag{2.68}$$

Thus simple shear, or laminar, flow may be regarded as a pure shear in two dimensions plus a rigid rotation about the second principal axis at a rate $\dot{\gamma}/2$.

2.3 ICE STRUCTURE

The specification and analysis of ice structure in conjunction with creep tests of polycrystalline ice is an area too often neglected in laboratory flow law studies. The inconsistency and scatter illustrated in a graphical summary of deformation studies in Figure 1, reflect the variety of ice structural types examined. It is clear from the limited evidence available that a number of structural parameters enter into the flow law for polycrystalline ice. In this section several parameters commonly considered to be among the most important are discussed.

2.3.1 Anisotropy

That crystallographic anisotropy plays an important role in the flow law for polycrystalline ice can be inferred from the results of studies on the shear deformation of single crystals of ice. Shumskiy (1958), Rigsby (1958, 1960), Butkovich and Landauer (1958) and Vialov (1958) have shown that single crystals oriented for easy glide deform at a rate 10^2 to 10^3 times faster than single crystals oriented for hard glide under similar conditions of temperature and applied stress. Qualitative results concerned with the influence of anisotropy on the deformation rates of polycrystalline specimens are available from creep tests on anisotropic specimens and on specimens developing preferred orientations under stress (Steinemann 1954, Kamb 1972, Rigsby 1960, Budd and Matsuda 1974, Dillon and Andersland 1967, Gold 1973 and Frederking 1972). These results confirm the view that polycrystalline deformation rates are enhanced when preferred orientation fabrics are compatible with the stress situation and that compatible preferred orientations are induced by the flow situation. Budd (1972) presents substantial evidence that such preferred orientations are a pervasive feature of natural ice masses and are compatible with the overall flow picture.

Quantitative studies related directly to the effects of anisotropy alone are nearly non-existent. Thus, as a major part of the present study a first model of the effects of crystallography on the flow law for polycrystalline ice is presented (Section 3). A precise parameterisation of a crystallographic orientation fabric will be required. Most fabric data are presented as scatter diagrams on an equal area (Schmidt net) projection of the lower hemisphere distribution (Phillips 1971). These distributions

are often contoured in terms of the number fraction or per cent of the oriented crystals per 1 per cent area of the Schmidt net. As it may be expected that the influence of a constituent crystal on the flow law for an aggregate is in proportion to its size, a more relevant quantity would be the orientational distribution per unit volume of the aggregate rather than number of crystals per unit area in the thin section (Budd 1972). While a volume-related orientation density cannot be obtained directly from a single thin section, an area-related distribution may be obtained by weighting each oriented crystal with its area fraction of the total thin section area. Then, if the crystal size and shape distributions are known for the aggregate (Rigsby 1968) it is possible to estimate the volumetric orientational distribution from the area distribution (Steinemann 1958a). Hooke (1969) argues that for an aggregate of grains equant in three dimensions, differences between the various distributions should be negligible.

It would appear practical, then, to define the crystallographic orientation density f as the volume fraction per steradian of an aggregate of total volume V possessing optic axes oriented within the elemental solid angle d Ω:

$$f = \frac{1}{V}\frac{dV}{d\Omega} \tag{2.69}$$

It follows that for an isotropic aggregate the orientation density is

$$f = f' = (2\pi)^{-1}. \tag{2.70}$$

2.3.2 Density

The evidence presented by Mellor and Smith (1966) regarding the effect of density on the strain rate of snow clearly indicates a decrease in strain rate with an increase in density. They have associated a 'step' in their curves between 0.53 and 0.64 MN m^{-3} with the attainment of the maximum practical density for close packed grains and close packed spheres within this range. They argue further that this limit is responsible for a transition in the rate controlling mechanisms. Budd (1969) extrapolated the curves of Mellor and Smith to the maximum density for ice and concluded that the resulting strain rates were consistent with the results of other workers. Budd (1969) also noted that the density of naturally deforming ice below the surface firn of glaciers and ice sheets is generally high and constant, arguing that since the firn layer is but a small fraction of the total depth in most ice caps and glaciers, density effects on strain rates may be neglected.

2.3.3 Texture

Few results are available concerning the effect of texture (grain size and shape) on the creep of polycrystals. The results of Butkovitch and Landauer (1960) indicate a tendency for higher strain rates to be associated with increased grain size. However, this trend cannot be separated from the effects of anisotropy in their test specimens. It is known that the range of crystal size can extend over two orders of magnitude at a single site. For this reason, the effect of texture on the flow law is an important area for future investigation.

2.3.4 Inclusions

Interstitial, intergranular and intragranular inclusions have an effect on the deformation rate of polycrystalline ice. In relation to natural ice masses, moranic material may play an important role as it is often observed in the basal region, where shearing stresses are large.

Nayar (1966) investigated the effects of small volume concentrations of dispersed ultrafine amorphous silica particles in a polycrystalline ice matrix. For concentrations between 0 and 1 per cent by volume, he noted a decrease of strain rate with increasing concentration. At 1 per cent concentration the strain rate decreased by a factor of from ten to thirty with respect to pure polycrystalline ice. This inverse dependence was greatest at low concentrations and low temperatures. Nayar suggested a mechanism of cross slip enabling dislocations to bypass particles.

The effect of volume concentrations up to 35 per cent dispersed fine sand has been studied by Hooke et al. (1972). Again a reduction of strain rate with increased particle concentration was found. Analysing their results in terms of dispersion hardening, Hooke et al. viewed each particle as surrounded by a cloud of tangled dislocations. At higher volume fractions of sand, the effective volume fraction of ice increases at a rate less than the volume fraction of sand due to the overlap of spheres of influence of adjacent particles — thus the observed exponential law relating volume fraction sand to strain rate.

At volume fractions less than about 0.1 the results of Hooke et al. were inconsistent: they concluded that at small concentrations individual particles might be acting as dislocation sources or decreasing the nominal crystal size, thereby promoting grain boundary slip.

Goughnour and Andersland (1968) reported experimental results on the creep of a sand-ice system with volume concentrations extending to 60 per cent. Displaying their results in terms of peak strength, they obtained a bi-linear distribution of strength against concentration. Strength increased slowly to a critical concentration of approximately 42 per cent; at higher concentration the strength of the sand-ice system increased sharply. The sharp increase in strength above the critical concentration was attributed to dilatency and friction between sand particles.

Clearly the gross effects of dispersed particles is complicated by many factors including the size, geometry and concentration of the particles. Whether particulate inclusions act as sources or barriers for dislocations remains unclear. It is the contention of the author that the role of particulate inclusions may be related to position within the polycrystalline matrix relative to the grain boundaries. Intracrystalline particle placement can be expected to preferentially influence intracrystalline creep mechanisms. The placement of particles relative to grain boundaries would then govern the rate-controlling mechanism and thus explain some of the observed scatter, especially at low concentration.

2.4 TEMPERATURE

The control of the thermal environment of a specimen and creep apparatus is essential to the successful interpretation of creep data, especially at low values of creep rate. Temperature variations influence not only the creep rate, but also the dimensional

stability of the specimen and apparatus, and the extent to which thermal stresses become important. In addition, most electrical displacement transducers exhibit both mechanical and electrical sensitivity to temperature variation. In this section, the effects of temperature variations on the creep rate functions and the requirements of temperature control used in the present study are considered.

There are two types of variations: those showing no well-defined periodicity, or relatively long periods compared to the duration of the test; and those represented by a periodic fluctuation with no variation of the mean value. Each type of variation contributes to the form of the creep function and can mask the real deformational

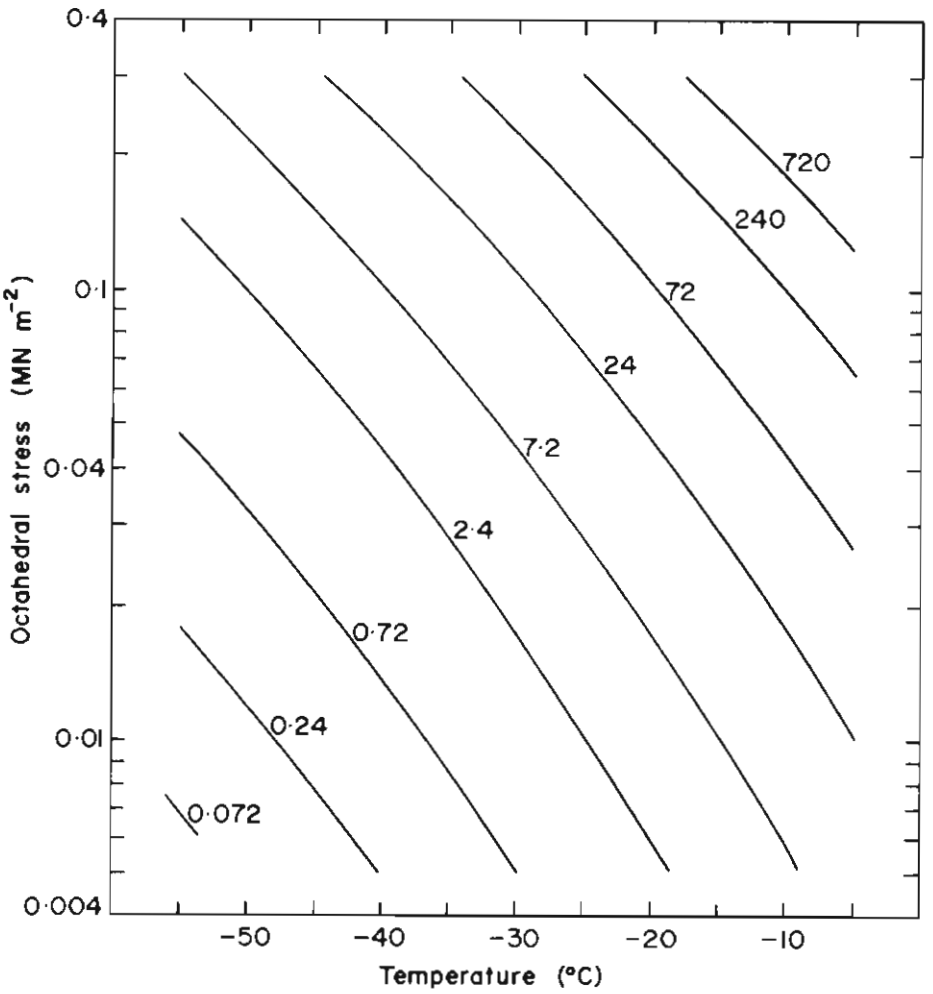

Figure 6. Temperature drift (millidegrees per day) versus temperature and octahedral sheer stress which will introduce a 10% error in observed octahedral strain rate. (Based on Budd's (1969, Figure 2.3) idealised extrapolation of previous empirical results to low temperatures and shear stresses).

contribution to its form. The linear thermal coefficient of expansion for ice is approximately $5 \times 10^{-5}\,°C^{-1}$; that is, a temperature change of 1 °C causes a thermal strain of 5×10^{-5}. As an indication of the importance of this masking effect at low temperatures and small shear stresses, Figure 6 shows the magnitude of temperature drift rate which will introduce an error of 10 per cent in observed octahedral strain rates. The rheological strain rates on which Figure 6 is based have been taken from Budd's (1969, his Figure 2.3) idealised extrapolation of previous empirical results to low temperatures and small strain rates. Clearly, Figure 6 indicates that below about 0.02 MN m^{-2} and $-20\,°C$ the precise control of temperature drift rate is essential.

Of equal concern at small creep rates, where the specimen may not reach a steady secondary creep rate even during a prolonged test, is the necessity of estimating the secondary creep rate from the form of the creep function during the primary stage. When thermal equilibrium within the test chamber has not been established at the time of loading, the specimen and apparatus temperatures may be expected to exhibit a transient, exponential approach to equilibrium, thus superimposing an exponential component of thermal strain on the creep function. Depending on the direction of approach to equilibrium, this effect may either diminish or enhance the real transient primary creep response as seen in the observed creep function. The duration of the thermal transient response can usually be measured or estimated and the effected creep data neglected. It might be noted that this effect must be considered if Glen's (1958) method is used to estimate secondary creep rates from the initial slope of the creep function.

Periodic fluctuations of temperature within the test chamber are revealed as periodic fluctuations of the observed displacement or creep functions. Observed periods longer than that of the actual thermal cycle may be misleading, arising from systematic differences between the data sampling rate and the period of the thermal cycle (Blackman and Tukey 1958). This effect is most pronounced with the use of an automatic data logger. The principle problem here is to separate the thermally induced fluctuations in the observed creep function from real fluctuations in creep rate (Budd and Matsuda 1974, Duval 1972, Gifkins 1959, and Richardson et al. 1966).

An additional, though usually minor, concern is the inducement of thermal gradients arising from a rapid rate of temperature change. These in turn generate thermal stresses within the specimen. Although thermal stresses are unlikely to cause fracture at elevated temperatures, fractures may become a real possibility at low temperatures where the ice is more brittle. Of greater importance at low stress magnitudes is the modification to the state of stress which can be caused by a superimposed thermal state of stress.

Certainly the most satisfactory solution is to minimise temperature variations to a level where the effects mentioned above become negligible.

3. The effect of anisotropy on the creep of polycrystalline ice

Empirical flow laws for polycrystalline ice presently in use are based for the most part on the suite of existing data relating to tessellate, fine-grained, randomly oriented polycrystals. In this chapter a model relating the deformation rate of an anisotropic polycrystal to that of an isotropic polycrystal is developed in terms of an enhancement factor. The utility of this approach is evident; once the stress and temperature region over which the model is applicable have been determined on the basis of a limited number of carefully designed laboratory experiments, an anisotropic flow law for polycrystalline ice in that region can be readily deduced for any crystallographic orientation fabric on the basis of established isotropic results through the application of the results of the present model.

3.1 INTRODUCTION

Consider an aggregate in which the octahedral strain rate $\dot{\epsilon}_o$ is a function of the Root Mean Square-resolved basal shear stress, as might be expected if the rate controlling mechanism is basal glide. It is shown in Section 3.2.1 that the shear stress τ_B resolved on a basal plane with direction cosines l_i relative to the principal axes of stress is

$$\tau_B = \alpha \tau_o \tag{3.1}$$

where

$$\alpha = \frac{3}{\sqrt{2}} \left[\frac{(\Lambda - 1)^2 l_2^2 l_3^2 + 4 l_1^2 l_3^2 + (\Lambda + 1)^2 l_1^2 l_2^2}{\Lambda^2 + 3} \right]^{1/2} \tag{3.2}$$

is the geometric (stress) factor (Weertman 1973) for the grain.

Defining the r.m.s.-resolved basal shear stress for an aggregate of total volume V as

$$\tau_{rms} = \left[\frac{1}{V} \int_V \tau_B^2 \, dV \right] \tag{3.3}$$

and substituting equations (3.1) and (2.69) gives

$$\tau_{rms} = \left[\frac{1}{2\pi} \int \alpha^2 d\Omega \right]^{1/2} \tau_o \tag{3.4}$$

The integral in equation (3.4) may be evaluated for an isotropic aggregate using

$$\left.\begin{aligned} l_1 &= \sin\theta\cos\alpha \\ l_2 &= \sin\theta\sin\alpha \\ l_3 &= \cos\theta \\ d\Omega &= \sin\theta\, d\theta\, d\alpha \end{aligned}\right\} \tag{3.5}$$

then

$$\begin{aligned} \frac{1}{2\pi}\int f'\alpha^2 d\Omega &= \frac{9}{4\pi}(\Lambda^2+3)^{-1}\int_0^{2\pi}\int_0^{\frac{\pi}{2}}[(\Lambda-1)^2\sin^3\theta\cos^2\theta\sin^2\alpha \\ &\quad + 4\sin^2\theta\cos^2\theta\cos^2\alpha \\ &\quad + (\Lambda+1)^2\sin^2\theta\sin^2\alpha\cos^2\alpha]\, d\theta\, d\alpha \\ &= \frac{9}{4}(\Lambda^2+3)^{-1}\int_0^{\frac{\pi}{2}}[(\Lambda-1)^2\sin^3\theta\cos^2\theta \\ &\quad + 4\sin^3\theta\cos^2\theta \\ &\quad + \frac{1}{4}(\Lambda+1)^2\sin^3\theta]\, d\theta \\ &= \frac{3}{10}(\Lambda^2+3)^{-1}[(\Lambda-1)^2+4+(\Lambda+1)^2] \\ &= \frac{3}{10}(\Lambda^2+3)^{-1}2(\Lambda^2+3) \\ &= \frac{3}{5} \end{aligned} \tag{3.6}$$

which is notably independent of A. If, as proposed above, $\dot{\epsilon}_o$ is a function of τ_{rms}, the implication of equation (3.6) is that for an isotropic aggregate $\dot{\epsilon}_o$ is a function of τ_o and not of stress configuration. This suggests a flow law of the form (Nye, 1953)

$$\dot{\epsilon}_o = \lambda(\tau_o)\,\tau_o. \tag{3.7}$$

The large suite of empirical creep data applicable to isotropic ice presently available indicates (cf. Weertman 1973) that $\dot{\epsilon}_o \propto \tau_o^n$, implying (Nye 1953 and Langdon 1973) that $\lambda \propto (\tau_o/G)^{n-1}$ where G is the shear modulus for ice.

Weertman (1963) viewed an ice polycrystal as a collection of grains deforming independently by basal glide governed by a monocrystalline flow law of the form

$$\dot{\epsilon}_B = \lambda_B(\tau_B)\,\tau_B = \lambda_B(\tau_o)\,\alpha^n\,\tau_o, \tag{3.8}$$

where $\dot{\epsilon}_B$ is the basal rate of glide and $\lambda_B \propto (\tau_B/G)^{n-1}$ is the basal fluidity. Assuming an isotropic aggregate in uniaxial compression under an axial stress $\sigma_a (= 3/\sqrt{2}\tau_o$, page 20) and using an axial geometric strain rate factor (b_a) to resolve $\dot{\epsilon}_B$ into its axial component, he found the average resolved axial srrain rate to be

$$\bar{\dot{\epsilon}}_a = \lambda_B \beta \overline{b_a \alpha^n} \tau_o \tag{3.9}$$

An additional factor [β] was introduced to account for effects of intergranular interference; the factor ($\lambda_B \beta \overline{b_a \alpha^n}$) is the axial fluidity of the aggregate. As the axial geometric strain rate factor is only one component of a general transformation tensor b_{ij} (Section 3.2.1) equation (3.9) may be written for each component of $\bar{\dot{\epsilon}}_{ij}$ as

$$\bar{\dot{\epsilon}}_{ij} = \lambda_{ij} \tau_o. \tag{3.10}$$

Also, since α is known in terms of Λ (equation 3.2), equation (3.10) may be regarded as a flow law for anisotropic ice deforming by basal glide in an arbitrary state of stress. The tensor fluidity $\lambda_{ij} = \lambda_B \beta \overline{b_{ij} \alpha^n}$ accounts for the effects of f and Λ through the composite geometric tensor

$$\bar{\alpha}_{ij} = \overline{b_{ij} \alpha^n} = \frac{1}{2\pi} \int f\, b_{ij}\, \alpha^n(\Lambda)\, d\Omega \tag{3.11}$$

If the symmetric part of $\bar{\alpha}_{ij}$ is written $\bar{g}_{ij}$, then the aggregate octahedral deformation rate is $\bar{\dot{\gamma}}_o = \lambda_o \tau_o$, where

$$\lambda_o = \lambda_B \beta(f, \Lambda)\, \bar{g}_o(f, \Lambda). \tag{3.12}$$

Consider two aggregates differing only with regard to their orientation fabrics and deforming under identical conditions of temperature, state of stress, etc. If one is isotropic, the ratio of their octahedral deformation rates is

$$\begin{aligned} E &= \frac{\bar{\dot{\gamma}}_o(f, \Lambda)}{\bar{\dot{\gamma}}_o(f')} \\ &= \frac{\lambda_o(f, \Lambda)}{\lambda_o(f')} \\ &= \frac{\beta(f, \Lambda)\, \bar{g}_o(f, \Lambda)}{\beta(f')\, \bar{g}_o(f')} \end{aligned} \tag{3.13}$$

or

$$\bar{\dot{\gamma}}_o(f, \Lambda) = E\, \bar{\dot{\gamma}}_o(f') \tag{3.14}$$

Equation (3.14) provides a flow law for an abritary orientation fabric and state of stress through application of the enhancement factor E to the flow law for an isotropic aggregate.

As a first step toward the development of a generalised flow law for an anisotropic aggregate, the results to be expected from equation (3.13) for a linear stress-strain rate dependence (n = 1) are now examined. This value of n deserves some comment. Empirical results indicate that n is a decreasing function of decreasing octahedral shear stress, approaching the limiting value of unity at small octahedral shear stresses (say less than 0.05 MN m^{-2}). Theoretical considerations (Weertman 1973, 1968 and Langdon 1973) on the other hand, predict values of n ranging between 2 and 4.5, depending on the assumed rate controlling mechanism, which are independent of octahedral shear stress. Weertman (1969, 1973) believes that the apparent contradiction

between theoretical and empirical results is due to the necessarily short-term (with regard to total strain) tests at the small octahedral shear stresses in question. The factor $(\tau_o/G)^{n-1}$ of the fluidity (Nye 1953 and Langdon 1973) arises from the expression for dislocation density which is often treated as a function of total strain (Higashi 1967 and Wakahama 1967). If this is the case, Weertman (1969, 1973) argues that the duration of creep tests at small octahedral shear stresses is insufficient for the dislocation density to increase to its final value, and concludes that the linear shear stress dependence observed is due to the dominance of the linearly stress dependent dislocation velocity at small strains (see also Gilman 1968).

Whether the linear dependence of $\dot{\epsilon}_o$ on τ_o at low octahedral shear stresses is a result of a real variation in the exponent n due to an inadequate theoretical description of the functional form of the dislocation density, or, as concluded by Weertman (1969, 1973), a result of the practical limitations placed on the duration of creep tests, must await further theoretical and laboratory results to be resolved (cf. Sinha 1977). It may be noted, however, that field results also indicate a trend toward n values approaching unity at low values of τ_o. The various explanations of the apparent linear dependence notwithstanding, empirical laboratory data at small octahedral shear stresses can evidently be represented by an n value of one.

The geometric tensor, interference factor and enhancement factor are developed in Sections 3.21, 3.2.4 and 3.3, respectively. External flow constraints are incorporated into the model in Section 3.2.2.

3.2 THE MODEL

3.2.1 The geometric tensor

Let the unit-vector normal to a given basal plane be specified by its direction cosines (l_1, l_2, l_3) with respect to the principal axes of stress. A general expression for the resolved basal shear stress vector, t_i is required. The total stress vector s_i acting across the given plane has components (Jaeger 1969)

$$\left.\begin{aligned} s_1 &= l_1\,\sigma_1 \\ s_2 &= l_2\,\sigma_2 \\ s_3 &= l_3\,\sigma_3 \end{aligned}\right\} \tag{3.15}$$

where σ_1, σ_2, and σ_3 are the principal stresses. The components t_i of the resolved basal shear stress are

$$\left.\begin{aligned} t_1 &= l_1\,[l_3^2\,(\sigma_1 - \sigma_3) + l_2^2\,(\sigma_1 - \sigma_2)] \\ t_2 &= l_2\,[l_1^2\,(\sigma_2 - \sigma_1) + l_3^2\,(\sigma_2 - \sigma_3)] \\ t_3 &= l_3\,[l_1^2\,(\sigma_3 - \sigma_1) + l_2^2\,(\sigma_3 - \sigma_2)] \end{aligned}\right\} \tag{3.16}$$

Substitution of equation (2.6) into equation (3.16) for the principal shear stresses in terms of the principal stress differences yields

$$\left.\begin{aligned} t_1 &= 2l_1\,[2_3^2\,\tau_2 + l_2^2\,\tau_3] \\ t_2 &= 2l_2\,[l_1^2\,\tau_3 + l_3^2\,\tau_1] \\ t_3 &= 2l_3\,[l_1^2\,\tau_2 + l_2^2\,\tau_1] \end{aligned}\right\} \qquad (3.17)$$

Further substitution of equation (2.26) into equation (3.17) yields the resolved shear stress in terms of the stress situation parameters τ_o and Λ.

$$\begin{aligned} t_1 &= \frac{3\,l_1}{\sqrt{2}}\left[\frac{2l_3^2 + (\Lambda + 1)\,l_2^2}{(\Lambda^2 + 3)^{1/2}}\right]\tau_o \\ t_2 &= -\frac{3\,l_2}{\sqrt{2}}\left[\frac{(\Lambda + 1)\,l_1^2 + (\Lambda - 1)\,l_3^2}{(\Lambda^2 + 3)^{1/2}}\right]\tau_o \\ t_3 &= \frac{3\,l_3}{\sqrt{2}}\left[\frac{(\Lambda - 1)\,l_2^2 - 2l_1^2}{(\Lambda^2 + 3)^{1/2}}\right]\tau_o \end{aligned} \qquad (3.18)$$

The magnitude of the resolved shear stress is

$$\tau_B = (t_i\,t_i)^{1/2} = \alpha\,\tau_o \qquad (3.19)$$

where

$$\alpha = \frac{3}{\sqrt{2}}\left[\frac{(\Lambda - 1)^2\,l_1^2 l_3^2 + 4l_1^2 l_3^2 + (\Lambda + 1)\,l_1^2 l_2^2}{\Lambda^2 + 3}\right]^{1/2} \qquad (3.20)$$

is the geometric (stress) factor (Weertman, 1973) for the grain.

Assuming that the basal glide direction is parallel to the resolved shear stress (Kamb, 1961), the basal glide rate is

$$\dot{\epsilon}_B = \lambda_B\,\tau_B = \lambda_B\,\alpha\,\tau_o \qquad (3.21)$$

Defining a co-ordinate system associated with the basal plane such that x_1^B is parallel to t_i and x_3^B is parallel to l_i, the strain rate tensor for simple shear (page 45) on the basal plane is

$$\dot{\epsilon}_{ij}^B = \begin{vmatrix} 0 & 0 & 0 \\ 0 & 0 & 0 \\ \dot{\epsilon}_B & 0 & 0 \end{vmatrix} \qquad (3.22)$$

It will be convenient to express the strain rate tensor of each grain in a common co-ordinate system. The obvious choice is the system defined by the principal stress axes of the applied load. The transformation law for a rotation of axes is

$$\dot{\epsilon}_{kl} = c_{ik}c_{jl}\,\dot{\epsilon}_{ij}^B \qquad (3.23)$$

where c_{pq} is the cosine of the angle between the positive x_p^B axis and the positive x_q axis. Since the only non-vanishing component of $\dot{\epsilon}_{kl}^B$ is $\dot{\epsilon}_{31}^B = \dot{\epsilon}_B$, the strain rate in the principal stress co-ordinate system is

$$\dot{\epsilon}_{kl} = c_{3k}c_{2l}\,\dot{\epsilon}_B = \lambda_B\,c_{3k}c_{1l}\,\alpha\,\tau_o \qquad (3.24)$$

where

$$c_{3k} = l_k \tag{3.25a}$$

and

$$c_{1l} = t_l/\tau_B. \tag{3.25b}$$

The product $b_{kl} = c_{3k}c_{1l}$ is a geometric strain rate factor (cf. Weertman 1963) for the grain. Let the geometrically related factors in equation (3.24) be absorbed into the composite geometric tensor

$$\alpha_{kl} = c_{3k}c_{2l}\,\alpha = b_{kl}\,\alpha$$
$$= \frac{3}{\sqrt{2}}\left[\frac{(\Lambda-1)^2 l_2^2 l_3^2 + 4l_1^2 l_3^2 + (\Lambda+1)^2 l_1^2 l_2^2}{\Lambda^2+3}\right]^{-1/2} b_{kl}. \tag{3.26}$$

The tensor α_{kl} may be written as the sum of a symmetric term g_{kl} and anti-symmentric term w_{kl}:

$$\alpha_{kl} = g_{kl} + w_{kl} \tag{3.27}$$

where

$$g_{kl} = \frac{3}{\sqrt{2}(\Lambda^2+3)^{1/2}} \begin{vmatrix} l_1[l_2^2(\Lambda+1)+2l_3^2] & l_1l_2[(l_2^2-1/2)(\Lambda+1)+2l_3^2] & l_1l_3[\Lambda l_2^2+l_3^2-l_1^2] \\ l_1l_2[(l_2^2-1/2)(\Lambda+1)+2l_3^2] & -l_2[l_1^2(\Lambda+1)+l_3^2(\Lambda-1)] & l_2l_3[(l_2^2-1/2)(\Lambda-1)-2l_1^2] \\ l_1l_3[\Lambda l_2^2+l_3^2-l_1^2] & l_2l_3[(l_2^2-1/2)(\Lambda-1)-2l_1^2] & l_3[l_3^2(\Lambda-1)-2l_1^2] \end{vmatrix} \tag{3.28}$$

and

$$w_{kl} = \frac{3}{\sqrt{2}(\Lambda^2+3)^{1/2}} \begin{vmatrix} 0 & -1/2\,l_1l_2(l+1) & -l_1l_3 \\ 1/2\,l_1l_2(\Lambda+1) & 0 & 1/2\,l_2l_3(\Lambda-1) \\ l_1l_3 & -1/2\,l_2l_3(\Lambda-1) & 0 \end{vmatrix} \tag{3.29}$$

The geometric tensor α_{kl} for an individual grain relates its strain rate tensor in principal stress co-ordinates to the applied octahedral stress through the geometry of its c-axis orientation $\vec{l}$ and the stress configuration parameter Λ. This geometric tensor is a generalised form of the scalar geometric factor (Weertman 1963 and Gilman 1968) to which α_{33} is analogous for uniaxial compression. To illustrate this point, consider a specimen in uniaxial compression ($\Lambda = -1$). The compression axis is x_3. The geometric factor for the axial component of the strain rate tensor is accordingly α_{33}. Equation (3.28) for α_{33} with $\Lambda = -1$ becomes

$$\alpha_{33} = \frac{-3}{2\sqrt{2}}\, l_3^2[2l_2^2 + 2l_1^2]$$
$$= \frac{-3}{\sqrt{2}}\, l_3^2[1 - l_3^2] \tag{3.30}$$

Let the unit vector l_i normal to the basal plane of a particular grain make an angle θ with respect to the compressive axis. Then $l_3 = \cos\theta$, and

$$\alpha_{33} = \frac{-3}{\sqrt{2}} \sin^2\theta \cos^2\theta, \tag{3.31}$$

[cf. expression (3.31) above with Weertman's (1963) discussion of the geometric factor leading to his equation (3); Gilman's (1968) discussion of the geometric factor in his equation (16); and Wakahama's (1967) equation (1)]. Note, however, that α_{ij} yields a geometric factor of each component of the strain rate tensor of an individual grain for an arbitrary stress configuration. An aggregate geometric tensor is required to obtain the octahedral strain rate of an anisotropic aggregate.

3.2.2 The effective fluidity of a non-interacting aggregate

Setting the bulk strain rate resulting from the intragranular deformation of non-interacting grains equal to the volumetric mean granular rate of strain (cf. Weertman 1963) yields

$$\bar{\dot{\epsilon}}_{ij} = \frac{1}{V} \int_V \dot{\epsilon}_{ij}\, dV. \tag{3.32}$$

Substitution of equation (2.69) replaces the volume integral of expression (3.32) with a spherical angle integral over all possible basal plane orientations:

$$\begin{aligned} \bar{\dot{\epsilon}}_{ij} &= \int_{2\pi} f\dot{\epsilon}_{ij}\, d\Omega \\ &= \lambda_B \tau_o \int_{2\pi} f\alpha_{ij} d\Omega \\ &= \bar{\alpha}_{ij}\lambda_B\tau_o \end{aligned} \tag{3.33}$$

where

$$\bar{\alpha}_{ij} = \int_{2\pi} f\alpha_{ij} d\Omega \tag{3.34}$$

The weighting function for each orientation is the volume fraction of the specimen possessing that orientation, i.e. the crystallographic orientation density, f. It follows that the bulk octahedral strain rate is

$$\begin{aligned} \bar{\dot{\epsilon}}_{oN} &= (\bar{\dot{\epsilon}}_{ij}\, \bar{\dot{\epsilon}}_{ij}/3)^{1/2} \\ &= \lambda_B\, \tau_o\, (\bar{\alpha}_{ij}\, \bar{\alpha}_{ij})^{1/2} \\ &= \bar{\alpha}_o\, \lambda_B\, \tau_o \end{aligned} \tag{3.35}$$

where

$$\bar{\alpha}_o = (\bar{\alpha}_{ij}\, \bar{\alpha}_{ij}/3)^{1/2}. \tag{3.36}$$

Similarly, the octahedral deformation rate is

$$\bar{\dot{\gamma}}_{oN} = \lambda_B \tau_o (\bar{g}_{ij}\bar{g}_{ij}/3)^{1/2}$$

$$= \bar{g}_o \lambda_B \tau_o \tag{3.37}$$

with

$$\bar{g}_o = (\bar{g}_{ij}\bar{g}_{ij}/3)^{1/2} \tag{3.38}$$

The effective fluidity of the non-interacting aggregate is thus

$$\lambda_{oN} = \lambda_B \bar{g}_o \tag{3.39}$$

The subscript N is a reminder that the associated parameter refers to an aggregate of non-interacting grains.

3.2.3 Satisfaction of external flow constraints

In this section external boundary constraints imposed on the aggregate as a whole are considered. These conditions or constraints are generally specified in terms of velocities, either by direct measurement, e.g. of the surface velocity component, or inference, e.g. by the presence of rigid bedrock boundaries. For a laboratory creep test, boundary conditions on the velocities are given by the platten constraints. It is useful, therefore, to exhibit the bulk unconstrained strain rate tensor in a co-ordinate system (x_i^p) associated with the platten geometry. The simplest creep device capable of generating all possible states of stress (though not all possible states of flow, since the rotational flow field cannot be varied independently) is one incorporating a single set of parallel opposed plattens. When the applied load is a single-valued composite of a shear load and a normal load, the results on page 20 show that the second principle stress axis is oriented parallel to the platten faces and normal to the shear load. Thus it is convenient to choose the platten-associated co-ordinate system such that x_1^p is parallel to the applied shear load and x_3^p is normal to the plattens. Let the orientation of the principal stress axes be specified by the transformation tensor p_{ij} which relates tensor and vector components in the principal stress co-ordinate system to their components in the x_i^p system. The load-induced strain rate tensor expressed in the platten system is then

$$\bar{\dot{\epsilon}}_{kl}^p = p_{ik}\, p_{jl}\, \bar{\dot{\epsilon}}_{ij}. \tag{3.40}$$

As the fundamental notion of an anisotropic material suggests that the components of strain rate are not necessarily proportional, respectively, to those of the applied stress, an anisotropic specimen need not deform in sympathy with the applied load. If the plattens are constrained against rotations or against translation, reactive couples and/or stress situations may develop, forcing the bulk flow field into conformity with the platten constraints.

Let a double overbar denote a parameter which fully satisfies the platten constraints. There are three possible translational constraints:

(a) $\bar{\bar{u}}_{3,3}^p = \bar{\bar{\epsilon}}_{33}^p = 0$ ($\bar{\bar{\alpha}}_{33}^p = 0$), plattens remain equidistant (simple shear);

(b) $\bar{\bar{u}}_{2,3}^p = \bar{\bar{\epsilon}}_{32}^p = 0$ ($\bar{\bar{\alpha}}_{32}^p = 0$), no platten translation parallel to x_2^p (laterally

constrained uniaxial tension/compression or simple shear); and

(c) $\bar{\bar{u}}^{p}_{1,3} = \bar{\bar{\epsilon}}^{p}_{31} = 0$ ($\bar{\bar{\alpha}}^{p}_{31} = 0$), no translation parallel to x^{p}_{1} (laterally constrained uniaxial tension/compression).

The two no-tilt rotational constraints are:

(d) $\bar{\bar{u}}^{p}_{3,2} = \bar{\bar{\epsilon}}^{p}_{23} = 0$ ($\bar{\bar{\alpha}}^{p}_{23} = 0$), no rotation about x^{p}_{1}; and

(e) $\bar{\bar{u}}^{p}_{3,1} = \bar{\bar{\epsilon}}^{p}_{13} = 0$ ($\bar{\bar{\alpha}}^{p}_{13} = 0$), no rotation about x^{p}_{2}.

Operating together, constraints (d) and (e) specify that the plattens remain parallel. Addition of the no-twist condition,

(f) $\bar{\bar{u}}^{p}_{1,2} = \bar{\bar{\epsilon}}^{p}_{21} = \bar{\bar{\epsilon}}^{p}_{12} = \bar{\bar{u}}^{p}_{2,1}$ ($\bar{\bar{\alpha}}^{p}_{12} = \bar{\bar{\alpha}}^{p}_{21}$), demands no rotation about the platten normal, x^{p}_{3}.

Physically, bulk translational constraints result in a constant load creep apparatus acting as a constant strain rate apparatus at a rate equal in magnitude but opposite in sign for each of the constrained, load-induced strain rate components. For each translationally constrained component, a new stress situation is induced by its counteracting strain rate component. The no-tilt constraints impose bulk couples on the specimen, resulting in a superimposed rigid bulk rotation (page 29). The torsional moment arising from the no-twist constraint about x^{p}_{3} yields a non-homogeneous stress situation. As the incorporation of non-homogeneous stress fields is beyond the scope of the present model, no attempt is here made to deal with the satisfaction of the no-twist constraint.

Let the constraint-induced reactive strain rates arising from cases (a) (b) or (c) above be respectively, $\bar{\bar{\epsilon}}^{pa}_{ij}$, $\bar{\bar{\epsilon}}^{pb}_{ij}$ and $\bar{\bar{\epsilon}}^{pc}_{ij}$, with associated reactive octahedral stresses $h_a\tau_o$, $h_b\tau_o$ and $h_c\tau_o$. The respective geometric tensors are then $\bar{\alpha}^{pa}_{ij}$, $\bar{\alpha}^{pb}_{ij}$ and $\bar{\alpha}^{pc}_{ij}$. Clearly at most two of the three possible translational constraints (a) (b) or (c) can be imposed simultaneously, as at least one component must be in the direction of the applied load and therefore unconstrained. Let the index k designate the origin of a particular stress situation, k = 1 indicating the applied stress situation and k = 2 and 3 indicating the constraint induced situations. Let $\sim$ denote a parameter which satisfies the translational constraints. Then

$$\tilde{\alpha}^{p}_{ij} = h_k\, \bar{\alpha}^{pk}_{ij}$$

$$= h_1\, \bar{\alpha}^{p1}_{ij} + h_2\, \bar{\alpha}^{p2}_{ij} + h_3\, \bar{\alpha}^{p3}_{ij} \tag{3.41}$$

where $h_1 = 1$, and summation is implied over k, i.e. over all stress situations applied and induced. It follows that

$$\tilde{g}^{p}_{ij} = h_k\, \bar{g}^{pk}_{ij} \tag{3.42}$$

and

$$\tilde{g}^{p}_{o} = \frac{1}{\sqrt{3}} (\tilde{g}^{p}_{ij}\, \tilde{g}^{p}_{ij})^{1/2} \tag{3.43}$$

It is easily verified that the composite octahedral stress in the aggregate is

$$\tilde{\tau}_o = (h_i h_j\, \delta_{ij})^{1/2}\, \tau_o \tag{3.44}$$

Satisfaction of the no-tilt constraints (d) and (e) may cause a flow-induced bulk rigid rotation. In order to account for this rotation, an antisymmetric term ρ_{ij}^{p}, is added to the geometric tensor $\tilde{\alpha}_{ij}^{p}$, so that their sum

$$\overline{\alpha}^{p}_{ij} = \tilde{\alpha}^{p}_{ij} + \rho^{p}_{ij} \tag{3.45}$$

satisfies all external constraints, translational and rotational. Platten constraints are now applied to equation (3.45) together with the condition that ρ_{ij}^{p} be antisymmetric:

$$\rho^{p}_{ij} + \rho^{p}_{ji} = 0 \tag{3.46}$$

This leads to a set of simultaneous equations which may be solved for the h_k and ρ_{ij}^{p}. To illustrate the general procedure, the two most common creep test configurations, simple shear and uniaxial tension/compression, are treated by example.

(a) Simple shear

Consider first a specimen in simple shear with the plattens constrained to remain equidistant ($\overline{\alpha}^{p}_{33} = 0$) and parallel ($\overline{\alpha}^{p}_{23} = \overline{\alpha}^{p}_{13} = 0$) with no lateral translation ($\overline{\alpha}^{p}_{32} = 0$). The simultaneous constraint equations are:

$$\overline{\alpha}^{p}_{33} = \tilde{g}^{p1}_{33} + h_2\,\tilde{g}^{p2}_{33} + h_3\,\tilde{g}^{p3}_{33} = 0 \tag{3.47a}$$

$$\overline{\alpha}^{p}_{32} = \tilde{\alpha}^{p1}_{32} + h_2\,\tilde{\alpha}^{p2}_{32} + h_3\,\tilde{\alpha}^{p3}_{32} + \rho^{p}_{32} = 0 \tag{3.47b}$$

$$\overline{\alpha}^{p}_{23} = \tilde{\alpha}^{p1}_{23} + h_2\,\tilde{\alpha}^{p2}_{23} + h_3\,\tilde{\alpha}^{p3}_{23} + \rho^{p}_{23} = 0 \tag{3.47c}$$

$$\overline{\alpha}^{p}_{13} = \tilde{\alpha}^{p1}_{13} + h_2\,\tilde{\alpha}^{p2}_{13} + h_3\,\tilde{\alpha}^{p3}_{13} + \rho^{p}_{13} = 0 \tag{3.47d}$$

$$\rho^{p}_{13} + \rho^{p}_{31} = 0 \tag{3.47e}$$

$$\rho^{p}_{23} + \rho^{p}_{32} = 0 \tag{3.47f}$$

Adding equations (3.47b) and (3.47c), elminating ρ^{p}_{23} and ρ^{p}_{32} with equation (3.47f) and noting that

$$\tilde{\alpha}^{pk}_{ij} + \tilde{\alpha}^{pk}_{ji} = 2\tilde{g}^{pk}_{ij} \tag{3.48}$$

we have

$$\tilde{g}^{p1}_{23} + h_2\,\tilde{g}^{p2}_{23} + h_3\,\tilde{g}^{p3}_{23} = 0 \tag{3.49}$$

Solving equations (3.47a) and (3.49) for h_2 and h_3 gives

$$h_2 = (\tilde{g}^{p1}_{23}\,\tilde{g}^{p3}_{33} - \tilde{g}^{p1}_{33}\,\tilde{g}^{p3}_{23})/(\tilde{g}^{p2}_{23}\,\tilde{g}^{p3}_{33} - \tilde{g}^{p2}_{33}\,\tilde{g}^{p3}_{23}) \tag{3.50a}$$

$$h_3 = (\tilde{g}^{p2}_{33}\,\tilde{g}^{p1}_{23} - \tilde{g}^{p1}_{23}\,\tilde{g}^{p2}_{33})/(\tilde{g}^{p2}_{23}\,\tilde{g}^{p3}_{33} - \tilde{g}^{p3}_{23}\,\tilde{g}^{p2}_{33}) \tag{3.50b}$$

With h_2 and h_3 known, the non-vanishing components of ρ_{ij}^{p} are

$$\rho^{p}_{13} = \tilde{\alpha}^{p}_{31} \tag{3.51a}$$

$$\rho^{p}_{31} = \tilde{\alpha}^{p}_{13} \tag{3.51b}$$

$$\rho^{p}_{23} = \tilde{\alpha}^{p}_{32} \tag{3.51c}$$

$$\rho^{p}_{32} = \tilde{\alpha}^{p}_{23} \tag{3.51d}$$

The composite geometric factor for the strain rate component parallel to the applied stress, i.e. the measured component in a simple shear creep test, is

$$\begin{aligned}\overline{\alpha}^{p}_{31} &= \tilde{\alpha}^{p}_{31} + \rho^{p}_{31} \\ &= \tilde{\alpha}^{p}_{31} + \tilde{\alpha}^{p}_{13} \\ &= 2\,\tilde{g}^{p}_{31}\end{aligned} \tag{3.52}$$

(b) Uniaxial compression

As a second example, consider a specimen in uniaxial compression between parallel plattens constrained against lateral translation. The constraint equations are

$$\overline{\alpha}^{p}_{31} = \tilde{\alpha}^{p1}_{31} + h_2\,\tilde{\alpha}^{p2}_{31} + h_3\,\tilde{\alpha}^{p3}_{31} + \rho^{p}_{31} = 0 \tag{3.53a}$$

$$\overline{\alpha}^{p}_{32} = \tilde{\alpha}^{p1}_{32} + h_2\,\tilde{\alpha}^{p2}_{32} + h_3\,\tilde{\alpha}^{p3}_{32} + \rho^{p}_{32} = 0 \tag{3.53b}$$

$$\overline{\alpha}^{p}_{13} = \tilde{\alpha}^{p1}_{13} + h_2\,\tilde{\alpha}^{p2}_{13} + h_3\,\tilde{\alpha}^{p3}_{13} + \rho^{p}_{13} = 0 \tag{3.53c}$$

$$\overline{\alpha}^{p}_{23} = \tilde{\alpha}^{p1}_{23} = h_2\,\tilde{\alpha}^{p2}_{23} + h_3\,\tilde{\alpha}^{p3}_{23} + \rho^{p}_{23} = 0 \tag{3.53d}$$

$$\rho^{p}_{13} + \rho^{p}_{31} = 0 \tag{3.53e}$$

$$\rho^{p}_{23} + \rho^{p}_{32} = 0 \tag{3.53f}$$

Addition of equations (3.53a) and (3.53c) and substitution of equation (3.53e) yields

$$\tilde{g}^{p1}_{13} + h_2\,\tilde{g}^{p2}_{13} + h_3\,\tilde{g}^{p3}_{13} = 0 \tag{3.54a}$$

Similarly, equations (3.53b, d, f) yield

$$\tilde{g}^{p1}_{23} + h_2\,\tilde{g}^{p2}_{23} + h_3\,\tilde{g}^{p3}_{23} = 0 \tag{3.54b}$$

The simultaneous solution of equations (3.54a) and (3.54b) then gives

$$h_2 = (\tilde{g}^{p1}_{23}\,\tilde{g}^{p3}_{13} - \tilde{g}^{p1}_{13}\,\tilde{g}^{p3}_{23})/(\tilde{g}^{p2}_{23}\,\tilde{g}^{p3}_{13} - \tilde{g}^{p3}_{13}\,\tilde{g}^{p2}_{23}) \tag{3.55a}$$

$$h_3 = (\tilde{g}^{p1}_{13}\,\tilde{g}^{p2}_{23} - \tilde{g}^{p1}_{23}\,\tilde{g}^{p2}_{13})/(\tilde{g}^{p3}_{23}\,\tilde{g}^{p2}_{13} - \tilde{g}^{p2}_{13}\,\tilde{g}^{p3}_{23}) \tag{3.55b}$$

Returning to constraint equations (3.53) with h_2 and h_3, the non-vanishing components of ρ^{p}_{ij} become

$$\rho^{p}_{13} = \tilde{\alpha}_{31} \tag{3.56a}$$

$$\rho^{p}_{31} = \tilde{\alpha}_{13} \tag{3.56b}$$

$$\rho^{p}_{23} = \tilde{\alpha}_{32} \tag{3.56c}$$

$$\rho^{p}_{32} = \tilde{\alpha}_{23} \tag{3.56d}$$

Finally, the axial geometric factor is

$$\bar{\alpha}^{p}_{33} = \tilde{\alpha}^{p}_{33} = \tilde{g}^{p}_{33} \tag{3.57}$$

3.2.4 The incorporation of internal flow constraints — intergranular interaction

Rotational and deformational interaction between grains is now considered, once again in terms of bulk integrals. Three assumptions are made: first, that on the average the interference between a particular grain and its immediate neighbours is equivalent to the hypothetical interference between that grain and the bulk material; second, that the interference rate between that grain and the bulk material is measured by an interference rate tensor, i.e. the difference between the strain rate tensor of that grain and that of the bulk material; and third, that the degree of interference for the aggregate as a whole is proportional to the volumetric mean second deviator of the interference rate tensors, i.e. to the r.m.s. octahedral interference rate.

The requirement (Taylor 1956) that each grain conform to the bulk state of flow leads to a physical interpretation of the r.m.s. octahedral interference rate. The bulk octahedral interference rate is the sum of a bulk rotational rate of interference (derived from the antisymmetric, or rotational, part of the interference rate tensor) and a bulk deformational rate of interference (derived from the symmetric, or deformational, part of the tensor). We may associate its rotational contribution with the bulk rate of intergranular accommodation sliding at grain boundaries, and its deformation contribution with the bulk rate at which additional creep mechanisms (Shumskiy 1958, Voitkovskii 1960, Gold 1963, Langdon 1973, and Steinemann 1958a) must act to provide the necessary degree of deformational accommodation.

The rate of interference between an individual grain and the aggregate as a whole is

$$\dot{d}_{ij} = \dot{\epsilon}_{ij} - \tilde{\dot{\epsilon}}_{ij} \tag{3.58}$$

It follows that the square of its octahedral rate of interference is

$$\begin{aligned} \dot{d}^{2}_{o} &= \tfrac{1}{3}\, \dot{d}_{ij}\, \dot{d}_{ij} \\ &= \tfrac{1}{3}\, \dot{\epsilon}_{ij}\, \dot{\epsilon}_{ij} - \tfrac{2}{3}\, \tilde{\dot{\epsilon}}_{ij}\, \dot{\epsilon}_{ij} + \tfrac{1}{3}\, \tilde{\dot{\epsilon}}_{ij}\, \tilde{\dot{\epsilon}}_{ij} \end{aligned} \tag{3.59}$$

The mean square octahedral interference rate for the aggregate is therefore

$$\bar{\dot{d}}^{2}_{o} = \frac{1}{V} \int_{V} \dot{d}^{2}_{o}\, dV$$

$$= \frac{1}{3V} \int_V \dot{\epsilon}_{ij}\,\dot{\epsilon}_{ij}\,dV - \frac{2}{3V}\tilde{\dot{\epsilon}}_{ij} \int_V \dot{\epsilon}_{ij}\,dV + \tfrac{1}{3}\tilde{\dot{\epsilon}}_{ij}\,\tilde{\dot{\epsilon}}_{ij}$$

$$= \tfrac{1}{3} \int_{2\pi} \int \dot{\epsilon}_{ij}\,\dot{\epsilon}_{ij}\,d\Omega - \tfrac{1}{3}\tilde{\dot{\epsilon}}_{ij}\,\tilde{\dot{\epsilon}}_{ij}$$

$$= \lambda_B^2\,\tilde{\tau}_o^2 \int_{2\pi} \int \frac{\alpha_{ij}\alpha_{ij}}{3}\,d\Omega - \lambda_B^2\,\tilde{\tau}_o^2\,\frac{\tilde{\alpha}_{ij}\tilde{\alpha}_{ij}}{3}$$

$$= \lambda_B^2\,\tilde{\tau}_o^2 \int_{2\pi} \int \alpha_o^2\,d\Omega - \lambda_B^2\,\tilde{\tau}_o^2\,\tilde{\alpha}_o^2 \tag{3.60}$$

where appropriate substitutions have been made using equations (2.69) and (3.33). Let the mean square octahedral geometric factor be

$$\widetilde{\alpha_o^2} = \int_{2\pi} \int \alpha_o^2\,d\Omega = \int_{2\pi} \int \alpha^2\,d\Omega \tag{3.61}$$

Incorporating equation (3.61), expression (3.60) may then be written

$$\tilde{d}_o^2 = \lambda_B^2\,\tilde{\tau}_o^2\,\widetilde{\alpha_o^2} - \lambda_B^2\,\tilde{\tau}_o^2\,\tilde{\alpha}_o^2$$

$$= \lambda_B^2\,\tilde{\tau}_o^2\,(\widetilde{\alpha_o^2} - \tilde{\alpha}_o^2) \tag{3.62}$$

yielding the r.m.s. octahedral interference rate:

$$\tilde{\dot{d}}_{rms} = (\tilde{\dot{d}}_o^2)' = \lambda_B\,\tilde{\tau}_o(\tilde{\alpha}_o^2 - \tilde{\alpha}_o^2)' \tag{3.63}$$

The effect of intergranular interference on the bulk strain rate is realised as an increase in the specific rate of dissipation arising from the bulk r.m.s. octahedral interference rate operating against the mean boundary stress. Assuming that the mean boundary stress is of the order of the mean octahedral shear stress τ_o, the specific rate of energy dissipation due to interference is approximately

$$\bar{q} = \tilde{\dot{d}}_{rms}\,\tilde{\tau}_o = \lambda_B\,\tilde{\tau}_o^2(\tilde{\alpha}_o^2 - \tilde{\alpha}_o^2)' \tag{3.64}$$

This additional specific rate of dissipation has been related by Batchelor (1970, his equation 4.11.16.) to an increase in the effective bulk viscosity.
Then, following Batchelor,

$$\bar{q} = 6(\lambda_o' - \lambda_{oN}')\,\tilde{\dot{\gamma}}_{oN}^2 \tag{3.65}$$

where $\tilde{\dot{\gamma}}_{oN}$ is the ambient deformation rate of the substance (in the present case, that of the non-interacting aggregate); λ_{oN} (equation (3.39)) is its ambient fluidity. The increase in viscosity is $\lambda_o' - \lambda_{oN}'$, λ_o being the effective bulk fluidity of the substance with interference effects included. Eliminating $\bar{q}$ between equations (3.64) and (3.65) and replacing the deformation rate tensor in terms of the geometric tensor using equations (3.37) and (3.39), the effective fluidity of the specimen due to the effects of crystallographic anisotrophy becomes

$$\lambda_o = \lambda_B \tilde{g}_o \left[1 + \left(\frac{\tilde{\alpha}_o^2 - \bar{\alpha}_o^2}{36\tilde{g}_o^2} \right)^{1/2} \right]^{-1} \tag{3.66}$$

It follows by equation (3.12) that the required interference factor is

$$\tilde{\beta} = \left[1 + \left(\frac{\tilde{\alpha}_o^2 - \bar{\alpha}_o^2}{36\tilde{g}_o} \right)^{1/2} \right]^{-1} \tag{3.67}$$

When interference effects are excluded by setting $\tilde{q} = 0$, the implication of equation (3.64) is that $\tilde{\alpha}_o^2 = \bar{\alpha}_o^2$. Then $\beta = 1$ and $\tilde{\alpha}_o = [\alpha_o^2]^{1/2}$. By equations (3.61) and (3.35) it follows that

$$\dot{\tilde{\epsilon}}_{oN} \propto \left[\int_{2\pi} f \alpha^2 \, d\Omega \right]^{1/2} \tau_o. \tag{3.68}$$

As β is independent of stress, equations (3.68) and (3.4) yield

$$\dot{\tilde{\epsilon}}_o \propto \tau_{rms}. \tag{3.69}$$

Thus the assumptions of the present model lead to the conclusion that $\dot{\tilde{\epsilon}}_o$ is proportional to the r.m.s.-resolved basal shear stress (cf. Section 3.2).

3.3 THE ENHANCEMENTS

The octahedral enhancement factor given by equation (3.13) may be written

$$E = B(f,\Lambda)\, G(f,\Lambda) \tag{3.70}$$

where

$$B(f,\Lambda) = \tilde{\beta}(f,\Lambda)/\tilde{\beta}(f') \tag{3.71}$$

is the interference component of the enhancement, and

$$G(f,\Lambda) = \tilde{g}_o(f,\Lambda)/\tilde{g}_o(f') \tag{3.72}$$

is the geometric component of the enhancement. In order to evaluate equations (3.71) and (3.72) the isotropic geometric tensor $\tilde{\alpha}_{ij}(f')$ must first be found by the analytical integration of equations (3.28) and (3.29). When equations (3.28), (3.29) and (3.5) are substituted into equation (3.34), the result, by symmetry, is

$$\tilde{w}_{ij}(f') = 0 \tag{3.73}$$

and

$$\tilde{g}_{ij}(f') = 0 \text{ for } i \neq j. \tag{3.74}$$

Thus only the components $\tilde{g}_{11}$, $\tilde{g}_{22}$ and $\tilde{g}_{33}$ require detailed treatment. In particular

$$\tilde{g}_{11'} = \frac{3(\Lambda^2 + 3)^{-1/2}}{2\sqrt{2}\,\pi} \int_0^{2\pi} \int_0^{\pi/2} \sin^3\theta \cos^2\alpha [(\Lambda + 1)\sin^2\theta \sin^2\alpha + 2\cos^2\theta] \, d\theta \, d\alpha$$

$$= \frac{1}{5\sqrt{2}} \frac{(\Lambda + 3)}{(\Lambda^2 + 3)^{1/2}} \tag{3.75}$$

$$\tilde{g}_{22} = \frac{-3(\Lambda^2 + 3)^{-1/2}}{2\sqrt{2}\,\pi} \int_0^{2\pi} \int_0^{\pi/2} \sin^3\theta \sin^2\alpha[(\Lambda + 1)\sin^2\theta \cos^2\alpha + (\Lambda - 1)\cos^2\theta]\, d\theta\, d\alpha$$

$$= \frac{-1}{5\sqrt{2}} \frac{2\Lambda}{(\Lambda^2 + 3)^{1/2}} \tag{3.76}$$

$$\tilde{g}_{33} = \frac{3(\Lambda^2 + 3)^{-1/2}}{2\sqrt{2}\,\pi} \int_0^{2\pi} \int_0^{\pi/2} \sin\theta \cos^2\theta[(\Lambda - 1)\sin^2\theta \sin^2\alpha - 2\sin^2\theta \cos^2\alpha]\, d\theta\, d\alpha$$

$$= \frac{1}{5\sqrt{2}} \frac{(\Lambda - 3)}{(\Lambda + 3)^{1/2}} \tag{3.77}$$

Written in full the geometric tensor is

$$\tilde{\alpha}_{ij}(f') = \tilde{g}_{ij}(f') = \frac{1}{5\sqrt{2}} \begin{vmatrix} \dfrac{\Lambda + 3}{(\Lambda^2 + 3)^{1/2}} & 0 & 0 \\ 0 & \dfrac{-2\Lambda}{(\Lambda^2 + 3)^{1/2}} & 0 \\ 0 & 0 & \dfrac{\Lambda - 3}{(\Lambda^2 + 3)^{1/2}} \end{vmatrix} \tag{3.78}$$

A comparison of equations (3.78) and (2.27) shows that the components of the geometric tensor are proportional to those of the stress deviator. The state of flow must therefore be isotropic and thus satisfy translational flow (platten) constraints identically:

$$\tilde{\alpha}_{ij}(f') = \tilde{g}_{ij}(f') = \tilde{\alpha}_{ij}(f') = \tilde{g}_{ij}(f') \tag{3.79}$$

The octahedral geometric factor becomes

$$\tilde{\alpha}_o(f') = \tilde{g}_o = \tilde{\alpha}_o(f') = \tilde{g}_o(f')$$

$$= \frac{1}{5\sqrt{2}} (\Lambda^2 + 3)^{-1/2}[(\Lambda + 3)^2 + 4\Lambda^2 + (\Lambda - 3)^2]^{1/2}$$

$$= \frac{1}{5}\,. \tag{3.80}$$

Indroducing the result given by the above equation into equation (3.67) which defines β and using equations (3.61) and (3.6) for α_o^2, we have

$$\beta(f') = \tilde{\beta}(f') = \frac{3}{4} \tag{3.81}$$

so that

$$B(f, \Lambda) = \frac{4}{3}\,\tilde{\beta}(f, \Lambda). \tag{3.82}$$

Similarly, the octahedral geometric enhancement becomes

$$G(f, \Lambda) = 5\,\bar{g}_o\,(f, \Lambda). \tag{3.83}$$

Finally, the octahedral enhancement is obtained by substitution of equations (3.82) and (3.83) into (3.70):

$$E = \frac{20}{3}\,\tilde{\beta}(f, \Lambda)\,\bar{g}_o\,(f, \Lambda) \tag{3.84}$$

The octahedral shear stress acting in the aggregate is given by equation (3.44). This stress is enhanced over that of the applied load by a factor

$$E_\tau = \frac{\bar{\tau}_o}{\tau_o} = (h_i h_j\,\delta_{ij})^{1/2} \tag{3.85}$$

The typical creep set-up yields only that strain rate component associated with the direction of the applied load. For an anisotropic aggregate, the octahedral deformation rate and strain rate cannot be evaluated from one measured component of $\bar{\dot{\epsilon}}_{ij}$ without a priori assumptions concerning the state of flow. Thus, if the model is to be tested conveniently or applied generally to past single component anisotropic creep results, a definition of component enhancement is needed. This task is simplified if platten co-ordinates are used. Let the component enhancement be defined as the ratio of the component strain rates, i.e.

$$\begin{aligned} E^p_{ij} &= \frac{\bar{\dot{\epsilon}}^p_{ij}\,(f, \Lambda)}{\bar{\dot{\epsilon}}^p_{ij}(f')} \\ &= \frac{\beta(f, \Lambda)}{\beta(f')}\,\frac{\bar{\alpha}^p_{ij}\,(f, \Lambda)}{\bar{\alpha}^p_{ij}\,(f')} \end{aligned} \tag{3.86}$$

Here summation on i and j is not implied.

Consider first the case of simple shear (page 44); we require E^p_{31}. By equation (3.52)

$$E^p_{31} = \frac{\beta(f)\;\tilde{g}^p_{31}(f)}{\beta(f')\;\tilde{g}^p_{31}(f')} \tag{3.87}$$

The geometric tensor component $\tilde{g}^p_{31}(f') = \bar{g}^p_{31}(f')$ is obtained from equation (3.78) by the co-ordinate transformation (cf. equation (3.40))

$$\tilde{g}^p_{31}(f') = p_{i3}p_{j1}\,\bar{g}_{ij}(f') \tag{3.88}$$

where (cf. page 21, with $\sigma = 0$)

$$P_{lm} = \frac{1}{\sqrt{2}}\begin{vmatrix} 1 & 1 & 1 \\ 0 & \sqrt{2} & 0 \\ -1 & 0 & 1 \end{vmatrix}. \tag{3.89}$$

Expanding equation (3.88) with $\Lambda = 0$,

$$\tilde{g}^{p}_{31}(f') = \tfrac{1}{2}\,[\tilde{g}_{11}(f') - \tilde{g}_{33}(f')]$$

$$= \frac{\sqrt{3}}{5\sqrt{2}}\,. \tag{3.90}$$

Equations (3.87), (3.81) and (3.90) are then combined to obtain

$$E^{p}_{31}(f) = \frac{20\sqrt{2}}{3\sqrt{3}}\,\beta\,(f)\,\tilde{g}^{p}_{31}(f). \tag{3.91}$$

For uniaxial compression the principal and platten axes coincide (page 45), so we have directly from equations (3.78) and (3.79)

$$E^{p}_{33}(f) = \frac{\beta(f)}{\beta(f')}\,\frac{\tilde{g}^{p}_{33}(f)}{\tilde{g}_{33}(f')}. \tag{3.92}$$

For $\Lambda = -1$ (uniaxial compression), equation (3.92) becomes

$$E^{p}_{33}(f) = \frac{20}{3\sqrt{2}}\,\beta(f)\,\tilde{g}^{p}_{33}(f) \tag{3.93}$$

The octahedral enhancement factor (equation (3.84)) and the component enhancement factors (equations (3.91) and (3.93)) must be evaluated numerically for a given orientation fabric. The bulk geometric tensor $\tilde{\alpha}_{ij}$ is first evaluated numerically in principal stress co-ordinates using equation (3.34). Equation (3.88) is then used to obtain the geometric tensor $\tilde{\alpha}^{p}_{ij}$ in platten co-ordinates. If $\tilde{\alpha}^{p}_{ij}$ satisfies all platten constraints identically, the interference factor β and the component and octahedral enhancement E^{p}_{ij} and E^{p} may be found directly. If not, the geometric factors for the induced stress situations must be determined and the constraint equations given in Section 3.2.3. solved to obtain $\bar{\tilde{\alpha}}^{p}_{ij}$ so that the results of the present section may be used to find the relevant enhancement.

3.4 IMPLICATIONS OF THE MODEL

A flexible numerical computer program has been written which requires as input an orientation density f and its orientation with respect to the platten co-ordinates, the normal and shear stresses applied to the plattens and the platten constraints of the creep apparatus. An apparatus similar to that described on page 20 is assumed. The program provides as output the interference factor, bulk geometric and component enhancements as well as the net octahedral enhancement. The bulk state of stress is output in terms of the aggregate stress enhancement and configuration parameter.

Using this program, the model has been applied to a spherical normal distribution of axes (Fisher 1953, McElhinny 1967, and Barton 1974) for various standard deviations assuming an 'easy glide' situation in simple shear. This case was selected

as one for which the greatest enhancements might be expected, thereby providing an extreme situation to test the model. The results of this test for standard deviations (σ_θ) ranging up to 35° are shown in Figure 7. For a relatively strong single pole ($\sigma_\theta < 9°$) in easy glide, shear enhancements in excess of 3 are predicted by the model. As the standard deviation becomes large, the fabric becomes isotropic and the enhancements approach unity. Due to the symmetry of the fabric with respect to the plane of maximum shear stress, platten constraints are satisfied identically, so that the aggregate octahedral stress and configuration parameter are those of the applied load.

As a second test aimed at investigating the results for a fabric not in conformity with the applied load or bulk state of flow (Budd 1972), a spherical normal fabric was once again used. This time the axis of the pole was tilted at an angle $0 \leq \theta_f \leq 45$ degrees from the easy glide orientation into the direction of shear. Model-derived estimates of the shear and stress enhancement factors and aggregate stress

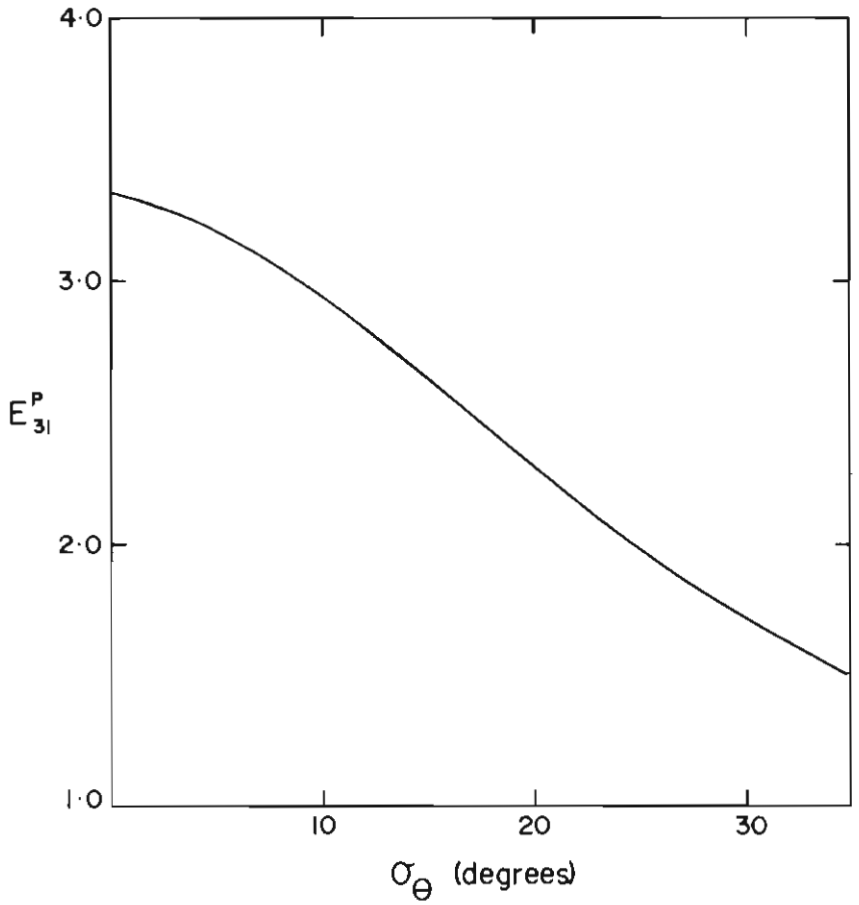

Figure 7. Model-derived shear component enhancement in easy glide for a single pole spherical normal fabric versus the standard deviation σ_θ of the fabric.

configuration parameter are shown in Figure 8. At θ_f equal to zero and 45° the fabric is symmetric with respect to the applied stress. Figure 8 confirms that the plattens constraints are then satisfied identically, and the octahedral shear stress and stress configuration are those of the applied load (E_r = 1 and Λ = 0). Of particular note is the modified state of stress for a tilt orientation of approximately 11° (Figure 8). Here the aggregate tends to contract in a direction normal to the plattens. This contraction induces a tensile stress at the plattens, which are constrained to remain equidistant (cf. Glen's (1958) discussion on his page 177). The effect of this superimposed tensile state of stress is to increase the octahedral shear stress in the aggregate by a factor (E_r) of approximately 1.8 and to alter the stress configuration parameter to a value of nearly 0.8, i.e. inducing an enhanced state of stress more nearly uniaxial tensile (Λ = 1) than the applied two dimensional state (Λ = 0).

If the model results given in Figure 8 are realistic, it is clear that laboratory creep results for anisotropic ice must be interpreted in light of possible gross alterations to the state of stress as calculated in the usual manner. Furthermore, if such tests

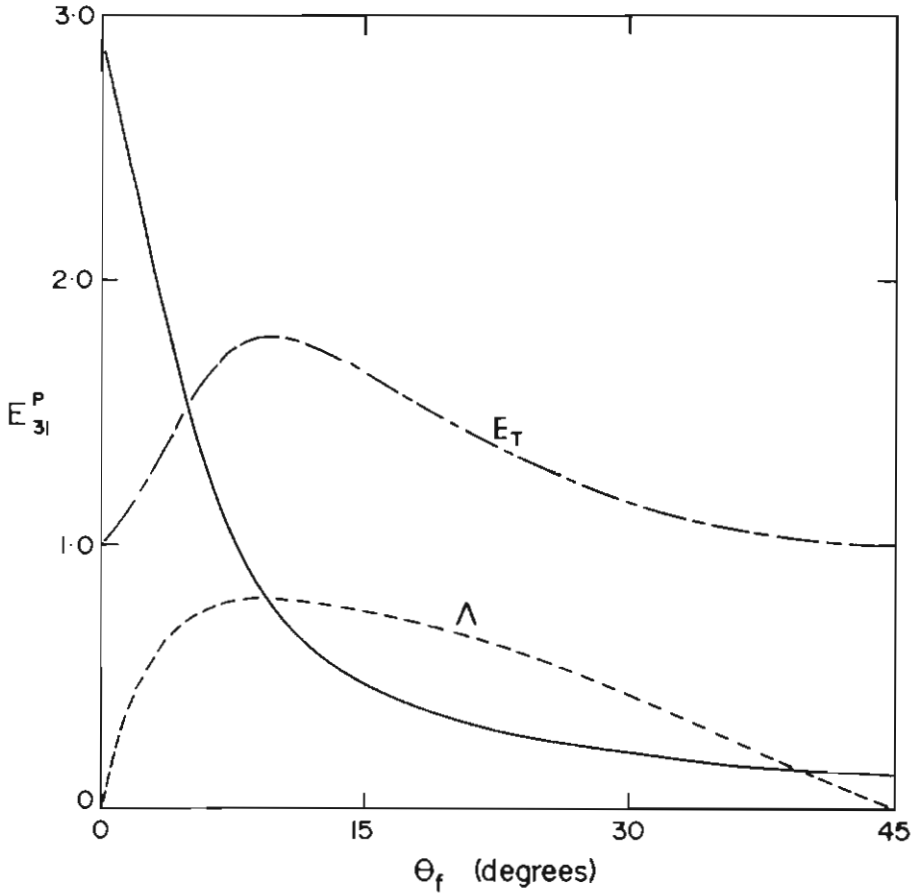

Figure 8. Calculated shear enhancement, stress enhancement and aggregate stress configuration parameter for a single pole spherical normal fabric (standard deviation σ_θ = 10°) for various angles of tilt θ_f into the direction of shear.

are meant to simulate *in situ* field conditions, particular care must be taken to ensure the accurate orientation of the fabric with respect to the applied state of stress. The component enhancement and state of stress are most sensitive to misalignment at small deviations from the *in situ* conditions as indicated by the steep slopes of E^e_{31} and Λ at $\theta_f = 0$ (Figure 8).

The present model is based on the assumption that there are sufficient grains in the aggregate to describe the aggregate in terms of its bulk properties. In particular, the state of stress and state of flow are assumed to be homogeneous. It is recognised that the state of stress on the granular scale is not homogeneous — that well aligned crystals appear to be 'soft sites' where the local level of stress is diminished, and poorly aligned crystals appear as 'hard sites' of enhanced local stress. Weertman (1963) argued qualitatively that this redistribution of stress on the granular scale is primarily responsible for determining the magnitude of the interference factor (β). The task of determining the redistribution of stress quantitatively at this scale is certainly impractical if not impossible.

As these small-scale variations do not effect the aggregate state of stress, stress homogeneity was assumed in Section 3.2.4. and interference was treated in terms of the specific rate of dissipation necessary to guarantee homogeneity in the state of flow. This approach led to an expression for the interference factor in terms of invariants of the bulk geometric tensor. On the other hand, when external flow constraints are considered, the enhanced state of stress implied by the model has implications to the development of preferred orientation fabrics in natural ice masses. Picturing a natural ice mass as a collection of individual volume elements migrating through a statistically static (from the Eulerian point of view) parent body of ice, each element incurs a slowly changing state of stress. The characteristic size of a volume element is dependent on the magnitude of the gradients of stress configuration and reorientation of the principal axes of stress. Neighbouring volume elements exert external flow constraints; as a result slight asymmetries of the orientation fabric induce enhanced levels of stress which hasten dynamic recrystallisation. Taken together with induced rotations, the enhanced rate of recrystallisation evidently provides a positive feedback mechanism sufficient for the crystallographic orientation fabric to remain compatible with the varying states of stress and flow. It follows that a natural ice mass will tend to remain in an enhanced state of flow. If so, there is clearly an urgent need to incorporate an anisotropic flow law such as that proposed here into present ice dynamics models.

The implications discussed above assume the validity of the model, at least at small values of octahedral shear stress. As the model yields estimates of the enhanced rate of strain (through E^e_{ij}) and the enhanced octahedral shear stress (through E_τ), two means of testing the model are possible. Glen (1958) suggested experiments designed to measure modifications in the state of stress. This would involve the measurement of at least one 'cross component' of stress, i.e. a component normal to the applied stress. As an appropriate creep apparatus must be 'cross' constrained for the development of a cross component of stress, a rather sophisticated creep device is implied. The alternative used here is to observe the enhanced value of the creep rate component parallel to the applied load. This has been done for two stress configurations, simple shear and uniaxial compression, and for several orientation fabrics. The results of these creep tests, reported in Section 5, point to the validity of the present model at small octahedral shear stresses.

4. The experimental method

4.1 CONTROL AND MEASUREMENT OF STRESS

The creep experiments presented here are all of the constant load type. The means used to apply loads to the samples are set out in Section 4.4. On page 20 formulas for calculating the octahedral shear stress from known applied loads are presented. The actual magnitudes of the loads in the simple shear tests were indicated by accurate spring balances measuring the tensile stress in the load cables. Alternatively, the known load mass and mechanical advantage of the compact frames were used to calculate the applied loads. Several tests were conducted to confirm these values.

The compressive loads of the uniaxial tests were measured directly using a special compressive spring balance calibrated against standard masses. Control of the loads in all tests was assumed since the resulting strain rates were sufficiently small that the cross-sectional area of the specimens remained constant for all practical purposes.

4.2 MEASUREMENT OF STRAIN RATE

The complete specification of the flow situation for the simplest case of incompressible, irrotational strain requires the measurement of five strain rate components (cf. equation 2.49). In the field it is seldom necessary or practical to measure five independent components, as certain features regarding flow symmetry are often sufficient to establish the orientation of the principle deformation axes (Budd, 1968, 1970a).

In the laboratory, on the other hand, the orientation of the principle axes are precisely determined by the platten constraints of the creep apparatus. Therefore the required number of independent measurements is reduced to two. For the special cases of isotropic pure shear in two dimensions, simple shear and uniaxial tension/compression, an additional relationship between the principle rates of strain (page 29) reduces the requirement to a single measurement.

4.2.1. Microdisplacement transducers

A wide range of devices are available for the measurement of displacements on the order of a few microns and less. Mechanical devices such as drum and dial micrometers are limited to a resolution of about two microns, though levers can be arranged to extend their resolution by a factor of two or three. The primary disadvantage of drum micrometers is the necessity of physical access for each measurement; visual access is sufficient for dial micrometers.

In an excellent review article by Sydenham (1972), a variety of remote reading microdisplacement transducers were compared and a comprehensive bibliography and

list of manufacturers appended. Remote reading distortion strain gauges used in conjunction with a bridge circuit have proven to be both sensitive and reliable in experiments on the creep of metals and geological materials. However the loads involved in the creep testing of ice are extremely small by comparison. As the distortion strain gauge exerts a varying load proportional to displacement, its utility in the constant load tests considered here is limited.

Two types of reactive microdisplacement trasducers (capacitive and inductive) offer infinite resolution, high sensitivity and excellent long-term stability. The Super Linear Variable Capacitor (SLVC) transducer is capable of a total linearity and accuracy of about 1 in 10^5 (Wolfendale, 1968); while the Linear Variable Differential Transformers (LVDT) operated over a limited range can attain a comparible accuracy (Herceg 1972).

4.2.2. Direct current linear variable diferential transformer

The SLVC and LVDT transducers require external AC excitation sources and demodulators. Linearity and sensitivity are very sensitive to source stability and to proper quadrature null of the transducer and connecting cables. This problem has been eliminated with the introduction of the Direct Current LVDT (DCDT). With only a slight increase in transducer size, an oscillator and demodulator have been packaged with the LVDT, thereby eliminating the need for a signal source, demodulator and calibration or adjustments by the user.

A 2 mm full-scale displacement unit (Schaevitz model 050 DCB), exhibiting a scale factor of 200 volts $inch^{-1}$ (7.9 volts mm^{-1}) at an uncalibrated full-scale linearity of 0.0025, is available as a standard product. Over a restricted range of 0.1 mm, its calibrated linearity is better than one part in 10^4. The long-term stability of the 050 DCB at constant temperature was tested in association with uniaxial compression creep apparatus (Section 4.4.1) and the data logger (Section 4.7). Overall system stability for a period exceeding 1700 hours proved to be less than 200 nm after correction for minor ($\pm$ 0.2 °C) temperature fluctuations. The length of the control sample was 150 mm, from which we obtain a strain stability of 1.3 in 10^6 and an overall octahedral deformation rate error less than $1.5 \times 10^{-13} s^{-1}$.

4.3 CONTROL AND MEASUREMENT OF TEMPERATURE

Several domestic deep freezers were used in the present study to obtain temperatures between -5 °C and -15 °C. In addition, two Werner cold boxes capable of continuous operation at -70 °C were used for tests below -15 °C. The thermostats of the domestic units were replaced by sensitive, rapid-response mercury-in-glass contact thermometers. The air in the freezer compartments was circulated with tangential fans to increase the thermal coupling betwen the air and walls of the box and to destroy temperature gradients. The heat output of the fan motors together with the faster thermostats reduced both the peak-to-peak variation and maximum rate of variation in the compartments.

The low temperature Werner boxes were also modified by placing the thermostats in close contact with the cooling coils. The resulting time-temperature variation then

showed characteristics similar to that of the domestic units. In both cases, the cycle time of the units decreased to between five and ten minutes with a corresponding decrease in sensitivity to ambient room temperature. Before modification, the loosely coupled, high hysteresis thermostats resulted in cycle times on the order of an hour or more. Thus, as the ambient room temperature increased, the rate of temperature rise in the compartments increased while the rate of fall decreased. This altered the temperature-time relationship to the extent that a 5 °C change in mean room ambient temperature was reflected as a change in mean compartment temperature of between 0.5 and 1 °C, depending on the particular unit. Peak-to-peak fluctuations were correspondingly large. Following alteration, the maximum peak-to-peak variation dropped to about 3 °C and the maximum sensitivity to room ambient temperature to about 0.05 °C/°C.

In order to further decrease the variation of specimen temperature, a specimen chamber fabricated of 13 mm polystyrene was placed in each freezer compartment. Each chamber had an integral temperature control system. The freezer compartment of each unit was regulated to approximately 5 °C below the target temperature required in the specimen chamber. Air within the specimen chamber was continually recirculated through a heat exchanger coupled to the freezer compartment. Before entering the exchanger from the specimen chamber, the recirculating air passed across a heating element. Passing next through a tangential fan, the turbulent airstream was efficiently coupled to the cooling fins of the exchanger before flowing past a thermistor sensor and returning to the chamber. With current to the heating element regulated by the thermistor, the air stream re-entering the chamber was maintained at the target temperature to within ± 0.01 °C. The entire volume of air in the chamber was recirculated in this way every few seconds.

Additional passive regulation, provided by the thermal inertia of the creep frame, kerosine bath, and specimens reduced the short-term rate of change to less than one millidegree per hour.

There are two primary considerations in the measurement of temperature associated with creep tests. The first is the accuracy to which the absolute temperature must be known; the second is the resolution to which temperature variations must be detected. It is now well known that the creep of ice is a thermally activated process. Evidently specification of the temperature to ± 0.1 °C is sufficient except within about 5 °C of pressure melting where the flow dependence on temperature increases due to a change in activation energy.

Most of the creep tests described in the present text were conducted in sealed secondary chambers in order to attain a relatively precise limitation to temperature variations. With visual and mechanical access unavailable for the duration of the tests, the necessity for remote reading electrical thermometers becomes apparent. A quartz thermometer with an absolute accuracy of ± 0.01 °C and a resolution of 0.0001 °C was available as a secondary standard, against which several instruments, used on a routine basis, were calibrated. On occasions the quartz thermometer also served for routine measurements, providing an opportunity to confirm the characteristics of those sensors designed and built expressly for the present tests.

Several levels of temperature monitoring were available. The temperature within the coldboxes external to the sample chamber was displayed continuously by visual dial-type liquid expansion thermometers to ± 0.5 °C. On the low temperature boxes,

these thermometers also activated over-temperature audible alarms. At the next level, the thermistor-controlled heating units of the sample chambers included visual indicators in parallel with the heating elements. Proper control of air temperature in the sample chamber was indicated by normal cyclic variation of these indicators. Within the sample chamber, one or more National Semiconductor LX5600 temperature transducers monitored temperature in the kerosine baths and reservoirs. Calibrated against the quartz thermometer, the transducers were accurate to better than 0.05 °C.

4.4 THE CREEP FRAMES

4.4.1 Uniaxial compression tests

Compression tests were carried out in several sturdy cast aluminium frames as illustrated in Figure 9. Near one end of the frame, a reservoir measuring 200 mm x 75 mm x 179 mm deep provided sufficient room for five cylindrical specimens arranged vertically in a single row. To the ends of each specimen were frozen brass plattens. A conical seat, lapped to receive a spherical platten bearing 7.8 mm in diameter, was centred on the outer face of each circular platten. The lower platten bearings were fixed in five equally spaced conical depressions in the bottom of the casting reservoir.

The displacement transducers were rigidly mounted in a single aluminium block bolted under the front lip of the reservoir. The rear lip of the reservoir, supported by three solid ribs, extended 220 mm beyond the rear reservoir wall, providing a mechanically stable fulcrum for the measurement arms. Near the rear edge, a set of seats were machined to receive a lateral pair of pin fulcrums for each of the five measurement arms. Each 'T' shaped measurement arm extended forward, directly over its associated specimen and displacement transducer (Figure 9). The third support point for each arm was the upper platten bearing of its specimen.

At the forward extremity of each arm, the transducer core was attached by a short length of phosphor-bronze wire to ensure alignment of the core in the teflon bushing of the transducer body. Provision for coarse alignment of the core was offered by a 'potlock' attaching the forward section of the arm to the main 9.25 mm diameter tubular section. The axial specimen displacement was thereby transferred to the transducer core with a multiplication factor (or 'arm factor') of approximately 1.35.

Two methods of applying axial loads to the sample were used: one for octahedral stresses between 0.05 and 0.5 bar; a second for stresses between 0.28 and 2.8 bars. In the former case, the load was transferred to the specimen through the measurement arm by application directly over the specimen. To the load arms, pivoted near the front lip of the reservoir, were attached weights. This load was transferred to the sample with a variable mechanical advantage as high as five. This considerably reduced the actual mass necessary to attain a given octahedral shear stress.

In the latter case, the loads were considered too great to be applied to the measurement arms due to the possibility of causing flexure. The load arm pivots were therefore placed in the reservoir, fastened to the rear wall at a height just above the upper plattens. The upper platten bearing was fixed to the load arm in such a manner

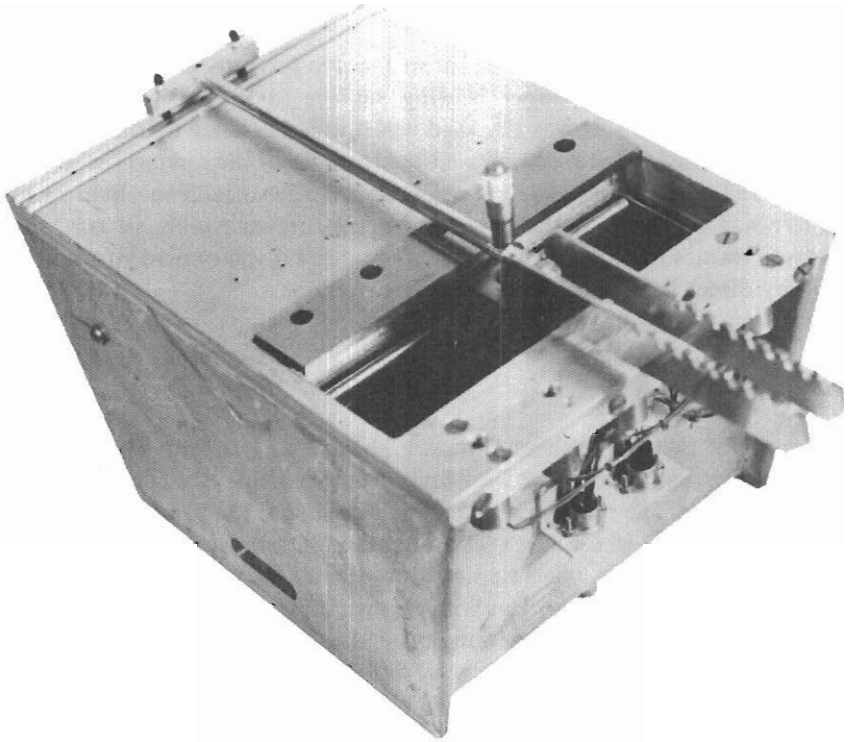

Figure 9. An example of the sturdy cast aluminium frames used for the uniaxial compression tests.

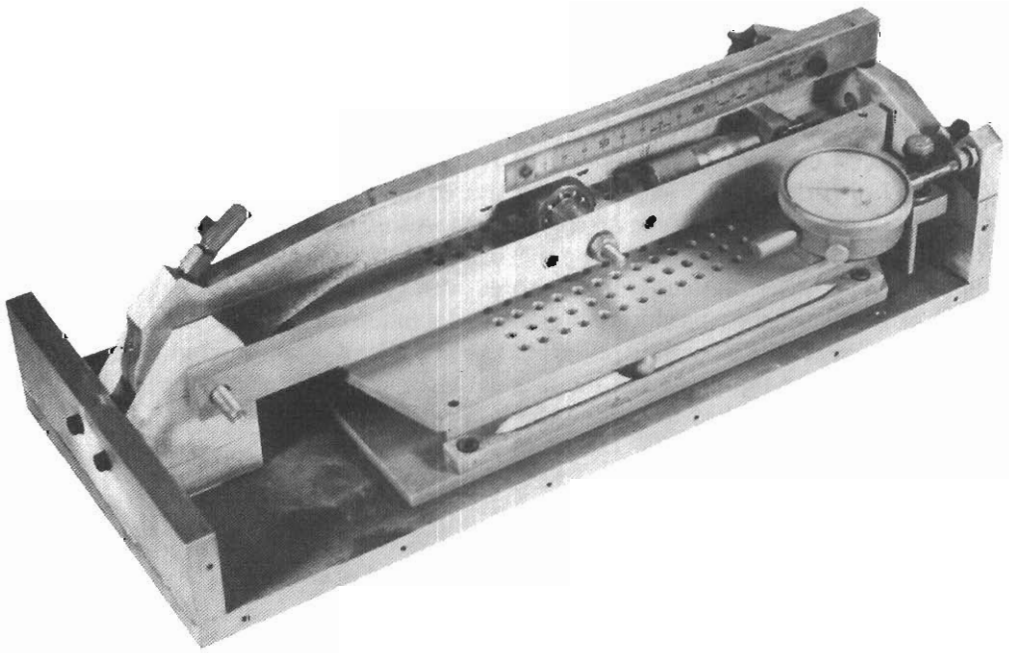

Figure 10. An example of the compact frames used in the simple shear tests.

to be sufficiently proud of the load arm surfaces to properly engage the upper platten seat while presenting the upper bearing surface to the forward support of the measurement arm. In this way the load was applied directly by the load arm to the upper platten. The load arm passed over the front lip of the reservoir where calibrated weights were supported on hangers. An incrementally variable mechanical advantage up to five was available. In the low stress frames the measurement arms, and in the high stress frames the load arms, prevented lateral displacement of the top of each sample by direct fixture to the platten bearings.

4.4.2 Simple shear tests

An example of the simple shear frames is shown in Figure 10. Two 6.35 mm thick aluminium plattens were fitted with linear steel 'V'-block bearing races parallel to their lateral sides. The races were machined parallel to the platten faces so that 12.7 mm ball bearings set in the races separated the plattens by 25.4 mm. Two different methods, described later, were employed to restrict separation of the plattens under load. The races also acted to disallow relative lateral displacement of the plattens while leaving them free to shear longitudinally, one over the other.

To the centre of the leading edge of the upper platten was fixed a steel cable. A hole at the centre of the trailing edge of the lower platten received a pin secured to the base plate of the frame. With a specimen frozen into place between the plattens and a load applied to the cable, the lower platten was thus free to pivot on this pin until the ball races were self-aligned parallel to the applied force. In the original design for bench mounting in the cold room, the load cable passed over a pulley fixed to the base plate, through a hole in the bench to a spring scale of 100 kg capacity. The lower hook of the scale was replaced by a turnbuckle secured to the floor beneath the bench. The turnbuckle, allowed adjustment of the load up to the maximum capacity of the scale.

A number of 'compact' simple shear frames were subsequently built for use in sets of five in domestic deep freezers. By replacing the original pulley with a load arm (Figure 10) extending back over the frame, the frame became self-contained, compact, and suitable for use in a kerosine bath. Adjustment of the loads was simply affected by sliding lead weights along the load arms. Relative shear displacement of the upper and lower plattens was monitored with either dial micrometers (original tests) or displacement transducers mounted in a block on the base plate.

In order to restrict separation of the plattens under load, a ten kilogram lead weight was placed on the top platten in the original tests; while a compact spring loaded system was later designed to replace the bulky lead weights.

4.5 PROCEDURE

4.5.1 Uniaxial compression

For the uniaxial compression tests, specimen diameter was standardised at 25.4 mm. The synthetic samples were prepared to this dimension within very close tolerance

(Section 5.6). Natural ice specimens were first rough-cut with a band saw and then turned on a lathe to this diameter (Figure 11). One end was then trimmed, using the lathe, to form a flat surface normal to the axis of the sample. A platten was warmed in the palm of the hand, placed in the tailstock jig (Figure 11) and brought to bear against the prepared end of the specimen. The high heat capacity of the cold platten jig resulted in the platten freezing to the specimen within seconds; lateral and tilt alignment of the platten were thereby assured. With one platten thus bonded, the specimen was machined to the desired length with an excess of about 0.5 mm and the second platten similarly bonded. As the precise thickness of the plattens was known, measurement of the distance between the outer platten surfaces with a micrometer caliper to ± 0.1 mm allowed the initial length of the sample to be calculated to better than ± 0.06 per cent for the standard sample of length 150 mm.

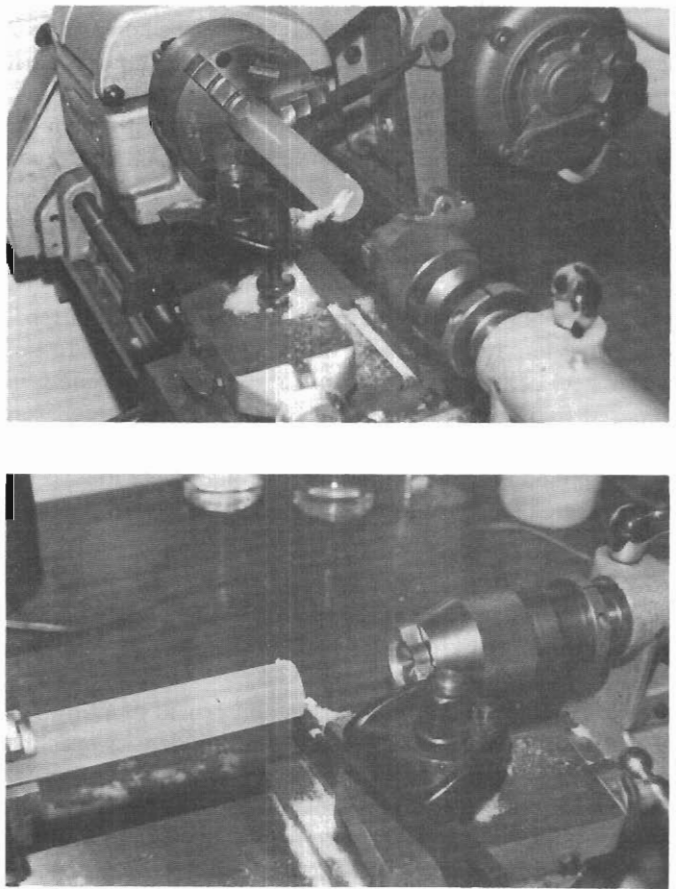

Figure 11. Preparation of sample prior to bonding the platten (upper). Platten is later placed in the tailstock jig (lower) which holds it in accurate alignment during bonding.

Once prepared, the five specimens were mounted and the reservoir topped up with pre-cooled kerosine. The loads were blocked to prohibit their immediate application, and the frame transported from the cold room to a cold box. The box was closed until thermal equilibrium had been established. Once established, the box was briefly reopened, the blocks removed, and the box closed and sealed. On several occasions the above procedure for application of the loads was carried out without actually applying the loads. The transducer outputs were recorded to establish the duration of transient effects due to opening the cold box. Significant effects in no case lasted longer than ten hours; in most cases the effects were not noticeable after one or two hours.

4.5.2 Simple shear

Standard cylindrical specimens 25.4 mm in height and from 60-100 mm in diameter were used in the shear frames. Synthetic specimens, as removed from the molds, were 95 mm in diameter and required no additional preparation of the cylindrical face. Natural specimens were rough-cut on a band saw and turned on a lathe to the required diameter. The ends of the specimen were then machined flat and parallel to obtain a height of approximately 25.2 mm. With practice, the specimen was easily frozen to the lower platten leaving a clearance of about 0.1 mm with the upper platten. By placing a massive lead weight on the upper platten during bonding to the upper platten, separation of the plattens due to the freezing process was avoided. A matrix of 3 mm holes in the upper platten were filled, one by one, using water from a syringe. By capillary action, the liquid spread out from each hole a few millimeters along the specimen-platten interface before freezing. This procedure proved quite effective in producing excellent bonds while maintaining the desired platten separation as gauged by the bearings and races. Indeed, on one occasion, while testing the strength of the bonds, the steel cable snapped with no apparent weakening of the bonds.

Having prepared five frames in the above manner, the frames were transported to a cold box or other test area and the temperature allowed to reach equilibrium before loads were applied. The bench mounted frames were loaded remotely, while the compact frames were blocked before loading as in the case of the compression tests.

4.6 PREPARATION OF SPECIMENS

The large suite of existing data relevant to the establishment of a flow law for isotropic polycrystalline ice is based, for the most part, on high density specimens exhibiting tessellate (Kamb 1972) structure. Nominal grain diameters ranging from about 0.5 mm to 3 mm have been used in various studies. From the author's experience, grain diameters less than about 1 mm show a tendency toward instability due to grain growth. Steinemann (1954) noted a lower limit of about 0.5 mm, which he attributed to effects of interface tension.

At the small total strains ($< 1\%$) expected in the proposed series of uniaxial tests, it was assumed that buckling would not become a significant problem. The maximisation of strain resolution through increased length and the maximisation of

stress homogeneity through increased L/D ratio became the primary considerations in the choice of specimen length. A practical limitation on the length of specimens was imposed by the size of the available cold boxes for the low (< − 15 °C) temperature tests, this limit being approximately 150 mm.

The minimisation of desirable specimen diameter, in order to maximise L/D and minimise the magnitude of applied forces necessary to obtain a given octahedral shear stress, then relied on the preparation of fine grained specimens. It was determined that the smallest stable grain diameter obtainable, using the procedure described below, was about 1 mm, implying (page 22) a minimum desirable specimen diameter of approximately 25 mm. For convenience, a mold of internal diameter 25.4 mm was chosen for the preparation of specimens to be used in the uniaxial tests. L/D ratios were 5.4 and 5.9 for the high (0.028 to 0.28 MN m^{-2}) and low (0.005 to 0.05 MN m^{-2}) octahedral stress ranges, respectively.

In order to maintain a basis for comparison with previous studies, a relatively simple method was devised (Jacka and Lile 1984) for the preparation of clear, finegrained, isometric (1.5 — 2.0 mm diameter), tessellate, high density, randomly oriented specimens. A notable simplification in procedure and apparatus along with a possible gain in quality control was achieved in comparison with the most successful previous techniques (cf. Glen 1952).

If the results of laboratory creep tests are to be applicable to the flow rates of natural ice masses, it is evidently (Budd, 1972) necessary that deforming specimens exhibit structures compatible with the magnitude, configuration and orientation of the applied stresses. This requirement of compatibility may preclude the preparation, by rapid prestraining, of laboratory specimens possessing both orientational and textural structures equivalent to those evolved at low stress magnitudes over geological time scales. The alternative is selection of natural specimens exhibiting natural structural compatibility.

Deep bore hole cores are available extending through regions of diversified stress situations and a wide range of temperatures. Structural compatibility is evidently preserved (Rigsby 1960, Howard 1948 and Seligman 1948) when cores are quenched and maintained at temperatures below about − 10 °C following removal from their field sites. With a knowledge of *in situ* conditions of stress and temperature (measured or calculated) these parameters can be reinstated on selected specimens in the laboratory with some confidence in compatibility between structure, temperature and stress situation as well as in the tectonic significance of subsequent strain increments.

4.7 DATA LOGGER

Those frames equipped with electrical displacement transducers were interfaced to a scanning data logger. The scanning rate of the data logger was ten specimens per hour. During each measurement cycle, the analogue transducer output was digitised, providing a digital 254 second average. Near the end of the cycle, the digitised transducer output along with various book-keeping data such as a sequential data tape identification number, sample number and elapsed time, were multiplexed onto an output data bus to be recorded. A highly stable and accurate power supply furnished power to the transducers. The ± 10 volt analogue output of each transducer was brought to the input port of a Solartron 3300 analogue scanner by means of

a guarded cable. The output of the selected transducer passed through the scanner to a voltage-to-frequency converter. Its pulse-train output was gated at the input of a frequency counter. The digital counter output merged with the book-keeping data at the multiplex bus. A system controller, receiving time signals from the system clock, controlled the sequence of events during the measurement cycle. Each measurement cycle began with a two-second synchronising pulse generated by the controller. This pulse incremented the scanner's address generator, placing a new sample 'on-line'. Simultaneously, the frequency counter was reset to begin a new count. The two-second duration of the synchronising pulse offered the voltage-to-frequency converter ample time to 'settle in' to the new transducer voltage before the frequency counter gate opened, allowing the averaging period to begin. The pulses generated by the voltage-to-frequency converter were then summed until the counter gate closed at the beginning of the 256th second of the measurement cycle. The resulting 254-second period during which the counter gate was open in effect resulted in a hardware conversion of the analogue transducer output into metric units, with a resolution of one nanometer per hertz. Two low order decades were discarded due to noise content so that the output resolution passed on to the recording device was 0.1 micrometers. During certain low creep rate tests the transducers were operated between $\pm$ 1.0 volt and the voltage-to-frequency converter over a similar range, resulting in a 0.01 micrometer resolution. During the final 8 seconds of the measurement cycle, the multiplexer address generator and punch command were activated, sequentially placing the appropriate data on the output bus to be punched on paper tape.

On the front panel of the data logger, digital displays exhibited the current elapsed time, sample number and displacement. Thumbwheel switches allowed the selection of a particular sample in manual mode or, in automatic mode, set the number of samples to be scanned. A second set of thumbwheel switches were used to set the tape sequence number.

4.8 DATA PROCESSING

Data tapes were removed from the paper tape punch at approximately weekly intervals, each tape being identified by its unique sequence number. Data processing was performed on the departmental (University of Melbourne, Department of Meteorology) Interdata 70 computer.

During the first stage of computer processing, the tape was read and echoed on a line printer, the data edited to confirm proper operation of the logger, a table of physical parameters associated with the frames and samples currently in use appended, and a floppy disc file of the week's data generated.

A second stage of processing began with a pass through an index of tests in progress. Continuing tests were identified, data files retrieved from disc and the most recent results concatenated to the files. New files were then opened for newly initiated tests. The displacement function of each sample (displacement in microns versus elapsed time in hours) was exhibited on the graphical display unit and photographed. An independent disc file was thereby kept for each specimen tested. The displacement data and all physical parameters associated with the test were contained in the sample's file. These files were used in the third stage of processing, the calculation of strain rates.

5. Results and conclusions

In this final section, the theoretical, technical and empirical aspects of the present study are combined to illustrate a feasible approach to the quantitative incorporation of crystallographic effects into the flow law for polycrystalline ice.

5.1 EXPERIMENTS ON ISOTROPIC AGGREGATES

In order to augment previous creep studies of isotropic polycrystalline ice, and particularly to extend such studies to include conditions of temperature and shear stress relevant to cold ice masses, a systematic laboratory investigation covering the range from $-10\,°C$ to $-50\,°C$ and 0.005 to 0.28 MN m^{-2} octahedral was undertaken. Figure 12 identifies the conditions imposed on the thirty-four individual samples tested. Seven group experiments were carried out at fixed temperatures. Each experimental group comprised five (with one exception) samples loaded at shear stresses equally spaced on a logarithmic scale over one order of magnitude. Two ranges of octahedral shear stress were used: experiments identified by the letter C ranged from 0.005 MN m^{-2} to 0.05 MN m^{-2}; and the letter D identifies experiments in the range from 0.028 MN m^{-2} to 0.28 MN m^{-2}.

In total, the present laboratory study on isotropic aggregates has involved more than 150 000 sample hours. Experiments C4, C5, C6, D2 and D3 explore a corner of the flow law diagram (Figure 1) relatively neglected by previous studies, but of particular importance in establishing a flow law for polar ice masses.

An additional five samples exhibiting mean grain sizes ranging over more than two orders of magnitude from 1.4 mm^2 to 160 mm^2 were tested in simple shear at $-10.3\,°C$ and 0.04 MN m^{-2} octahedral to assess the effect of grain size on the creep rate of an isotropic aggregate. No significant or systematic difference in creep rates was observed except for one sample which was significantly higher. To assess the cause of this higher creep rate, the specimens were removed from the simple shear frames, rotated 90° about the platten normal and rebonded. In the subsequent test a second sample showed an anomalously high creep rate. It was concluded that the anomalous creep rates were due to inadequate platten bonds with no significant effect attributable to grain size. As a partial consequence of the suspected bonding problem, the isotropic tests were carried out in uniaxial compression. As the ratio of grain size to sample size would appear to be more critical (page 22), than grain size alone, the smallest stable grain size attainable using the technique described by Jacka and Lile (1984) was used.

With the platten bonding problem for simple shear tests now evidently solved (page 21), a new series of tests covering the original range of grain sizes and also a variety of temperatures and shear stresses is being planned to check and extend the original results under improved experimental conditions.

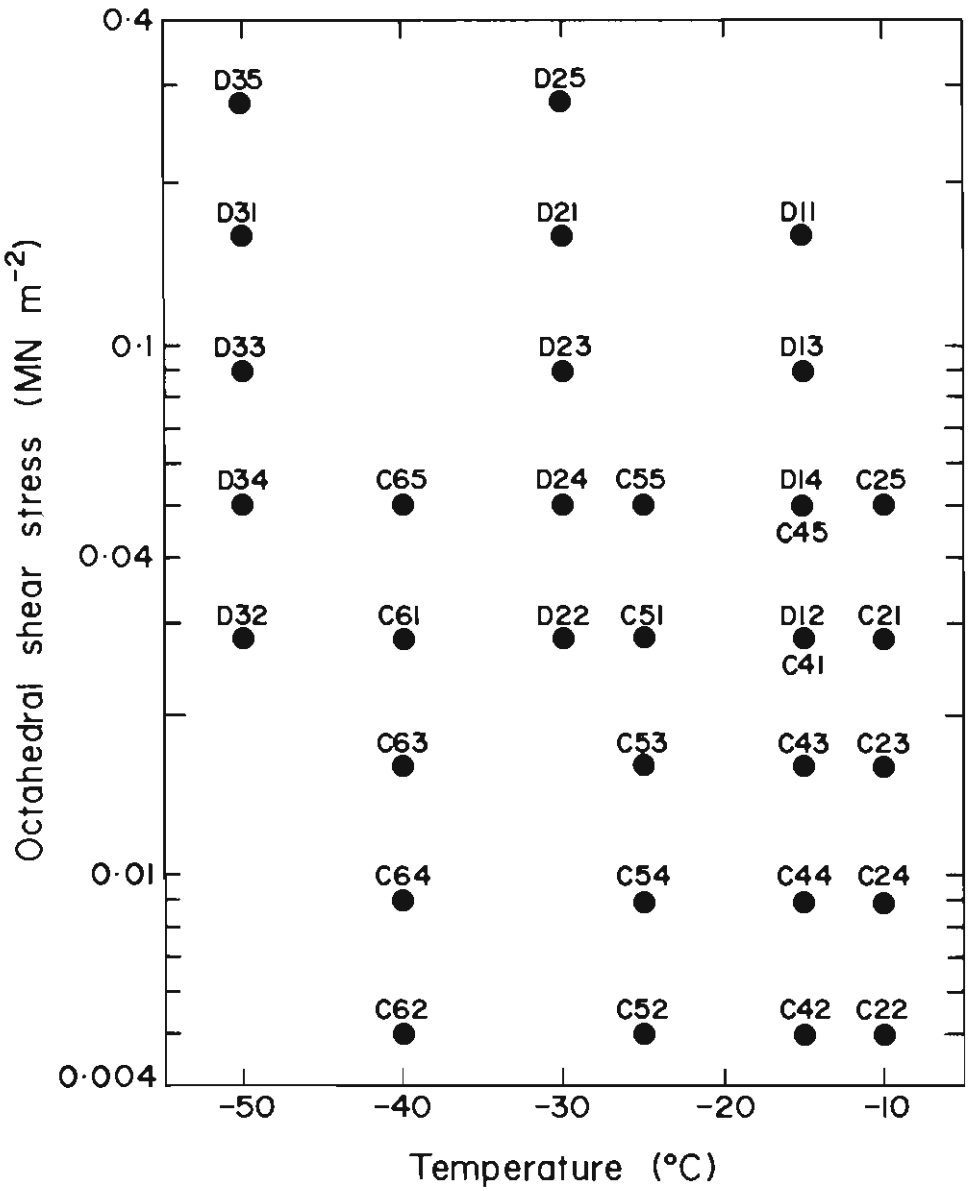

Figure 12. Summary of experimental conditions imposed on isotropic specimens in uniaxial compression.

5.1.1 Results

Creep curves of platten displacement versus time are shown in Figures 13 to 19 for each of the isotropic creep experiments. Secondary creep rates were sought to construct a flow law based on these data. Even though some of the samples have been under load for more than 11 000 hours and are continuing, the total strains achieved are still very small, and the secondary stage of creep has not been reached. Thus secondary creep rates cannot be obtained directly from these rheologically short-term experiments. The problem then is how to extrapolate the observed data to yield estimates of the steady-state rates. The relatively unique automatically logged creep data were, by nature of their high time resolution and computer compatibility, ideally suited to computerised curve fitting techniques.

Two different analytical functions were examined for their ability to represent the measured strain versus time relationship. Three terms were included in each function: a constant term (ϵ_e) to account for the elastic response of both the sample and the creep frame; a linearly time dependent term (Kt), where the coefficient K is the final or steady-state creep rate; and a transient term which becomes negligibly small at suitably long times. The two analytical functions differed in the form of the transient terms. The first form was a McVetty (exponential) function of time

$$\epsilon(t) = \epsilon_e + Kt + \epsilon_t(1 - e^{-\beta t}) \tag{5.1}$$

and the second

$$\epsilon(t) = \epsilon_e + Kt + (\beta t)^{\gamma} \tag{5.2}$$

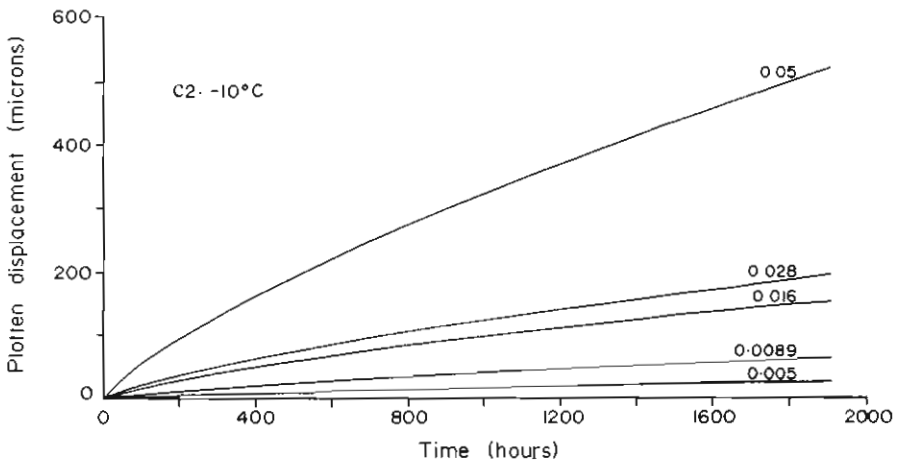

Figure 13. Creep curves of axial displacement versus time. Octahedral shear stress is indicated in MN m⁻². Sample C2: −10 °C.

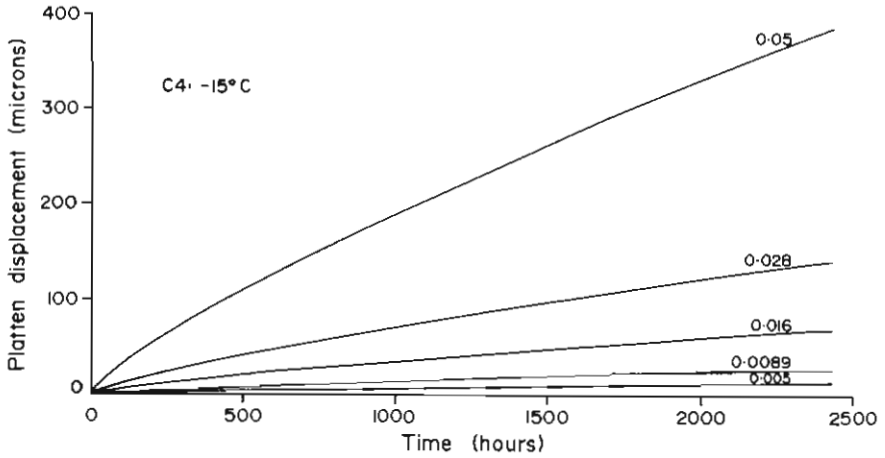

Figure 14. Creep curves of axial displacement versus time. Octahedral shear stress is indicated in MN m^{-2}. Sample C4: – 15 °C.

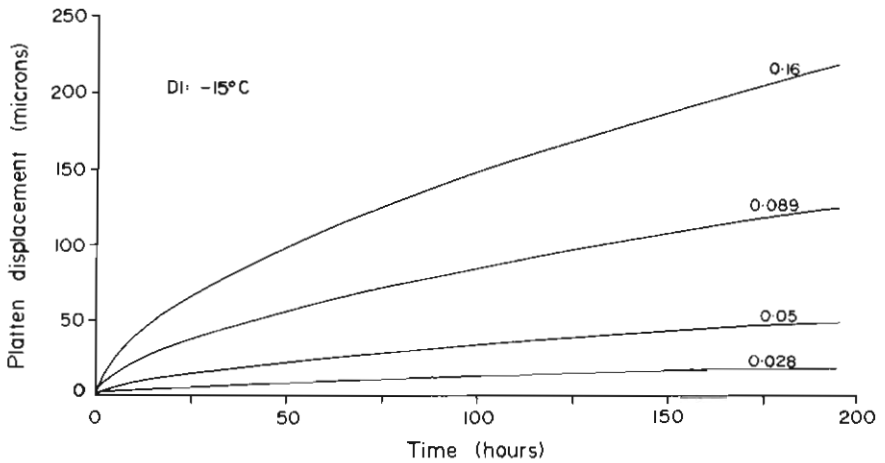

Figure 15. Creep curves of axial displacement versus time. Octahedral shear stress is indicated in MN m^{-2}. Sample D1: – 15 °C.

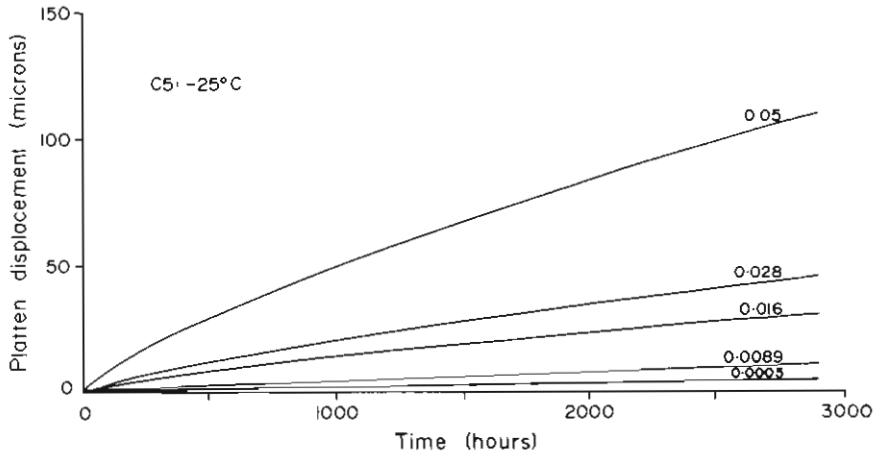

Figure 16. Creep curves of axial displacement versus time. Octahedral shear stress is indicated in MN m⁻². Sample C5: – 25 °C.

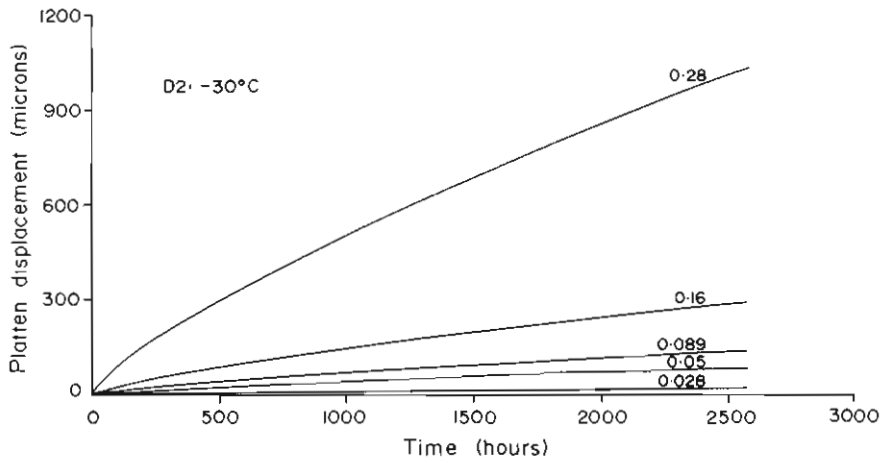

Figure 17. Creep curves of axial displacement versus time. Octahedral shear stress is indicated in MN m⁻². Sample D2: – 30 °C.

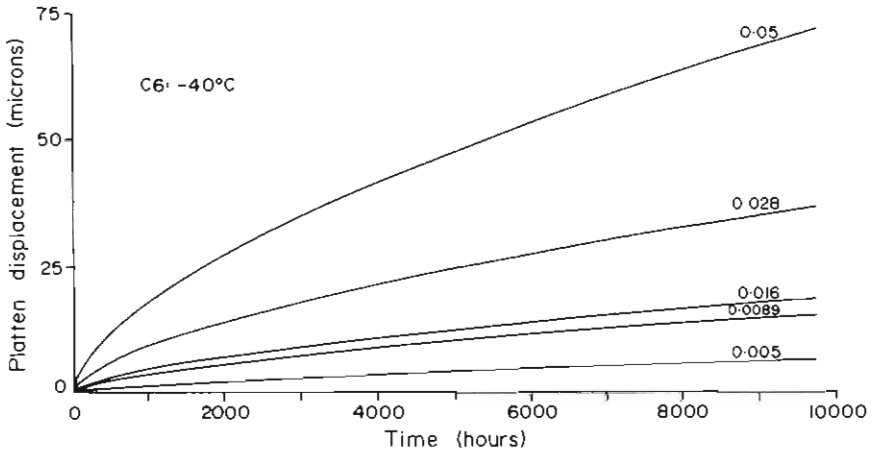

Figure 18. Creep curves of axial displacement versus time. Octahedral shear stress is indicated in MN m⁻². Sample C6: – 40 °C.

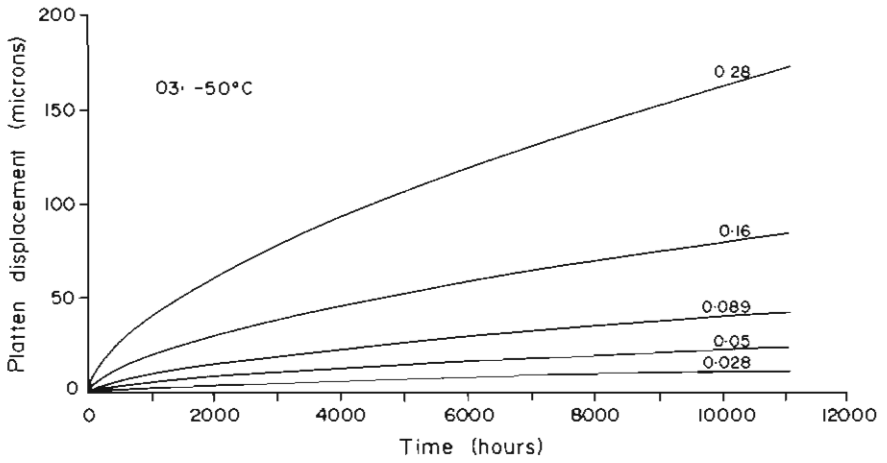

Figure 19. Creep curves of axial displacement versus time. Octahedral shear stress is indicated in MN m⁻². Sample D3: – 50 °C.

an Andrade (power) function of time (cf. Rotherham 1951). For each form, a least squares regression technique was used to minimise the variance simultaneously for the several fit parameters (ϵ_e, K, β and ϵ_1) and yield the best fit values.

Differences in the mean residual variance found for each of these classical analytic creep functions was small compared with sample-to-sample differences. Thus it cannot be stated with reasonable confidence which form is the more suitable representation of the observed data. To evaluate the ability of each form to extrapolate the observations beyond the duration of the experiments, differences between the observed and best-fit analytical curves were plotted against time. Systematic deviations appeared for each form; typically two crossover points were exhibited with the function diverging from the observed creep curve at the conclusion of the experiments. The McVetty form gave time constants (β^{-1}) shorter than the duration of the experiments, implying that steady-state rates had been reached within a few per cent or less by the time the experiments had concluded. When the experiments were artificially shortened by neglecting various amounts of data and the shortened curves fitted, β^{-1} decreased in proportion. Some comments concerning the divergence found using the Andrade law appear in Section 5.1.2.

Because both analytic functions tend to diverge from the observed data toward the end of the experiments, it must be concluded that neither can adequately extrapolate rheologically short-term data to secondary creep rates. An alternative approach is presented in the following section.

5.1.2 Discussion

Some interesting results have emerged from a parallel laboratory investigation by Jacka (1984) of isotropic samples similar to those used for the present study. His creep tests in uniaxial compression covered octahedral shear stresses from about 0.05 MN m^{-2} to 1.2 MN m^{-2} at temperatures of about -5 °C to -32 °C. Under these conditions many of Jacka's samples reached minimum creep rate. When plotted in log $\dot{\gamma}_o$ – log t co-ordinates (Figure 20) his creep data exhibit two systematic features:

(a) Prolonged steady-state creep rates are not observed; instead the secondary stage of creep degenerates to an equilibrium state characterised by a minimum octahedral creep rate $\dot{\gamma}_{om}$. The locus of minimum values is revealed as a straight line corresponding closely with an accrued octahedral shear strain of 0.6 to 0.7 per cent.

(b) Within the range of temperature and shear stress so far examined this locus seems to be independent of shear stress and temperature over three orders of magnitude of $\dot{\gamma}_{om}$. At temperatures below -10 °C the observed equilibrium creep rates are described by a flow law of the form

$$\dot{\gamma}_{om} = A \exp(-Q/RT)\, \tau_o^n \qquad (5.3)$$

with $A = 1.87 \times 10^9$ sec^{-1} MN^{-n} m^{6n}; $Q = 18$ Kcal $mole^{-1}$; $n = 3$; $R = 1.9$ cal $mole^{-1}$ $°K^{-1}$; and T, the temperature in °K. Jacka's observed equilibrium creep rates at -10 °C and -17.8 °C are shown as open circles in Figure 21. Dashed lines calculated using equation (5.3) with the values given above are shown for $\tau_o \geq 0.16$ MN m^{-2}.

Pending any evidence to the contrary, it can be assumed that the locus of equilibrium creep rates identified in Figure 20 can be extended to smaller values of $\dot{\gamma}_{om}$. With this assumption, it is possible, in principle at least, to extrapolate

rheologically short-term creep data to estimate equilibrium creep rates as well as the time necessary to realise them. Until the form of the log $\dot{\gamma}_o$ – log t creep function is better understood, it is presently possible to determine only the upper and lower bounds on equilibrium creep rates expected from short-term experiments. The upper bound is the last observed creep rate; while the lower bound is found from a linear extrapolation of the observed log $\dot{\gamma}_o$ – log t creep curve to the locus of $\dot{\gamma}_{om}$ values.

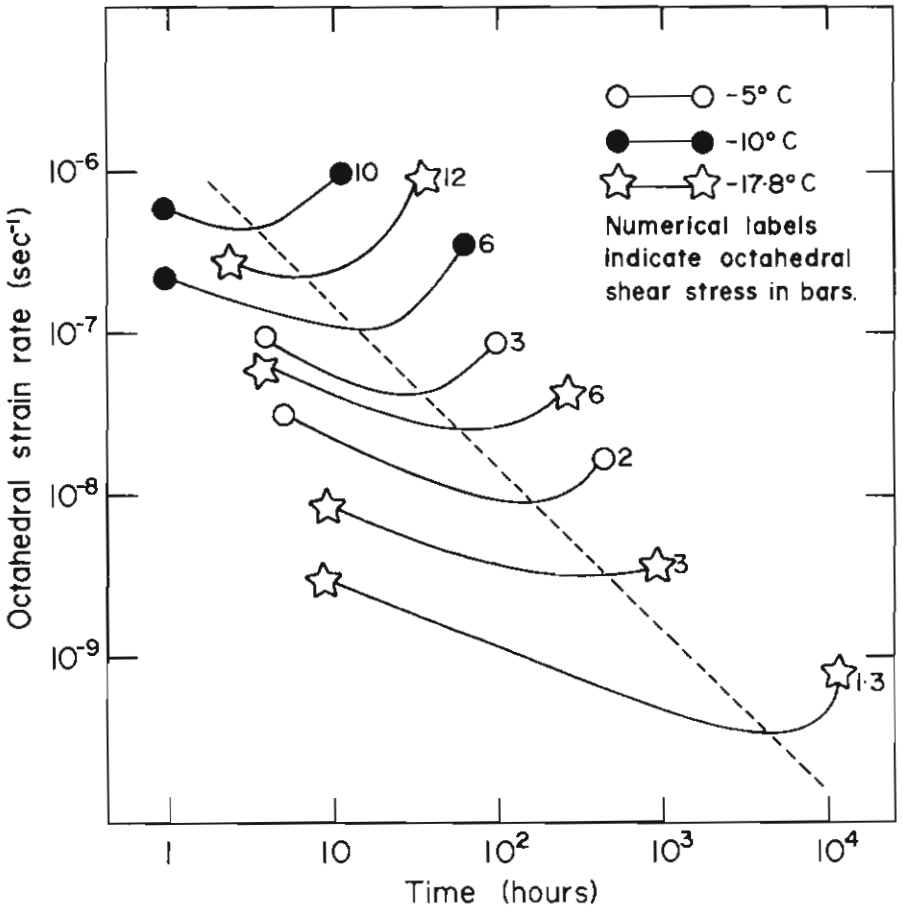

Figure 20. A typical sample of log $\dot{\gamma}_o$ versus log t creep curves for isotropic specimens in uniaxial compression. (After Jacka 1984).

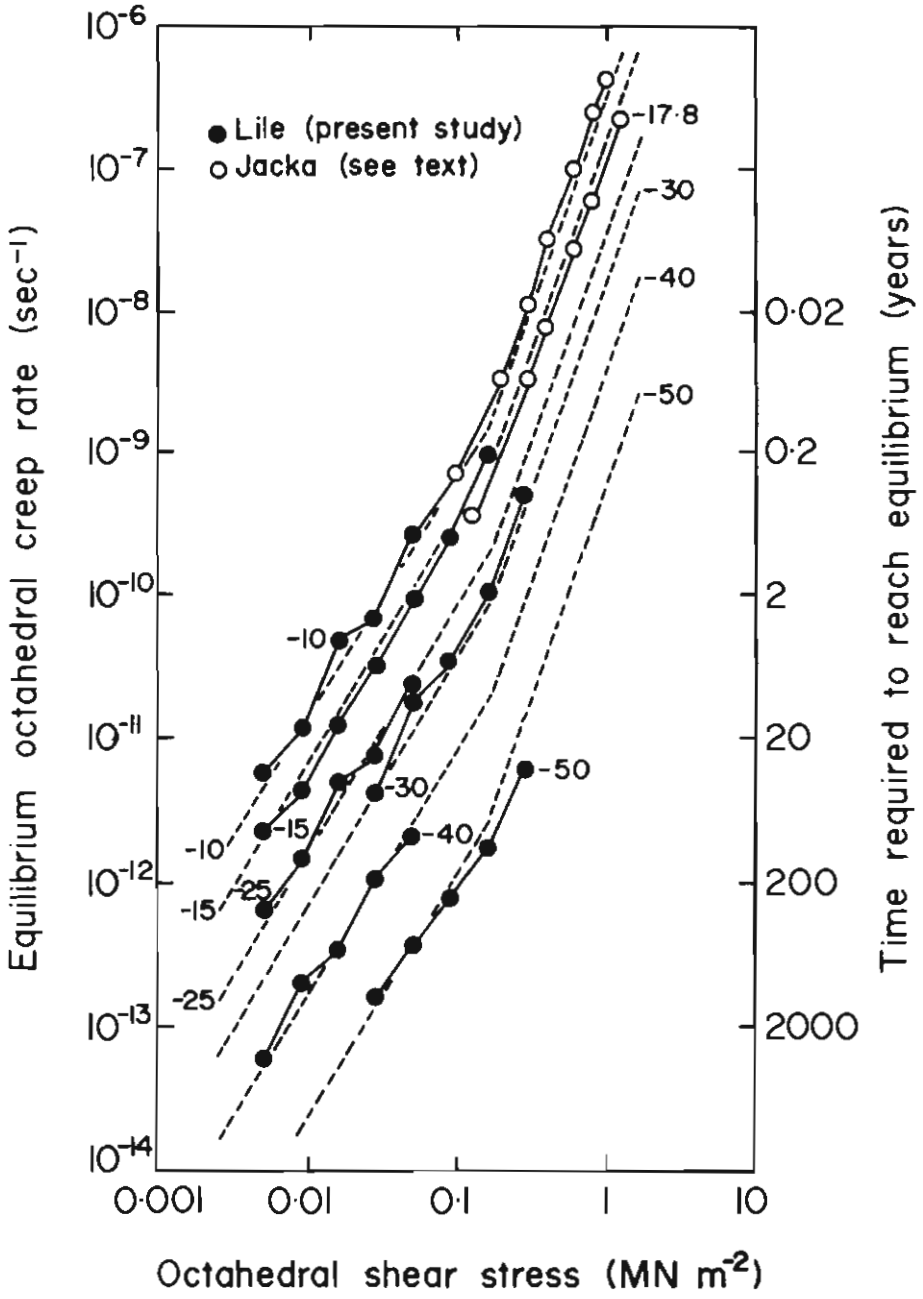

Figure 21. Flow law for isotropic polycrystalline ice based on (○) observed equilibrium creep rates (after Jacka 1984) and (●) present experiments extrapolated to equilibrium creep rates. Estimated times necessary to reach equilibrium are also shown.

Smoothed curves of log $\dot{\gamma}_o$ versus log t have been computed from the present data and are displayed in Figures 22 to 28 as solid curves with extrapolations to the lower bounds being shown as dashed lines. For each sample the value of $\dot{\gamma}_{om}$ has been calculated as the logarithmic mean of the upper and lower bounds; these values are shown as solid circles. The errors attributable to extrapolation are indicated as error bars extending from the upper to the lower bound. The number near each estimate of $\dot{\gamma}_{om}$ gives the octahedral shear stress applied to the sample. The calculated values of $\dot{\gamma}_{om}$ have been transferred to Figure 21 where they are entered as solid circles. A flow law of the form given by equation (5.3) with A = 1.72 x 10^8 sec^{-1} $MN^{-1.7}$ $m^{3.4}$, Q = 18 Kcal $mole^{-1}$ and n = 1.7 is found to describe these data reasonably well. Curves calculated on this basis are shown in Figure 21 as dashed lines for $\tau_o \leq 0.16$ MN m^{-2}. An apparent transition in the value of n from 3 to 1.7 at octahedral shear stresses below about 0.16 MN m^{-2} suggests the possibility of different rate controlling mechanisms operating above and below this value of shear stress. However, in the decade of equilibrium creep rates between 10^{-9} sec^{-1} and 10^{-10} sec^{-1} the time required to actually achieve equilibrium increases from two or three months to about two years. At creep rates greater than 10^{-9} sec^{-1} the values entered in Figure 21 are based on observation; below 10^{-10} sec^{-1} they must so far be based on extrapolation. When the errors associated with this extrapolation (Figures 22 to 28) are considered, a flow law with n = 3 extending to very small creep rates cannot be entirely ruled out by the present data.

Returning now to Figures 22 to 28, it is notable that the log $\dot{\gamma}_o$ – log t creep curves appear to be linear until they approach the locus of equilibrium values. Their slopes during the dominantly primary stage of creep are evidently independent of

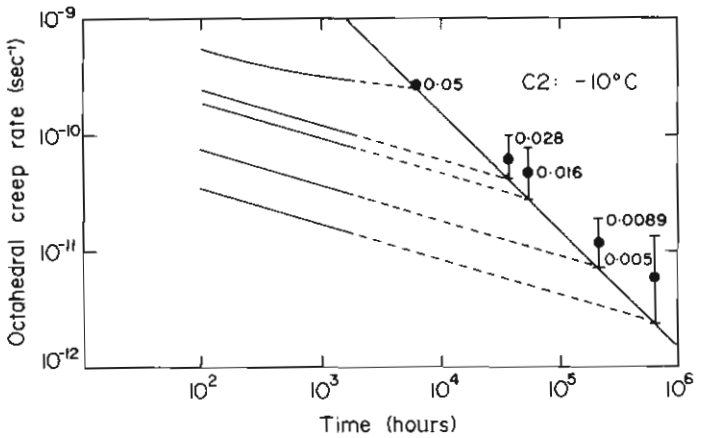

Figure 22. Smoothed curves of log $\dot{\gamma}_o$ versus log t with extrapolations to equilibrium curve shown as dashed lines. Octahedral shear stress is indicated in MN m^{-2}. Sample C2: – 10 °C.

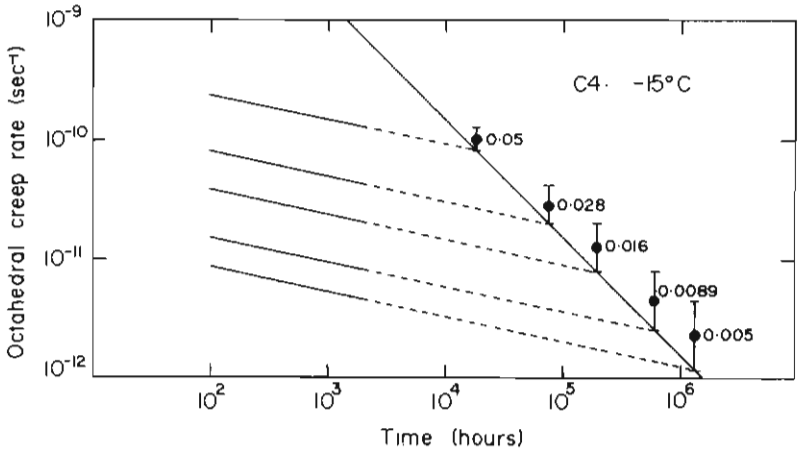

Figure 23. Smoothed curves of log $\dot{\gamma}_o$ versus log t with extrapolations to equilibrium curve shown as dashed lines. Octahedral shear stress is indicated in MN m^{-2}. Sample C4: −15 °C.

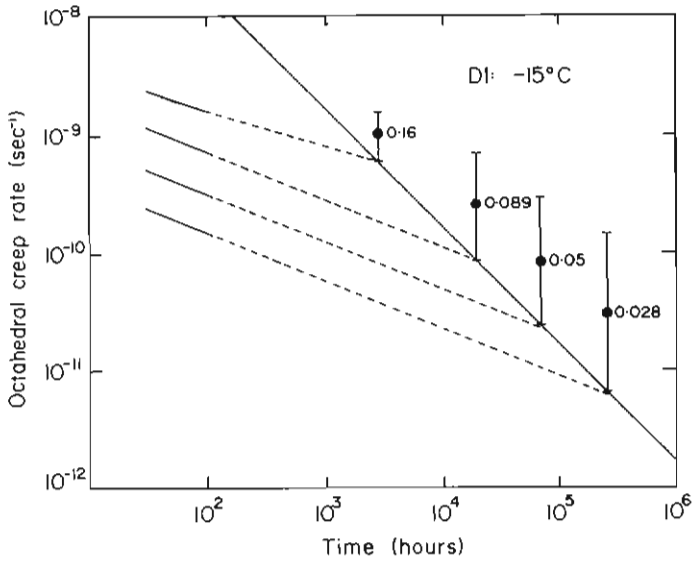

Figure 24. Smoothed curves of log $\dot{\gamma}_o$ versus log t with extrapolations to equilibrium curve shown as dashed lines. Octahedral shear stress is indicated in MN m^{-2}. Sample D1: −15 °C.

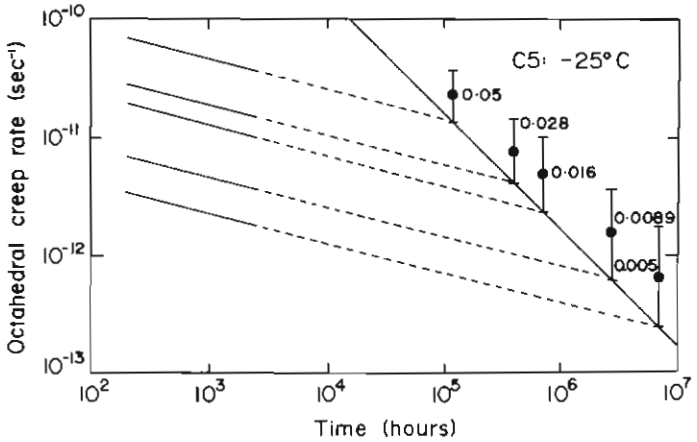

Figure 25. Smoothed curves of log $\dot{\gamma}_o$ versus log t with extrapolations to equilibrium curve shown as dashed lines. Octahedral shear stress is indicated in MN m^{-2}. Sample C5: – 25 °C.

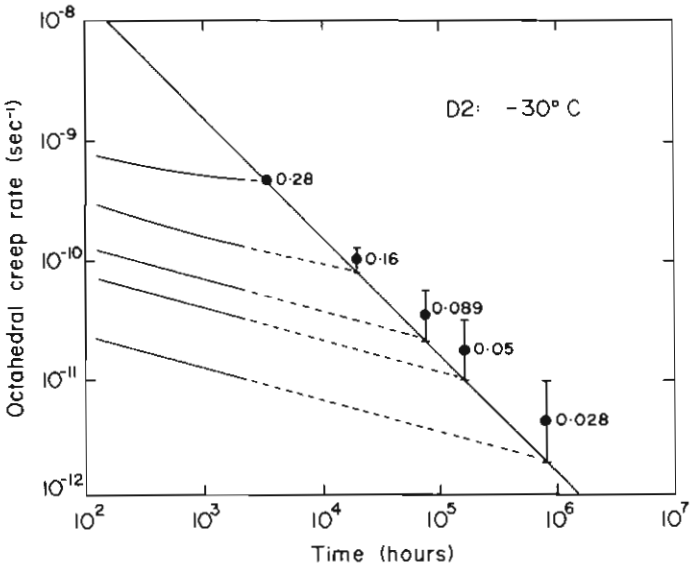

Figure 26. Smoothed curves of log $\dot{\gamma}_o$ versus log t with extrapolations to equilibrium curve shown as dashed lines. Octahedral shear stress is indicated in MN m^{-2}. Sample D2: – 30 °C.

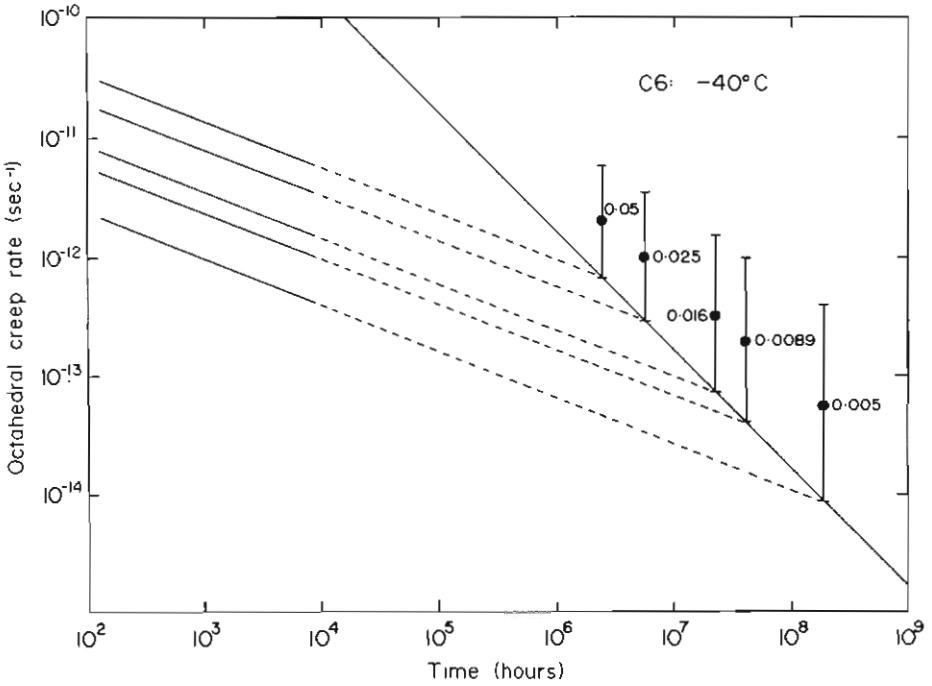

Figure 27. Smoothed curves of log $\dot{\gamma}_o$ versus log t with extrapolations to equilibrium curve shown as dashed lines. Octahedral shear stress is indicated in MN m^{-2}. Sample C6: − 40 °C.

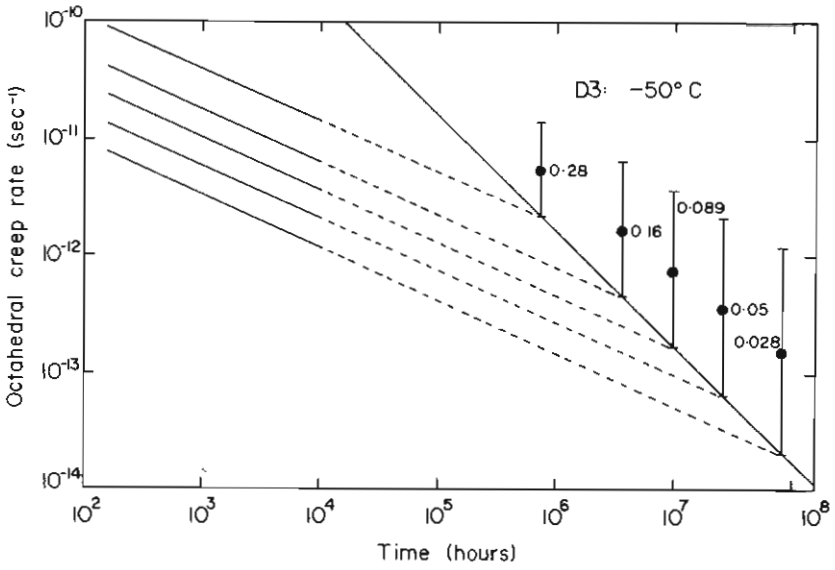

Figure 28. Smoothed curves of log $\dot{\gamma}_o$ versus log t with extrapolations to equilibrium curve shown as dashed lines. Octahedral shear stress is indicated in MN m^{-2}. Sample D3: − 50 °C.

shear stress with some indication of a slight dependence on temperature. Also, for creep rates in the primary stage, $\dot{\gamma}_o$ remains linearly proportional to τ_o when evaluated at equal times. The linearity between log $\dot{\gamma}_o$ and log t suggests a further examination of the Andrade law (equation 5.2) in the more general form

$$\gamma_o = \gamma_e + Kt + (\beta t)^m. \tag{5.4}$$

The octahedral creep rate is

$$\dot{\gamma}_o = K + m\,\beta^m\,t^{m-1}. \tag{5.5}$$

Then

$$d\dot{\gamma}_o = m(m - 1)\,\beta^m\,t^{m-2}\,dt \tag{5.6}$$

which, when combined with equation (6.5), yields

$$\frac{d\dot{\gamma}_o}{\dot{\gamma}_o} = \frac{m(m - 1)\,\beta^m\,t^{m-1}}{K + m\,\beta^m\,t^{m-1}}\,\frac{dt}{t} \tag{5.7}$$

For short-term creep experiments the transient term dominates the secondary term so that $K << m\,\beta^m\,t^{m-1}$. As a result

$$\frac{d(\log\,\dot{\gamma}_o)}{d(\log\,t)} = m - 1 \tag{5.8}$$

From the observed slopes, $d(\log\,\dot{\gamma}_o)/d(\log\,t)$, shown in Figures 22 to 28, it is found that the value of m varies approximately from 0.6 at $-50\,°C$ to 0.75 at $-10\,°C$. These values differ significantly from the value of one third found by Andrade and others to be relevant to metallurgical materials. By forcing m to be one-third when fitting the present creep curves tothe classical Andrade law (Section 5.1.1), an exaggerated value of K must have been generated to compensate for the larger value of m characteristic of the empirical curves for ice. In this case the best fit Andrade function with m = 1/3 would be expected to exhibit an artificial curvature, which evidently contributed to the present failure of the Andrade function as a tool for the extrapolation of rheologically short-term creep rates to secondary values. The more general Andrade law (equation 5.4) certainly merits further investigation in this regard. However, its usefulness may be limited, as very long creep tests will still be required to yield confident estimates of K. Jacka's data have shown that a prolonged period of unaccelerated creep is not a characteristic feature of isotropic creep at temperatures between $-5\,°C$ and $-18\,°C$ and at shear stresses as low as 0.1 MN m^{-2}. If this trend continues at smaller stresses and lower temperatures, a flow law based on secondary creep rates could not be directly substantiated by experiment.

Alternately, by prestraining isotropic aggregates to an accrued strain of nearly one per cent at an elevated stress and/or temperature, the time necessary to reach small equilibrium creep rates could be shortened considerably. The effects of prestraining on equilibrium creep rates will need to be determined, e.g. by comparative tests at creep rates above about 10^{-9} sec^{-1}. If the effects are found to be small, it might then be possible to construct a purely empirical flow law for isotropic ice based on equilibrium creep rates extending to very small values. This possibility is being considered as a future area of study at the University of Melbourne.

The present isotropic creep tests have resulted in the construction of the first comprehensive laboratory extension of the flow law for isotropic aggregates (Figure 21) to $-50\,°C$ and 0.005 MN m^{-2}. An activation energy of 18 Kcal $mole^{-1}$ is indicated throughout this region of small creep rates. The present evidence points to a value of n in the range 1.7 to 3. When compared to previous short term laboratory studies which suggested a linear flow law at small creep rates (Figure 1), the errors in predicting creep rates under conditions of shear stress and temperature characteristic of polar ice masses are thus reduced by more than an order of magnitude. With this improvement in the flow law for isotropic aggregates, it becomes even more pressing to consider the empirical effects of anisotropic crystallography on strain rate.

5.2 EXPERIMENTS ON ANISOTROPIC AGGREGATES

Present and past laboratory results indicate that creep rates observed during short-term creep experiments on isotropic aggregates are described by a linear ($n = 1$) flow law. When a constant load is applied to a prestrained anisotropic aggregate after a prolonged period of relaxation, it will be assumed that the resulting creep rate will also exhibit a linear dependence on stress during the dominantly primary stage of creep. By adopting this assumption, it becomes possible to test the linear enhancement model developed in Section 3 with short-term laboratory creep tests at small creep rates.

In view of the paucity of suitably documented creep tests on crystallographically anisotropic aggregates, several experiments were designed specifically to provide empirical as well as model-derived enhancements in uniaxial compression ($\Lambda = -1$) and pure shear in two dimensions ($\Lambda = 0$) between equidistant plattens, i.e. simple shear. Borehole cores obtained from Law Dome Antarctica provided the prestrained, anisotropic specimens for the tests.

5.2.1 Experimental results

Anisotropic ice cores were obtained from two quite different stress situations at Law Dome. Specimens cut from these cores were subjected in the laboratory to stress configurations simulating both *in situ* and anomalous conditions. Three specimens were prepared from the 318 m depth core at site SGD, the Dome summit, a region approximating (McLaren, 1968) uniaxial compression. The symmetric girdle fabric of the parent core is illustrated in Figure 29a. Two of the specimens (318D1 and 318D2) were loaded in uniaxial compression as *in situ*. A third specimen (318D3) was tilted 90° to the *in situ* case with the axis of compression normal to the axis of symmetry of the girdle fabric. The octahedral shear stress and temperature in each of these creep tests were 0.005 MN m^{-2} and $-10.2\,°C$, respectively.

A second set of three specimens was prepared from the 200 m depth core at site SGF near Cape Folger. The parent core exhibited a strong single pole fabric (Figure 29b), indicative of its history of laminar (simple shear) flow in that region. In order to reinstate the *in situ* flow situation, these specimens were mounted between parallel plattens and a constant shear load applied. The plattens were constrained to remain equidistant (Section 4.4.2). Specimen 200F1 was oriented as *in situ* (single pole fabric

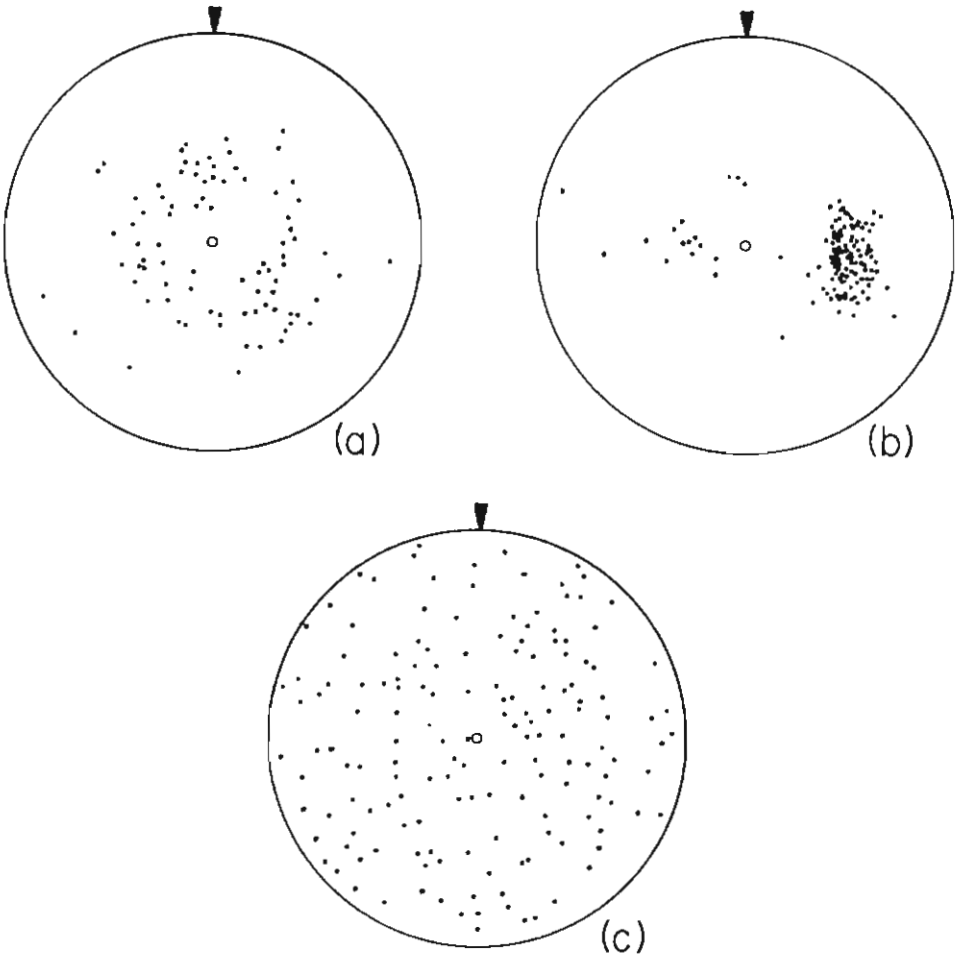

Figure 29. Fabrics of (a) a horizontal section of Dome summit core from a depth of 318 m; (b) Cape Folger core from 200 m depth, sectioned at 45° to the horizontal; and (c) laboratory prepared isotropic ice.

axis of symmetry normal to the plattens), while the fabric axes of specimens 200F2 and 200F3 were tilted at 22.5° and 45° respectively, into the direction of the applied shear stress. These tests were conducted at 0.04 MN m^{-2} octahedral and -6°C.

With each set, an isotropic polycrystal of similar grain size (prepared as described in Section 4.6) was tested under identical conditions. A typical measured orientation fabric for the laboratory-prepared specimens is shown in Figure 29c. The observed creep curves of platten displacement versus time are shown in Figures 30 and 31. Empirical component enhancements were computed as the ratios of the slopes of the creep curves of the anisotropic aggregate to the associated slopes of the curves for the isotropic control samples. The slopes were calculated for the final 100 hours of each test, and represent uniaxial and simple shear creep rates at approximately 0.5

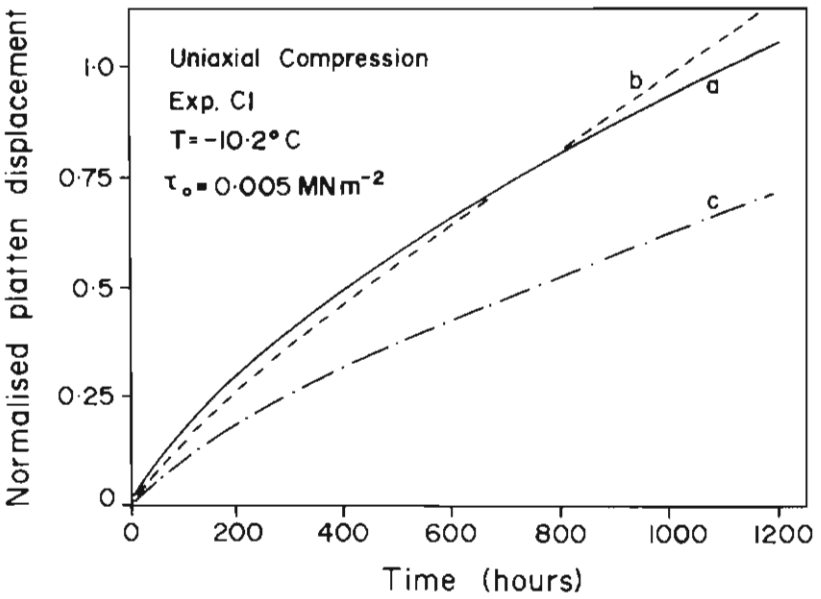

Figure 30. Normalised creep curves of platten displacement versus time for short-term uniaxial experiments on (a) isotropic control specimen; (b) anistropic specimens 318D1 and 318D2 loaded as in situ; and (c) anisotropic specimen 318D3 loaded perpendicular to the fabric axis of symmetry.

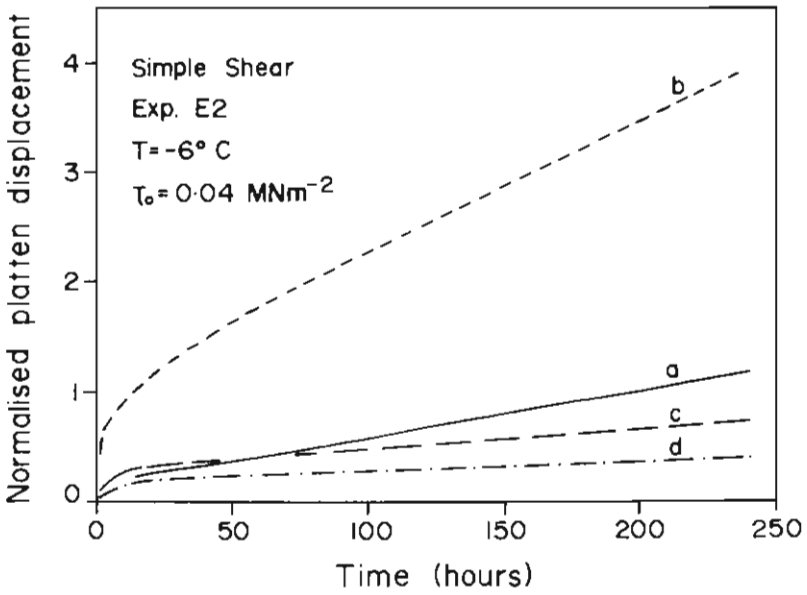

Figure 31. Normalised creep curves of platten displacement versus time for short-term simple shear experiments on (a) isotropic control specimen; (b) anisotropic specimen 200F1 loaded as in situ; (c) anisotropic specimen 200F2 loaded with fabric axis of symmetry tilted 22.5° into the direction of shear; and (d) anisotropic specimen 200F3 loaded with fabric axis of symmetry tilted 45° into the direction of shear.

per cent and 5 per cent respectively, of the time estimated to reach equilibrium isotropic values. Thus the experiments are rheologically short term, so that the observed component enhancements can be considered linear. The linear short term component enhancements measured for each of the six anisotropic aggregates are shown as solid circles in Figures 32 and 33.

5.2.2 Results from the enhancement model

For each test, the measured orientation fabric of the parent core and the relevant stress-configuration parameter were presented as inputs to a computer program which performed the numerical integrations and calculations required to evaluate the model-derived component enhancements. The model was run for various angles of tilt (θ_f) between the platten normal and the axis of symmetry of the observed fabric. The results are summarised in the curves of Figures 32 and 33.

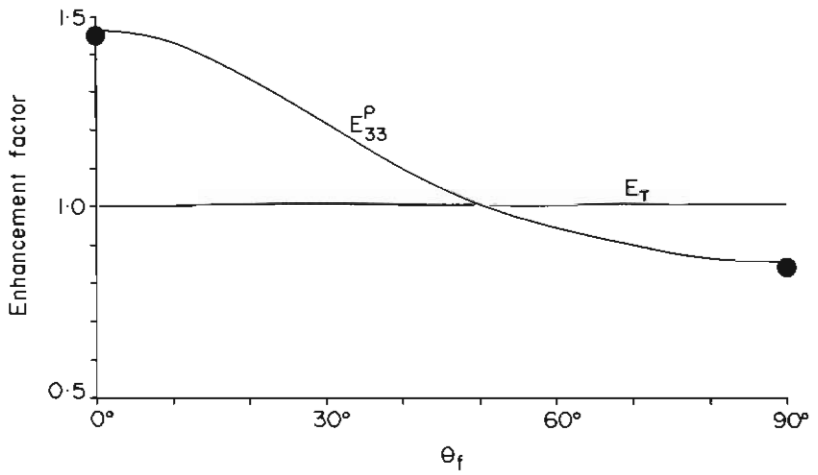

Figure 32. Model-derived linear enhancement factors for axial component of creep rate (E^{P}_{33}) and octahedral shear stress (E_T) versus angle of tilt (θ_f) of fabric axis of symmetry from load axis. Solid circles indicate measured axial enhancement factors for short-term uniaxial tests.

5.2.3 Discussion

The variety of test conditions that could be examined by the present study was necessarily limited. However, the conditions selected were sufficiently diverse to constitute a fair test of the linear enhancement model and to provide the first well-documented short-term laboratory results replicating conditions of well developed anisotropic crystallography in natural ice masses. The strong correlation between measured and model-derived component enhancements for both natural and anomalous relationships between stress configuration and crystallography, indicated in Figure 34, supports the validity of the linear model for short-term laboratory creep tests at small creep rates.

Current and future work aimed at extending both the laboratory and modelling aspects of the present study of crystallographic anisotropy to more nearly approximate conditions of equilibrium in natural ice masses is discussed in Section 5.3.

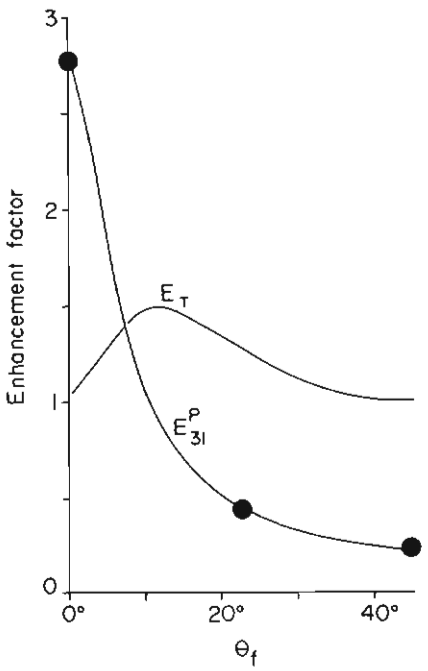

Figure 33. Model-derived linear enhancement factors for shear component of creep rate (E^p_{31}) and octahedral shear stress (E_τ) versus angle of tilt (θ_f) of fabric axis of symmetry away from platten normal into the direction of shear. Solid circles indicate measured shear enhancement factors for short-term simple shear tests.

5.3 SUMMARY AND CONCLUDING REMARKS

In retrospect, it is perhaps ironical that the first laboratory study of polycrystalline ice (McConnell and Kidd 1886) was most successful in indicating that the creep rate of an anisotropic aggregate is very sensitive to an implied relationship between the symmetry of its crystal orientation fabric and the configuration of the applied stress situation. Yet nearly a century later the quantitative roles of crystallography and stress configuration are not as well understood as those of temperature and shear stress magnitude (octahedral shear stress). Looking back the reason is clear. If it is assumed that the flow law for pure, dense polycrystalline ice is independent of the first stress invariant (Rigsby 1958), grain size and grain geometry, then the flow law will be a surface in a rheological space of at least seven dimensions. The rheological co-ordinates are octahedral deformation rate (dependent variable), temperature, the second and third deviatoric stress invariants, and at least three co-ordinates describing the crystal orientation fabric. For the simplest case of a single pole fabric approximating a spherical normal distribution, its standard deviation and, say, the two Euler angles of its axis of symmetry are required. Fabrics exhibiting additional axes or planes of symmetry require correspondingly more co-ordinates for a full description. It was not until midway through this century that advances in the technology of measurement and control made it possible to undertake well-controlled laboratory creep experiments (e.g. Glen 1952). With few exceptions, subsequent laboratory studies have concentrated on isotropic aggregates.

The hypothesis was put forward in Section 3 that if the rate-controlling mechanism for the creep of polycrystalline ice is basal glide, the deformation rate might be proportional to the root-mean-square resolved basal shear stress. It was then shown that this hypothesis leads to an isotropic flow law independent of the third deviatoric stress invariant. The flow law for isotropic polycrystalline ice thus degenerates to a surface in a three-dimensional rheological space where octahedral deformation rate is a function only of temperature and octahedral shear stress (cf. Budd 1969). This conclusion is consistent with past empirical laboratory results.

Since the pioneering field program of the Jungfraujoch Research Party of 1938, a large body of empirical field data describing the structure (grain size and geometry, crystallography, density, etc.) of natural ice has been collected. Only recently (Budd 1972) has such data been comprehensively re-examined to determine the large-scale distribution of crystallography and its development throughout an ice mass. Budd (1972) presents substantial evidence that the symmetry of a crystal orientation fabric tends to adopt that of the local stress configuration and that fabric development is flow induced. Thus the symmetry of the fabric lags that of the stress configuration and is modified by bulk rotations arising from flow constraints. In regions where gradients of the stress situation parameters (Section 2) are small, a strong correlation between the stress configuration parameter (third deviatoric stress invariant) and the crystal orientation fabric can be expected. In any case, field results from natural ice masses suggest (Budd 1972) that crystallographic features are systematically distributed throughout.

This information suggested a means (Section 3) of modelling the effects of anisotropic crystallography for a wide range of conditions encountered in natural ice masses. By introducing only one additional rheological co-ordinate, the flow law for an anisotropic aggregate can be examined in relation to that for an isotropic

aggregate. The new variable is an enhancement factor which yields the octahedral deformation rate of an anisotropic polycrystal relative to that of an isotropic polycrystal under identical conditions of temperature and stress situation. The flow law for an anisotropic aggregate then becomes

$$\dot{\gamma}_o(\tau_o, \Lambda, T, f, n) = E(f, \Lambda, n)\, A\, e^{Q \cdot RT} \tau_o^n \qquad (5.9)$$

where $\dot{\gamma}_o$ is the octahedral deformation rate of an ice aggregate exhibiting a crystallographic orientation density f; τ_o and Λ are the octahedral shear stress and stress configuration parameter; T is the temperature; $n = \partial(\ln \dot{\gamma}_o)/\partial(\ln \tau_o)$; Q is the activation energy for polycrystalline ice; R = 1.9 cal mole^{-1} °K^{-1}; and A is an empirical constant. The product $A\, e^{Q \cdot RT} \tau_o^n$ is the deformation rate of an isotropic aggregate found e.g. from the flow law presented in Figure 21. E(f, Λ, n) is the enhancement factor, related to stress configuration and crystallography in terms of a geometric tensor (Lile 1978). This geometric tensor can be viewed as a tensor coefficient of correlation between the configuration parameter of the local stress tensor (specifying the geometrical distribution of shear stress) and the crystal orientation fabric (specifying the geometrical distribution of basal planes). As a dynamic structural parameter, the geometric tensor has real meaning only for *deforming* ice. It is in essence a mathematical formulation of an empirical correlation found by Budd (1972) to be systematically distributed throughout an ice mass. It can therefore be specified (more practically in terms of the enhancement factor) as a structural function of position and utilised in present ice dynamics models.

The enhancement factor for octahedral deformation rate is defined in terms of the second invariant of the geometric tensor; enhancement factors for each component of the strain rate tensor can be defined in terms of the associated component of the geometric tensor. This generalisation allows the enhancement model to be applied directly to laboratory creep experiments in which only one strain rate component is measured. A linearised form of the enhancement factor (n = 1) was applied successfully to short-term laboratory creep tests replicating a variety of rheological conditions relevant to polar ice masses (Section 5.1.2).

If the flow law given by equation (5.9) is to be applicable to natural ice masses, it will be necessary to generalise the enhancement model to determine the functional dependence of E upon n for $n > 1$. Work directed toward this goal is now in progress. While details have yet to be finalised, first results indicate that

$$E(f, \Lambda, n) = [E(f, \Lambda, 1)]^{(n+1)/2} \qquad (5.10)$$

The non-linear enhancement estimates provided by equation (5.10) can be compared with the unpublished field and laboratory results of D. S. Russell-head. Russell-Head and Budd (1979) found that the crystal orientation fabrics in the Cape Folger, Antarctica borehole between about 150 m and 325 m exhibit a single pole cluster with a strength (or verticality) which varies with depth. The standard deviation (σ_θ) of c-axes about the vertical has been determined, by fabric analyses of the core, as a function of depth in the hole.

Non-linear enhancement factors were evaluated using equation (5.10), a spherical normal approximation to the measured fabrics (cf. Section 3.4), an easy glide situation in simple shear, a value for n of 1.7 (cf. Figure 21) and the measured vertical distribution of σ_θ. The model-derived enhancement factor as a function of depth is shown as a solid curve in Figure 34.

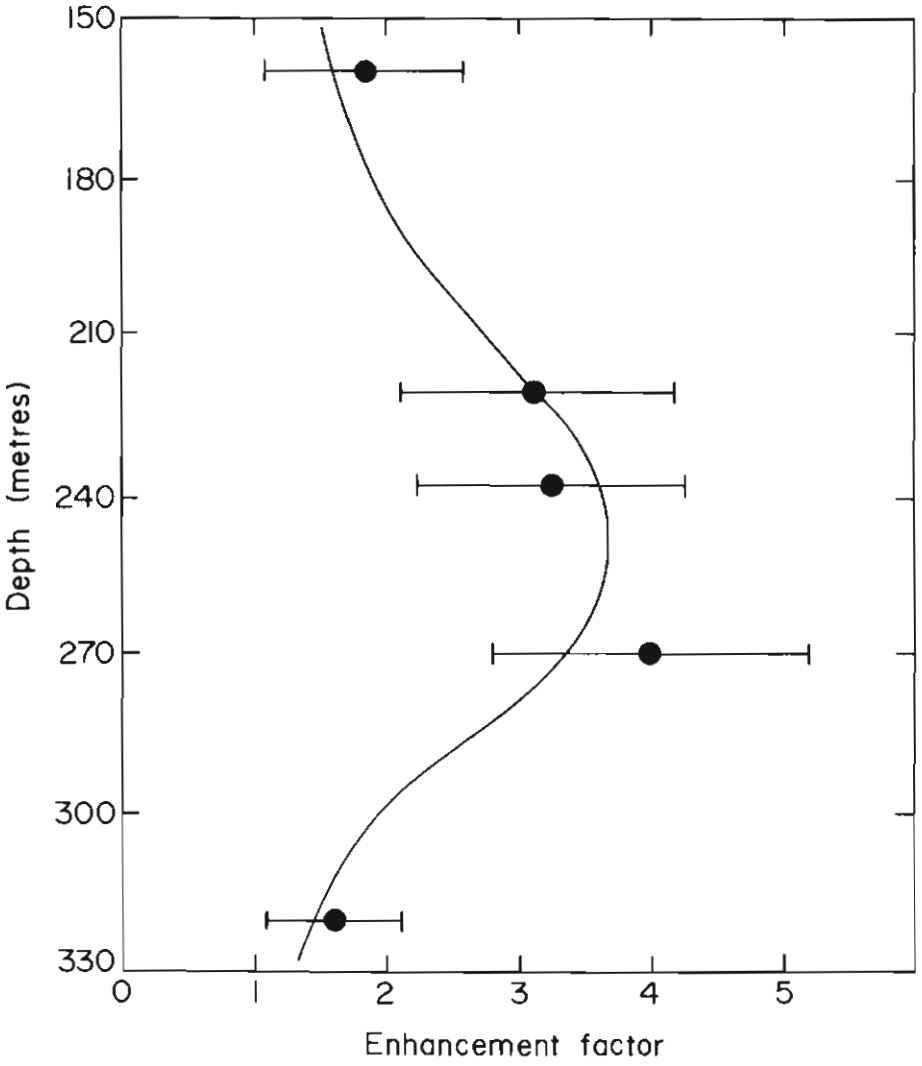

Figure 34. Enhancement factors versus depth in the 1974 Cape Folger borehole. (After Russell-Head and Budd 1979).

Russell-Head and Budd's laboratory study included a series of long-term simple shear creep tests on specimens prepared from the core. These experiments replicated *in situ* conditions of temperature and stress situation. Enhancement factors were calculated for each sample and have been entered as solid circles in Figure 34. The error bars are based on an expected experimental error of ± 20 per cent and an error of equal size in the measured σ_θ values. The general quantitative agreement between the enhancements predicted by the preliminary non-linear model and rheologically long-term laboratory results is encouraging.

A 1977 resurvey of the 1974 Cape Folger borehole provides an opportunity to compare the preliminary model results with field observations. The model-derived enhancement profile shown in Figure 34 suggests a region of enhanced horizontal shear rates at about 250 m down the hole. From the resurvey, a maximum in horizontal shear rate was observed at a depth of about 240 m (Russell-Head and Budd 1979). The model is in qualitative agreement with this observation.

Russell-Head and Budd (1979) pointed out the following implications concerning this observed enhancement of horizontal shear rates in the third depth quartile in the Cape Folger region. The vertical velocity profile differs significantly from that predicted by an isotropic flow law; thus, from a consideration of observed surface velocities and the large contribution of the enhanced quartile to this velocity, it can be concluded that residual shear rates in the lowest quartile of depth are quite small. It is generally assumed that octahedral shear stress increases in proportion to depth (e.g. Budd, 1969). Assuming further that the shear rates at depth are unenhanced and described by an isotropic flow law, the implied horizontal shear rates will still significantly overestimate the observed surface velocity. This apparent dilemma can be resolved by assuming in addition that shear stress decreases in the lowest quartile of depth in the ice mass.

The implied effect of strong anisotropic crystallography on computed particle paths and isochrones is obvious. An urgent need to consider the quantitative effects of crystallography in the flow law for natural anisotropic ice masses is clearly established. The enhancement model proposed and described in this study promises to provide a pragmatic and feasible approach to the realisation of this need. It has been successful in describing the principal qualitative characteristics of the observed velocity profile in the Cape Folger region. Once the question of stress situation at depth has been clarified, a quantitative field assessment of the model will be possible. Finally, the general mathematical basis on whieh the enhancement model has been constructed provides a receptive framework for new empirical and theoretical evidence.

Acknowledgements

I am particularly indebted to Dr Uwe Radok and Dr W. F. Budd, for their stimulating advice, prolonged encouragement and constructive criticism. Without the support of T. H. (Jo) Jacka, Vin Morgan, David Russell-Head, Neal Young and other members of the Australian National Antarctic Research Expeditions, a large part of the laboratory aspects of this study would not have been possible. The professiona! advice and technical assistance of John Turner, Michel Porcher and Barry McInnes of the Meteorology Department, proved invaluable. To these expeditioners and technical officers I express my sincere gratitude and thanks. The study was funded in part by the Antarctic Division of the Australian Department of Science and Technology. Data processing by the University of Melbourne Computer Centre is acknowledged with thanks.

References

Bader, H. (1964). Criteria for measurement of strain rates in deep boreholes in polar glaciers. *U.S. Army Cold Regions Research and Engineering Laboratory. Research Report* **127.**

Balla, A. (1960). Stress conditions in triaxial compression. *American Society of Civil Engineers. Journal of the Soil Mechanics and Foundations Division* **86** (SM6), 57.

Barnes, P., Tabor, D., and Walker, J. C. F. (1971). The friction and creep of polycrystalline ice. *Proceedings of the Royal Society, Series A* **324** (1557), 127-155.

Barnes, W. H. (1929). The crystal structure of ice betwen 0 °C and −183 °C. *Proceedings of the Royal Society, Series A* **125** (799), 670-693.

Barton, C. M. (1974). Simplified procedures for the vector summation and statistical analysis of spherically distributed point clusters. *CSIRO Division of Applied Geomechanics. Technical Report* **20.**

Batchelor, G. K. (1970). *An Introduction to Fluid Mechanics.* Cambridge Unviersity Press.

Berner, W., Bucher, P., Oeschger, H. and Stauffer, B. (1977). Analysis and interpretation of gas content and composition in natural ice. In: *Isotopes and Impurities in Snow and Ice.* Proceedings of the Grenoble Symposium, August/September, 1975. Pp. 272-284.

Blackman, R. B. and Tukey, J. W. (1958). *The Measurement of Power Spectra.* New York, Dover.

Boutron, C. and Martin, S. (1980). Sources of twelve trace metals in Antarctic snows determined by principal component analysis. *Journal of Geophysical Research* **85**(C10), 5631-5638.

Brace, W. F. (1960). Orientation of anisotropic minerals in a stress field: discussion. In: Griggs, D. and Handin, J. (eds.) *Rock Deformation. (Geological Society of America Memoirs* **79).** Chapter 2.

Bragg, W. H (1922). The crystal structure of ice. *Proceedings of the Physical Society of London* **34,** 98-103.

Budd, W. F. (1968). The longitudinal velocity profile of large ice masses. In: Ward, W. (ed.) *IUGG IASH General Assembly of Bern, 1967. Commission of Snow and Ice. Reports and discussions. (IASH Publication* **79).** Pp. 58-75.

Budd, W. F. (1969). Dynamics of ice masses. *ANARE Scientific Reports Series A(IV)* **108.**

Budd, W. F. (1970a). The longitudinal stress and strain rate gradients in ice masses. *Journal of Glaciology* **9** (55), 19-27.

Budd, W. F. (1970b). Ice flow over bedrock perturbations. *Journal of Glaciology* **9** (55), 29-48.

Budd, W. F. (1972). The development of crystal orientation fabrics in moving ice. *Zeitschrift für Gletscherkunde und Glazialgeologie* **8** (1-2), 65-105.

Budd, W. F. and Matsuda, M. (1974). Preferred orientation of polycrystalline ice by bi-axial creep test. *Low Temperature Science, Series A* **32,** 261-265.

Budd, W. F. and Jenssen, D. (1975). Numerical modelling of glacier systems. In: *Symposium on Interdisciplinary Studies of Snow and Ice in Mountain Regions, 1971. (IASH Publication* **104).** Pp. 257-291.

Butkovich, T. R. and Landauer, J. K. (1958). The flow law for ice. In: *Symposium of Chamonix, 1958. (IASH Publication* **47).** Pp. 318-325.

Butkovich, T. R. and Landauer, J. K. (1959). A grid technique for measuring ice tunnel deformation. *Journal of Glaciology* **3** (26), 508-511.

Butkovich, T. R. and Landauer, J. K. (1960). Creep of ice at low stresses. *U.S. Army Snow Ice and Permafrost Research Establishment, Research Report* **72.**

Chamberlin, R. T. (1928). Instrumental work on the nature of glacier motion. *Journal of Geology* **36** (1), 1-30.

Chamberlin, R. T. (1936). Glacier motion as typical rock deformation. *Journal of Geology* **44** 93-104.

Colbeck, S. C. and Evans, R. J. (1973). A flow law for temperate glacier ice. *Journal of Glaciology* **12** (64), 71-86.

Dansgaard, W. (1964). Stable isotopes in precipitation. *Tellus* **16**, 436-468.

Demorest, M. (1941). Glacier flow and its bearing on the classification of glaciers. *Bulletin of the Geological Society of America* **52**, 2024-2025.

Demorest, M. (1943). Ice sheets. *Bulletin of the Geological Society of America* **54**, 263-400.

Dillon, H. B. and Andersland, O. B. (1967). Deformation rates of polycrystalline ice. In: Oura, H. (ed.) *Physics of Snow and Ice, volume 1*. Sapporo, Hokkaido University, Institute of Low Temperature Science. Pp. 14-19.

Duval, P. (1972). Fluage et recrystallisation dynamique de la glace polycrystalline. *Comptes Rendes Hebdomadaires des Sceances de l' Academie des Sciences Paris, Serie D* **275** (3): 337-339.

Finnie, I. and Heller, W. R. (1959). *Creep of Engineering Materials*. New York, McGraw-Hill.

Fisher, R. (1953). Dispersion on a sphere. *Proceedings of the Royal Society, Series A* **217**, 295-305.

Frederking, R. (1972). Preliminary results of plane strain compression tests on columnar-grained ice. In: *Second Symposium on Ice and its Action on Hydraulic Structures, Leningrad, 1972*. Ottawa, National Research Council of Canada.

Gerrard, J. A. F., Perutz, M. F. and Roch, A. (1952). Measurement of the velocity distribution along a vertical line through a glacier. *Proceedings of the Royal Society, Series A* **213**, 546-558.

Gifkins, R. C. (1959). Recrystallisation of lead during creep. *Journal of the Institute of Metals* **87**, 255-261.

Gilman, J.J. (1968). Microdynamical theory of plasticity. In: *Advances in Material Science, Microplasticity*. New York, John Wiley. Pp 17-43.

Gilman, J. J. (1969). *Micromechanics of the Flow in Solids*. New York, McGraw-Hill.

Glen, J. W. (1952). Experiments on the deformation of ice. *Journal of Glaciology* **2** (12), 111-114.

Glen, J. W. (1953). Rate of flow of polycrystalline ice. *Nature* **172** (4381), 721-722.

Glen, J. W. (1955). The creep of polycrystalline iee. *Proceedings of the Royal Society, Series A* **228** (1175), 519-538.

Glen, J. W. (1958). The flow law of ice. In: *Symposium of Chamonix, 1958. (IASH Publication* **47***)*. Pp. 171-183.

Gold, L. W. (1963). Deformation mechanisms in ice. In: Kingery, W. D. (ed.) *Ice and Snow*. Cambridge, Massachusetts, MIT Press. Pp. 8-27.

Gold, L. W. (1973). Activation energy for creep of columnar-grained ice. In: Whalley, E., Jones, S. J., and Gold, L. W. (eds.) *Physics and Chemistry of Ice*. Papers presented at the Symposium on the Physics and Chemistry of Ice, Ottawa, 1972. Ottawa, Royal Society of Canada. Pp. 362-364.

Goughnour, R. R. and Andersland, O. B. (1968). Mechanical properties of a sand-ice system. *American Society of Civil Engineers. Journal of the Soil Mechanics and Foundations Division* **94** (SM4), 923-950.

Gow, A. J. (1963). Results of measurements in the 309 bore hole at Byrd Station, Antarctica. *Journal of Glaciology* **4** (36), 771-784.

Hagenbach-Bishoff, E. (1889). Weiteres über Gletchereis. *Verhandlungen Naturforschende Gesellschaft in Basle* **8**, 821-832.

Hansen, B. L. and Landauer, J. K. (1958). Some results of ice cap drill hole measurements. In *Symposium of Chamonix, 1958. (IASH Publication* **47**). Pp. 313-317.

Hawkes, I. and Mellor, M. (1970). Uniaxial testing in rock mechanics laboratories. *Engineering Geology* **4**(3), 177-285.

Hawkes, L. (1930). Some notes on the structure and flow of ice. *Geological Magazine* **67**, 111-123.

Herceg, E. E. (1972). *Handbook of Measurement and Control.* Pennsauken, New Jersey, Schaevitz.

Higashi, A. (1967). Mechanisms of plastic deformation in ice single crystals. In: Oura, H. (ed.) *Physics of Snow and Ice, volume 1.* Sapporo, Hokkaido University, Institute of Low Temperature Science. Pp. 277-289.

Holdsworth, G. (1975). Measurement of small strain rates over short time periods. *Journal of Glaciology* **14** (71), 317-324.

Hooke, R. LeB. (1969). Crystal shape in polar glaciers and the philosophy of ice fabric diagrams. *Journal of Glaciology* **8** (53), 324-326.

Hooke, R. LeB., Dahlin, B.B. and Kauper, M.T. (1972). Creep of ice containing dispersed fine sand. *Journal of Glaciology* **11** (63), 327-336.

Hooke, R. LeB., Mellor, M., Budd, W.F., Glen, J. W., Higashi, A., Jacka, T. H., Jones, S. J., Lile, R. C., Martin, R. T., Meier, M. F., Russell-Head, D. S. and Weertman, J. (1980). Mechanical properties of polycrystalline ice: an assessment of current knowledge and priorities for research. *Cold Regions Science and Technology* **3**, 263-275.

Howard, A. D. (1948). The preservation of Antarctic ice specimens. *Journal of Geology* **56** (1), 67-71.

Hughes, T. P. and Seligman, G. (1939). The temperature, meltwater movement and density increase in the neve of an Alpine glacier. *Roval Astronomical Society Monthly Notices. Geophysical Supplement* **4** (8), 616-647.

Jacka, T. H. (1984). The time and strain required for the development of minimum strain rates in ice. *Cold Regions Science and Technology* **8** (3), 261-268.

Jacka, T. H. and Lile, R. C (1984). Sample preparation techniques and compression apparatus for ice flow studies. *Cold Regions Science and Technology* **8** (3), 235-240.

Jaeger, J. C. (1969). *Elasticity, fracture and flow.* London. Methuen.

Johnson, S. J., Dansgaard, W., Clausen, H. G., and Langway, C.C. (1972). Oxygen isotope profiles through the Antarctic and Greenland ice sheets. *Nature* **235**, 429-434.

Kamb, W. B. (1961). The glide direction in ice. *Journal of Glaciology* 3 (30), 1097-1106.

Kamb, W. B. (1972). Experimental recrystallisation of ice under stress. In: Heard, H.C., Borg, I. Y., Carter, N. L. and Raleigh, C. B. (eds.) *Flow and Fracture of Rocks (American Geophysical Union Monograph* **16).** Pp. 210-241.

Langdon, T. G. (1973). Creep mechanisms in ice. In: Walley, E., Jones, S. J., Gold, L. W. (eds) *Physics and Chemistry of Ice.* Papers presented at the Symposium on the Physics and Chemistry of Ice, Ottawa, 1972. Ottawa, Royal Society of Canada. Pp. 356-361.

Lile, R. C. (1978). The effect of anisotropy on the creep of polycrystalline ice. *Journal of Glaciology* **21** (85), 475-483.

Luton, M. J. and Sellars, C. M. (1969). Dynamic recrystallisation in nickel and nickel-iron alloys during high temperature deformation. *Acta Metallurgica* **17** (8), 1033-1043.

McConnell, J. C. and Kidd, D. A. (1886). On the plasticity of glacier and other ice. *Proceedings of the Royal Society, Series A* **44** (270), 331-337.

McElhinny, M. A. (1967). Statistics of a spherical distribution. In: *Methods in Paleomagnetism, Developments in Solid Earth Geophysics.* Amsterdam, Elsevier. Pp. 314-321.

McLaren, W. A. (1968). A study of the local ice cap near Wilkes, Antarctica. *ANARE Scientific Reports Series A (IV)* **103.**

Meier, M. G. (1958). Vertical profiles of velocity and the flow law of glacier ice. In: *Symposium of Chamonix, 1958. (IASH Publication* **47**). Pp. 169-170.

Mellor, M. and Smith, J. H. (1966). Creep of snow and ice. *U. S. Army Cold Regions Research and Engineering Laboratory. Report* **220.**

Mellor, M. and Testa, R. (1969). Effect of temperature on the creep of ice. *Journal of Glaciology* **8** (52), 131-145.

Morgan, V. I. (1982). Antarctic ice sheet surface oxygen isotope values. *Journal of Glaciology* **28** (99), 315-323.

Nayar, H. S. (1966). Creep behaviour of pure ice and ice dispersed with ultrafine amorphous silica (SiO_2) particles. *Phd Thesis*. New York, Rensselaer Polytechnic Institute.

Nyc, J. F. (1952). The mechanics of glacier flow. *Journal of Glaciology* **2** (12), 82-93.

Nye, J. F. (1953). The flow law of ice from measurements in glacier tunnels, laboratory experiments and the Jungfraufirn bore hole experiment. *Proceedings of the Royal Society, Series A* **219** (1139), 477-489.

Nye, J. F. (1957). The distribution of stress and velocity in glaciers and ice sheets. *Proceedings of the Royal Society, Series A* **239**, 113-133.

Nye, J. F. (1959). A method of determining the strain rate tensor at the surface of a glacier. *Journal of Glaciology* **3** (25), 409-419.

Paterson, W. S. B. (1977). Secondary and tertiary creep of glacier ice as measured by borehole closure rates. *Reviews of Geophysics and Space Physics* **15** (1), 47-55.

Perutz, M. F. (1940). Mechanism of glacier flow. *Proceedings of the Physical Society* **52**, 132-135.

Perutz, M. F. and Seligman, G. (1939). A crystallographic investigation of glacier structure and the meehanism of glacier flow. *Proceedings of the Royal Society, Series A* **172**, 335-360.

Phillips, F C. (1971). *The Use of Stereographic Projection in Structural Geology. London, Edward Arnold.*

Raraty, L. E. and Tabor, D. (1958). The adhesion and strength properties of ice. *Proceedings of the Royal Society, Series A* **245** (1241), 184-201.

Raynaud, D. and Lorius, C. (1973). Climatic implications of total gas content in ice at Camp Century. *Nature* **243**,283-284.

Richardson, G. J., Sellars, C. M. and Tegart, W. J. McG. (1966). Recrystallisation during creep of nickel. *Acta Mettallurgica* **14**, 1225-1236.

Rigsby, G. P. (1958). Effect of hydrostatic pressure on velocity of shear deformation of single ice crystals. *Journal of Glaciology* **3** (24), 273-278.

Rigsby, G. P. (1960). Crystal orientation in glacier and experimentally deformed ice. *Journal of Glaciology* **3** (27), 589-606.

Rigsby, G. P. (1968). The complexities of the three-dimensional shape of individual crystals in glacier ice. *Journal of Glaciology* 7 (50), 233-251.

Rotherham, L. (1951). *Creep of Metals.* London, Unwin.

Russell-Head, D..S. and Budd, W. F. (1979). Ice sheet flow properties derived from bore-hole shear measurements combined with ice core studies. *Journal of Glaciology* **24** (90), 117-130.

Seligman, G. (1948). The growth of the glacier crystal. *Journal of Glaciology* **1** (5), 254-267.

Shumskiy, P. A. (1958). The mechanism of ice straining and its recrystallisation. In: *Symposium of Chamonix, 1958. (IASH Publication* **47**). Pp. 244-248.

Shumskiy, P. A. (1964). *Principles of Structural Glaciology.* New York, Dover.

Sinha, N. K. (1977). Short time rheology of polycrystalline ice. *Journal of Glaciology* **21** (85), 457-473.

Steinemann, S. (1954). Flow and recrystallisation of ice. In: *IUGG IASH General Assembly of Rome. (IASH Publication* **39**). Pp. 449-462.

Steinemann, S. (1958a). Experimentelle Unterschungen zur Plastizität von Eis. *Beiträge zur Geologie der Schweiz. Geotechnische Series Hydrologie* **10.**

Steinemann, S. (1958b). Resultats experimentaux sur la dynamique de la glace et leurs correlations avec le mouvement et la petrographie des glaciers. In: *Symposium of Chamonix, 1958. (IASH Publication* **47**). Pp. 184-189.

Streif-Becker, R. (1938). Zur Dynamik des Firneises. *Zeitschrift für Gletscherkunde* **26**, 1-21.

Sydenham, P. H. (1972). Microdisplacement transducers. *Journal of Scientific Instruments (Journal of Physics E)* **5**, 721-735.

Taylor, G. I. (1956). Strains in crystalline aggregate. In: Grammel, R. (ed.) *Deformation and Flow of Solids, Colloquium of Madrid, 1955*. International Union of Theoretical and Applied Mechanics. Pp. 3-12.

Vialov, S. S. (1958). Regularities of ice deformation. In: *Symposium of Chamonix, 1958. (IASH Publication* **47**). Pp. 383-391.

Vialov, S. S. (1970). Laws of ice deformation. Translated from: *Sovetskaya Antarktischeskaya Ekspeditsiya* **10**. Springfield, National Technical Information Service. Pp. 239-249.

Voitkovskii, K. F. (1957). Eksperimental'nye issledovaniya plasticheskikh svoystv l'da (Experimental studies on the plastic properties of ice). In: *Sezonnoye Promerzaniye Gruntov i Primeneniye l'da dlya Stroitel'nykh Tseley*. Moscow, Akademiya Nauk SSSR, Institute Merzlotovedeniya. Pp. 101-136.

Voitkovskii, K. F. (1960). *The Mechanical Properties of Ice*. English translation. Boston, American Meteorological Society.

Wakahama, G. (1967). On the plastic deformation of single crystals of ice. In: Oura, H. (ed.) *Physics of Snow and Ice, volume 1*. Sapporo, Hokkaido University, Institute of Low Temperature Science. Pp. 291-311.

Weertman, J. (1963). The Eshelby-Schoeck viscous dislocation damping mechanism applied to the steady-state creep of ice. In: Kingery, W. D. (ed.) *Ice and Snow*. Cambridge, Massachusetts, MIT Press. Pp. 28-33.

Weertman, J. (1968). Dislocation climb theory of steady-state creep. *Transactions of the American Society for Metals* **61**(4), 681-694.

Weertman, J. (1969). The stress dependence of the secondary creep rate at low stresses. *Journal of Glaciology* **8**(54), 494-495.

Weertman, J. (1973). Creep of ice. In: Whalley, E., Jones, S. J. and Gold, L. W. (eds.) *Physics and Chemistry of Ice*. Papers presented at the Symposium on the Physics and Chemistry of Ice, Ottawa, 1972. Ottawa, Royal Society of Canada. Pp. 320-337.

Wilson, S. D. (Unpublished). *Report on 1958 Tuto Ramp Slope Indicator Meaurements*. Report prepared for the U.S. Army Engineers Division by Shannon and Wilson, Seattle, Washington.

Wolfendale, P. C. F. (1968). Capacitive displacement transducers with high accuracy and resolution. *Journal of Scientific Instruments (Journal of Physics E) Series 2* **1**, 817-818.